Escuela de Ingenierías Industriales

TESIS DOCTORAL

Programa de doctorado de Ingeniería Mecatrónica

Experimental study in near-and far-field of trailing vortices and their active control

A DISSERTATION PRESENTED
BY
JOSE HERMENEGILDO GARCÍA ORTIZ
TO
THE DEPARTMENT OF MECHANICAL, THERMAL AND FLUID ENGINEERING

IN PARTIAL FULFILLMENT OF THE REQUIREMENTS
FOR THE DEGREE OF
DOCTOR OF INDUSTRIAL ENGINEERING
IN THE SUBJECT OF
MECHATRONICS ENGINEERING

THESIS SUPERVISORS:
DR. CARLOS DEL PINO PEÑAS
DR. LUIS PARRAS ANGUITA

UNIVERSIDAD DE MALAGA
MÁLAGA, ESPAÑA
OCTOBER 2017

AUTOR: José Hermenegildo García Ortiz

http://orcid.org/0000-0003-0670-8109

UNIVERSIDAD
DE MÁLAGA

Acknowledgments

UNIVERSIDAD
DE MÁLAGA

Contents

Listing of figures

Estudio experimental de los vórtices de estela de ala hasta el campo lejano y su control activo

Extended Spanish Abstract

Los vórtices se definen como el volumen finito de fluido sometido a una fuerte rotación que está limitado en su frontera por un flujo en reposo relativo, o bien está confinado por paredes sólidas. Los vórtices se encuentran en gran variedad de fenómenos atmosféricos, como pueden ser los tornados, en otras aplicaciones tecnológicas con o sin reacciones químicas como mezcladores, motores de combustión interna o turborreactores y también en vehículos marítimos o aéreos, como por ejemplo las hélices de los barcos y helicópteros. Además de estos últimos ejemplos, los rodetes que existen en otras turbomáquinas hidráulicas como bombas centrífugas, axiales o mixtas, así como en turbinas eólicas o aerogeneradores también presentan torbellinos similares a los que se estudian en esta tesis doctoral, y que resultan del paso de un fluido a gran velocidad por un perfil aerodinámico.

El objetivo de este trabajo de investigación se centra en el estudio y control de los vórtices o torbellinos de estela de ala (denominados en inglés *wingtip vortex*) que se forman en el extremo del perfil aerodinámico. Este torbellino se forma siempre en la configuración de vuelo (cuando existe fuerza de sustentación), ya que existe una diferencia de presiones entre su cara superior (extradós) y su cara inferior (intradós). Las grandes masas de fluido que se mueven por ambas caras se encuentran justamente en el extremo del perfil aerodinámico que es donde tiene lugar el origen del vórtice. El patrón de la estela del vórtice detrás del ala se describe como una gran masa de aire que se desprende del ala rotando en un determinado sentido, se mueve aguas abajo por convección y se va formando hasta tener una estructura bien definida, mientras que simultáneamente se difunde gradualmente conforme el perfil aerodinámico se desplaza. Al vórtice también le afecta la posible interacción con otros vórtices, la influencia del viento o la estratificación de la atmósfera.

La intensidad de los torbellinos en perfiles aerodinámicos es proporcional a la fuerza de sustentación, y esta a su vez, al peso de la aeronave. Debido a que es en las operaciones de despegue y aterrizaje cuando esta fuerza es mayor, se hace necesario establecer una separación temporal entre las aeronaves, lo que conlleva la reducción de la frecuencia de operaciones en aeropuertos y, consecuentemente, limita la capacidad de éstos. En este sentido, las organizaciones internacionales establecen tiempos de espera que garanticen la seguridad en las operaciones aeroportuarias. El tiempo de espera depende del tipo de aeronave que preceda a la que va a realizar la maniobra de despegue o aterrizaje. Si bien los tiempos de espera suelen ser de 1-2 minutos para aeronaves comunes, en el caso del gigante A-380 de Airbus el tiempo de espera puede ser de hasta 3-5 minutos. Una de las estrategias usadas en aeropuertos de un gran tráfico para conocer si el torbellino está o no presente en la pista del aeropuerto es la colocación de un sonar que lo detecte. En cualquier caso, la eliminación de este torbellino se considera un reto tecnológico hoy en día.

Estos vórtices fueron descritos por primera vez en 1907, solo cuatro años después del primer vuelo de los hermanos *Wright* y fue en 1964 cuando Batchelor [1964] publicó el primer modelo teórico y simplificado considerando la componente de la velocidad axial. Unos años más tarde, este modelo fue complementado por Moore & Saffman [1973] que desarrolló su modelo teórico a partir de las visualizaciones llevadas a cabo por Olsen [1970] teniendo en cuenta el proceso de formación del vórtice. Este último modelo mejoró las discrepancias entre el modelo original desarrollado por Batchelor y los datos experimentales en el campo cercano del torbellino. Otros estudios teóricos llevados a cabo por Uberoi [1979] indican que la velocidad del centro del vórtice decae por convección radial debido a la diferencia de velocidad axial entre el núcleo y el fluido circundante y McCormick et al. [1968] mostró que esta diferenciad de velocidad axial es necesaria para el sustento de la turbulencia en el núcleo del vórtice. Heyes et al. [2004] concluyó que la turbulencia de la corriente libre alrededor del ala altera el proceso de formación de vórtices, pero no tiene un efecto acusado

sobre el vórtice cuando éste está totalmente formado.

Años más tarde, del Pino et al. [2011b] realizó mediciones experimentales de la evolución axial de los vórtices identificando la trayectoria del núcleo del vórtice e introduciendo nuevos parámetro en los modelos de Batchelor (B) y Moore and Saffman (MS). En este trabajo de investigación encontraron que los perfiles del modelo MS describen mejor los flujos axiales cerca del centro del vórtice que el modelo B, tal y como también corroborarán más adelante Feys & Maslowe [2014, 2016]. Además, del Pino et al. [2011b] analizaron la dependencia de esos parámetros con el número de Reynolds basado en la cuerda, ya que tal y como advirtió Green & Acosta [1991], la velocidad axial media es fuertemente dependiente del número de Reynolds mientras se estudia la inestabilidad en los vórtices de estela de ala. Por otro lado, Sun & Daichin [2011] observó el efecto de las proximidades del suelo sobre el torbellino detrás del ala en términos de la vorticidad, las fuerzas de arrastre y sustentación, obteniendo que el núcleo del vórtice se desplaza hacia fuera de la punta del ala debido a la presencia del suelo, y el desplazamiento del torbellino cerca del mismo disminuye además con la reducción del ángulo de ataque.

Tal y como se puede observar, el análisis de los vórtices ha suscitado bastante interés a lo largo de los años, llevándose a cabo estudios teóricos, numéricos o experimentales para entender mejor su comportamiento y conocer mejor su campo de velocidad. Con la realización de estudios experimentales, los primeros investigadores en llevarlos a cabo [Gaspareck, 1960; Orloff, 1974] se dieron cuenta de un fenómeno intrínseco de los vórtices, el cual propiciaba una dificultad añadida para realizar las mediciones deseadas y la reproducibilidad de los experimentos. Este fenómeno se conoce en inglés como *meandering* e implica que el vórtice tiene un movimiento aleatorio e impredecible (ver Figura 1). Esto supone un problema serio para los experimentalistas, ya que los primeros ensayos se llevaron a cabo en túneles de viento usando la técnica de anemometría térmica (o de hilo caliente) para medir la velocidad del torbellino en un determinado punto del dominio espacial. El problema radica en que debido a este movimiento aleatorio del vórtice, resulta muy difícil determinar el perfil de velocidad usando uno o varios hilos. Fueron varios autores los que llevaron a cabo un estudio de este fenómeno, pero Devenport et al. [1996] fue el que realizó el análisis más detallado ya que determinó la magnitud del *meandering* para corregir las medidas realizadas usando hilo caliente y años más tarde fue confirmado por Heyes et al. [2004] usando la técnica de velocimetría por partículas (o en inglés, PIV, de las iniciales *Particle Image Velocity*). Básicamente, el proceso del movimiento aleatorio o *meandering* pudo ser eliminado moviendo el centro del torbellino en cada instante a un sistema de referencia fijo.
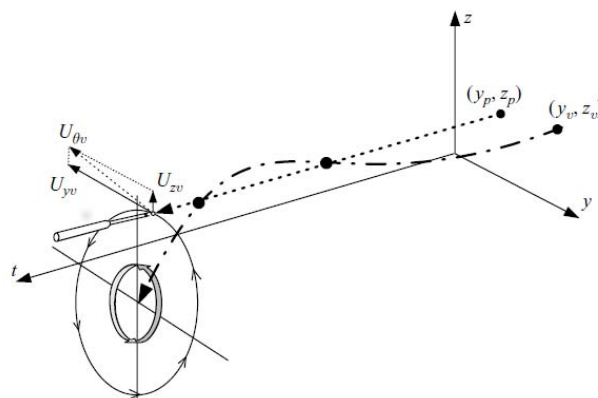
Figure 1: Esquema que define la posición del vórtice (y_v, z_v) en el plano (y, z), la posición de la sonda de hilo caliente (y_p, z_p) en el plano (y, z) y las componentes U_{yv}, U_{zv} de la velocidad inducidas por el vórtice en la posición de la sonda cuando este tiene un movimiento aleatorio en el tiempo [Bailey & Tavoularis, 2008].

Una vez descritos los vórtices de estela de ala, sus modelos teóricos y las dificultades de los ensayos experimentales, se va a tener en cuenta otro tema de interés que tiene que ver con su control. Es evidente el interés que existe por parte de grandes constructores de la industria aeronáutica (como Airbus o Boeing) por patentar un dispositivo robusto y seguro que sea capaz de romper el vórtice de estela de ala en las operaciones de

despegue y aterrizaje, tal y como se comentó anteriormente. Este avance tecnológico aumentaría, sin lugar a dudas, la capacidad aeroportuaria. Actualmente se han tratado de romper o eliminar los vórtices, mediante distintas estrategias que pueden ser clasificadas en dos grupos:

· *Control pasivo*, que engloba todas las técnicas con las que se pretende actuar con el vórtices que implican cambios de geometría en el ala.

· *Control activo*, engloba todas las técnicas que actúan sobre el vórtice a través de la interacción directa sobre el mismo de forma forzada.

Los elementos de control pasivo, únicamente podrán ser optimizados para un determinado régimen de vuelo, mientras que los dispositivos de control activo pueden ser diseñados y puestos en marcha de manera óptima para distintas condiciones de vuelo. Se han sugerido múltiples soluciones, pero hasta ahora los denominados *winglets* ha sido reconocida como la más eficaz y práctica para reducir parcialmente los efectos de los vórtices y están implementados en muchos de los aviones comerciales actuales. Se trata de una deformación en la parte final del ala, que resulta en una curvatura más acusada de su extremo.
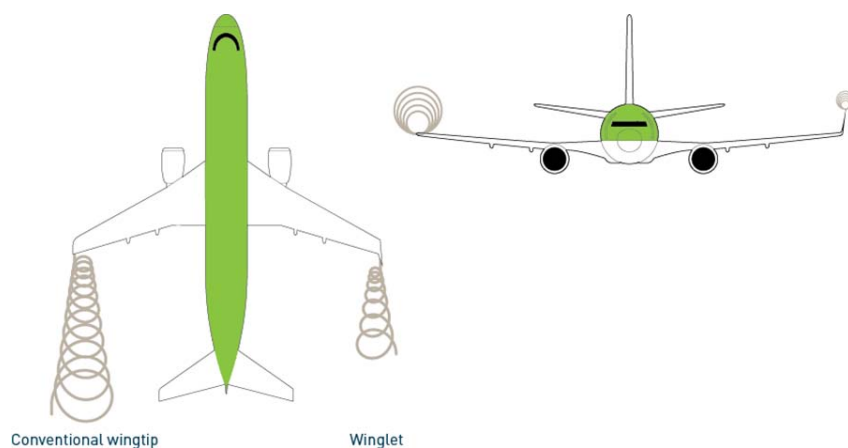
Figure 2: Configuración de un perfil aerodinámico con *winglets*.

Por otro lado, la tipología de los elementos de control activo consta de técnicas como el mecanismo de soplado, los chorros sintéticos (*synthetic jets*) o perfiles que pueden cambiar su forma dinámica dependiendo de las condiciones en las que opere la aeronave. El mecanismo de soplado fue el primero y es, además, una de las técnicas más estudiadas, probablemente por su fácil implementación. Esta técnica consiste en la inyección de un chorro en el extremo del ala. Los primeros estudios que se realizaron aplicando esta técnica, Carafoli [1964]; Carafoli & Camarasescu [1971], aportaron que se producía un aumento de la sustentación de forma independiente del arrastre. Esto se debió a que el soplado producía un aumento de la envergadura del ala. Wu et al. [1982] analizaron también una disposición de soplado en el borde del ala con varios chorros muy finos que salen por una ranura cuya longitud es una fracción de la cuerda del ala. Aunque esta disposición no producía una prolongación efectiva de la envergadura, se observaron multitudes similitudes con el efecto del *winglet*. Esta técnica ha sido desarrollada a lo largo de los años, produciendo variaciones en parámetros como el tamaño de la zona de soplado, el ángulo de ataque del soplado o la zona en la que se produce el soplado (aguas arriba o aguas abajo del perfil aerodinámico)
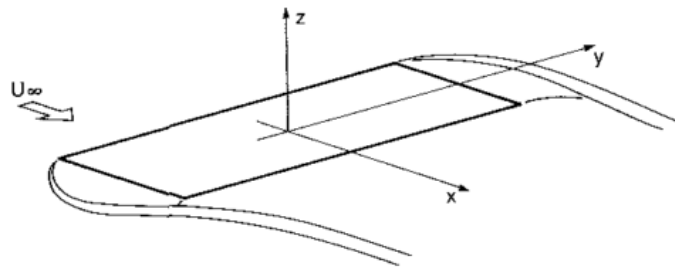
Figure 3: Mecanismo de soplado en el lateral del perfil aerodinámico [Tavella et al., 1986].

La técnica de chorros sintéticos consiste en la vibración de una membrana unida a una cavidad con una pequeña apertura. La creación de un chorro sintético consiste en una compresión-expansión periódica en la membrana y, en consecuencia, del fluido dentro de la cavidad, dando como resultado una oscilación del fluido en el orificio que finalmente introduce un soplado en el flujo externo de la boquilla, pero sin variación total de masa. Esta técnica permite trabajar con varios parámetros como son la frecuencia o la amplitud.

Recientemente, también se han desarrollado tecnologías para reducir la resistencia aerodinámica sin que exista una disminución en la sustentación basadas en variaciones dinámicas de la forma del perfil aerodinámico del ala. Estos cambios se producen mediante actuadores piezoeléctricos o mediante elementos flexibles que dan como resultado un cambio en la morfología del perfil.

Para predecir el desarrollo de la fuerza axial de los vórtices de estela de ala, se requiere un modelo teórico preciso (B o MS). Existen varias técnicas experimentales para este fin, por ejemplo, PIV, anemometría láser o térmica, pero implican un costo y un esfuerzo significativos. Por esta razón, en este trabajo de investigación se ha llevado a cabo un estudio experimental basado en visualizaciones mediante una cortina de humo. Estas se han llevado a cabo en un túnel de viento subsónico cerrado de la Universidad de Málaga, con una cámara de ensayos de $1 \times 1 m^2$ de sección y 4m de longitud. Para el montaje experimental se ha elegido el perfil aerodinámico NACA0012 con una cuerda (c) de 0.1m y una envergadura de 0.2m, el cual ha sido instalado en un soporte controlado por un servomotor que gira sobre el eje vertical para colocar así el ángulo de ataque deseado. Para producir la cortina de humo, se ha usado un hilo de niquel de 1m de longitud y 0.12mm de diámetro impregnado en aceite el cual se vaporiza debido al incremento de temperatura producido en el cable mediante la imposición de una alta corriente eléctrica de forma instantánea. Una vez producido el humo, se crea un plano láser perpendicular al movimiento del flujo, consiguiendo, mediante una cámara de alta velocidad visualizar las trazas de humo en seis planos perpendiculares a la dirección del flujo principal.

La técnica de visualización se ha demostrado que es no intrusiva y robusta. Para conseguir las imágenes, era necesario previamente un flujo en estado estacionario en la sección de ensayo del túnel de viento antes de accionar el hilo de humo. Es esencial sincronizar todos los actuadores y elementos en los sistemas de hilo de humo y cámaras digitales. Una vez que se ejecuta el impulso de corriente sobre el cable de humo, el disparador de cámara de alta velocidad tiene que activar el modo de grabación. Se registra la aparición / desaparición de la superficie de humo con forma de flujo en rotación a través del plano de medida y se almacenan las instantáneas. Se ha de destacar que sólo la imagen con la intensidad más alta del humo fue analizada en varios planos en la dirección axial o de la corriente libre del túnel de viento. Por lo tanto, estas imágenes instantáneas proporcionan información relativa a patrones de vórtice de flujo producidos por las fuerzas de elevación del ala cuando la corriente principal pasa a través del perfil aerodinámico. Posteriormente se seleccionan un conjunto de puntos experimentales en estos fotogramas instantáneos. En consecuencia, se recoge una descripción bidimensional del vórtice en el plano de medida. Se hicieron mediciones en seis planos $z = 0, c, 2c, 3c, 4c$, y $5c$ junto con dos valores representativos de W_∞.

Con el fin de analizar la influencia de la estela producida por el hilo de humo en los patrones de flujo de aire, se ha calculado el número de Reynolds basado en el diámetro del alambre, Re_D. Los valores están en el intervalo entre 60 y 168 para las velocidades ensayadas. Despreciando el efecto del impulso para realizar el calentamiento necesario para evaporar el aceite, el flujo pertenece al régimen laminar de vórtices en dos dimensiones (2D), y los regímenes de transición a un flujo tridimensional (3D). Debido al hecho de que el humo se genera en la superficie del alambre, cualquier inestabilidad de la estela proviene de un aumento de

la anchura de las líneas de humo en el caso de las inestabilidades 2D, mientras que las 3D se rompen en las líneas de humo en la dirección axial. Se han aportado evidencias experimentales de estos hechos. El efecto principal de la estela del hilo de humo es el aumento de la incertidumbre en la determinación de los puntos seleccionados para establecer, mediante la línea de humo, la forma del vórtice. Podemos confirmar que el error es inferior al 3 % para los parámetros del modelo B.

Así pues, usando esta técnica de visualización, se ha obtenido información cuantitativa del campo de velocidad del vórtice mediante el modelo B para dos números de Reynolds basados en la cuerda, Re_c =3,33×10^4 y 10^5. Por lo tanto, este modelo de vórtice teórico se ha introducido en la integración de las ecuaciones diferenciales ordinarias que describen la evolución temporal de las trazas en función de dos parámetros: la intensidad del vórtice S y la coordenada del centro virtual $\overline{z_0}$ del mismo. Mientras que las trazas son calculadas mediante el análisis de imágenes, los parámetros S y $\overline{z_0}$ se han calculado mediante las ecuaciones diferenciales, que han sido resueltas con éxito. En esto se basa el novedoso método descrito en esta tesis doctoral. Además, se han aplicado dos procedimientos diferentes para minimizar la distancia entre patrones de flujo experimentales y teóricos: ajuste de curva individual en seis planos de control diferentes en la dirección del flujo, así como el ajuste de curva global que corresponde a todos los planos de control simultáneamente. Ambos conjuntos de resultados se han comparado con los proporcionados por del Pino et al. [2011a] obtenidos mediante stereo-PIV en el túnel de agua usando el mismo perfil aerodinámico, encontrando un buen acuerdo. Por último, se ha observado una débil influencia del número de Reynolds sobre los valores S y $\overline{z_0}$ para los valores de Re_c considerados en este estudio. Esta técnica experimental se propone como una alternativa de bajo costo para caracterizar vórtices de extremo de ala basados en visualizaciones de flujo.

Seguidamente, se presenta un análisis detallado de los resultados experimentales y numéricos para el flujo de torbellinos formados en la estela de un ala usando el mismo perfil aerodinámico, el NACA0012. En este caso los experimentos se han realizado en un canal de arrastre, con unas dimensiones de 0.5m x 0.5m y 10m de longitud el cual ofrece un alcance de hasta 40 cuerdas, usando la técnica de 2D-PIV para obtener el campo de velocidad. La principal razón del uso del canal de arrastre es que al no existir elementos que desplacen el fluido, los niveles de turbulencia conseguidos son extremadamente bajos. Para obtener las imágenes se genera un plano láser en la dirección perpendicular al movimiento del ala y se mezcla el agua con esferas de vidrio recubiertas de plata, con la misma densidad del agua. Estas esferas brillan gracias a la luz del láser continuo de 1.5 W y a través de una cámara de alta velocidad se obtienen dichas imágenes. Las imágenes son posteriormente procesadas por el software DPIVSoft desarrollado conjuntamente en un instituto de investigación de Marsella y la Universidad de Málaga. Se presta especial atención a un valor específico del ángulo de ataque, α =9°, y los números de Reynolds bajos basados en la cuerda que van desde Re_c =7×10^3 a 20×10^3. Este tipo de experimentos tienen una dificultad añadida que tiene que ver el fenómeno de *meandering*, cuyo efecto implica un movimiento aleatorio del núcleo del torbellino, tal y como se ha comentado anteriormente. La dificultad de procesar datos bajo este efecto radica en que en los distintos experimentos realizados para un mismo caso, la posición del torbellino no es la misma, por lo que llevar a cabo un promedio nos puede conducir a un error. Para evitar este efecto, se ha realizado un centrado de cada experimento sobre una sistema de referencia común, teniendo así para todos los casos una posición fija del centro del torbellino.

En la parte numérica de este trabajo de investigación se han resuelto las ecuaciones de Navier-Stokes en un dominio espacial usando 3D-DNS (*Direct Numerical Simulation*), el cual simula un túnel de viento con una sección 0.4m x 0.4m y 1.5m de longitud usando el mismo perfil alar, NACA0012, y el mismo ángulo de ataque $\alpha = 9°$. Este dominio es ligeramente más pequeño que el experimental debido al elevado coste computacional que requiere la ejecución de simulaciones directas (DNS), por lo que solo nos ofrece un alcance de hasta 10 cuerdas. Los números de Reynolds estudiados son desde $Re_c = 0.3×10^3$ up to Re_c =7×10^3 llevando a cabo los correspondientes análisis de malla, llegando esta en el último caso a tener del orden de treinta millones de nodos. Fueron necesarias varias semanas de ejecución del código en el supercomputador Picasso de la Universidad de Malaga para completar un solo caso.

Se han comparado los perfiles de velocidad obtenidos tanto numéricamente como de forma experimental para Re_c =7× 10^3 hasta 10 cuerdas quedando el método numérico validado. Se ha elegido este caso porque es donde ambos métodos coinciden, ya que Re_c =7×10^3 es el mayor conseguido de forma numérica y el

menor que se ha podido conseguir experimentalmente debido a que para números de Reynolds más bajos, el movimiento residual del agua es del mismo orden que el del torbellino siendo por tanto muy difícil su caracterización cuantitativa debido al alto nivel de dispersión en los datos.

Una vez que se han validado los resultados, se ajustan los parámetros teóricos en función del Re_c para lo modelos teóricos B y MS tanto para los datos numéricos como para los experimentales. Dichos parámetros son dos, S y $\overline{z_{0B}}$, para el modelo B y tres, n, b y $\overline{z_{0MS}}$, para el modelo MS. Los parámetros S y b se corresponden con la intensidad del vórtice, mientras que el parámetro n nos indica como decae el perfil radial de velocidad acimutal. Una vez ajustados todos estos parámetros teóricos, se encontraron dos números de Reynolds críticos. Nuestros cálculos de DNS verifican que desde el inicio del flujo hasta primer umbral $Re_{C1} \approx 1.3 \times 10^3$ se captura el cambio en la tendencia de los parámetros teóricos. En esta región de bajos números de Reynolds la intensidad del torbellino decrece con el número de Reynolds. Sin embargo, a partir de este primer número de Reynolds crítico, la intensidad sube hasta un segundo número de Reynolds crítico. La justificación a este hecho se ha establecido a través de las simulaciones numéricas que muestran como aparecen inestabilidades aguas abajo del perfil que suponen una fuente extra de vorticidad al núcleo del vórtice lo que hace aumentar la intensidad del torbellino. Conforme aumentamos el número de Reynolds los valores de los parámetros teóricos S y b tienden a ser constantes experimentalmente para un segundo número Reynolds crítico Re_{C2} mayor que 10-20$\times 10^3$. En este sentido, no se ha aportado una evidencia para justificar este hecho, pero si se ha dado una explicación del posible mecanismo para que esto suceda. El flujo de aire cerca de la superficie del perfil aerodinámico tiene una región de recirculación en la capa límite laminar y el flujo es turbulento cerca de los bordes de entrada y salida, respectivamente. Por esta razón, la saturación del valor de S es el resultado de una proceso de evolución que resulta en una transición suave para lograr una completa separación de la burbuja laminar. Cuando este proceso ya está terminado en el número de Reynolds mayor que 10-20$\times 10^3$, el valor de la intensidad del vórtice debe permanecer constante.

Las observaciones hechas en el modelo B se pueden extender al modelo MS. En el caso del modelo MS, el parámetro n nos da información del decaimiento del vórtice. Hemos demostrado que este valor es mayor que 0,44 en todos los casos de estudio, por lo que el vórtice tiene siempre una forma con un defecto de velocidad axial en la estela. Además, este parámetro parece ser relevante para detectar el segundo número crítico de Reynolds. Adicionalmente, nuestros resultados se han comparado con los dados por otros autores a números de Reynolds muchos más elevados. Además de estos datos, se ha estudiado la tendencia de la evolución axial de dichos parámetros teóricos en función de la distancia axial, observando que para $Re_c = 7 \times 10^3$ decaen según aumenta el número de cuerdas, mientras que para $Re_c = 20 \times 10^3$ permanecen prácticamente constantes hasta la distancia axial máxima posible en nuestro montaje experimental. Con todo lo dicho anteriormente, se puede concluir que el número de Reynolds juega un papel importante en el análisis de estabilidad para los vórtices de estela de ala no sólo teniendo en cuenta el papel de los términos viscosos, sino también determinando los parámetros de entrada con los que se deben estudiar los flujos bases en función del número de Reynolds.

Finalmente, a partir del mismo montaje experimental, se ha realizado un estudio del efecto de soplado mediante inyección continua. El mecanismo de soplado se realiza perpendicularmente a la dirección de movimiento, y desde el extremo del mismo perfil aerodinámico NACA0012. Para ello, se han mecanizado en el plano medio del perfil dos orificios de 2mm de diámetro. Para realizar la inyección se ha usado una bomba de jeringa de uso veterinario cuya principal ventaja es que produce un caudal constante sin necesidad de un caudalímetro adicional. Además, nos permite variar el tipo de jeringa según el experimento a realizar adaptando así el tamaño de la jeringa según la velocidad del perfil NACA0012 y la relación de inyección que queremos forzar. Analizamos tres números de Reynolds Re_c y cuatro relaciones de inyección R_{jet}, la cual se determina por el cociente entre la velocidad de salida del soplado y la velocidad de arrastre del perfil aerodinámico, esto es, $R_{jet} = \frac{W_{jet}}{W_\infty}$.

A diferencia de otros autores que usan una inyección de alta relación de aspecto mediante una ranura mecanizada en el extremo del ala, nosotros hemos probado una configuración de baja relación de aspecto mediante chorros puntuales. Esta configuración de soplado resulta ser una buena candidata para reducir la fuerza de los vórtices de punta de ala a los números de Reynolds más bajos considerados, por ejemplo $Re_c =$

7×10^3. Para los números de Reynolds superiores hasta $Re_c = 20 \times 10^3$, el forzado tiene una influencia débil sobre la intensidad del vórtice en el campo cercano una vez que el proceso de formación del torbellino ya ha terminado, y especialmente a distancias axiales por encima de siete cuerdas detrás del ala. La razón de la presencia de dos decaimientos de fuerza diferentes dependiendo del número de Reynolds se explica por la capacidad del chorro continuo de eliminar el torbellino formado en el extremo del ala. De esta forma, se puede crear una superficie de vorticidad débil o fuerte que resulta en un circulación positiva o negativa en el extremo del perfil aerodinámico. Esto se traduce en un vórtice que puede ser contra-rotatorio o co-rotatorio a valores bajos o altos del número de Reynolds basado en la cuerda, Re_c, respectivamente. Este mecanismo de soplado hace que el torbellino del extremo del ala disminuya o permanezca constante cuando aplicamos diferentes proporciones de soplado R_{jet}. Este efecto es evidente en el número de Reynolds más bajo en el que observamos una fuerte decaimiento del vórtice. Por el contrario, el chorro continuo cambia las características para altos números de Reynolds solo en la zona donde se produce la formación del torbellino de extremo de ala, es decir, en la evolución del campo cercano (hasta siete cuerdas). Por el contrario, no hay un efecto apreciable sobre la intensidad del vórtice ni en su evolución axial a altos números de Reynolds.

En general, esta tesis contiene ajustes de parámetros teóricos, simulaciones numéricas y medidas experimentales de un modelo matemático de vórtices de extremo de ala en un perfil aerodinámico NACA0012.

La motivación de esta tesis ha sido la mejora del conocimiento de la dinámica de los vórtices de punta de ala, que es clave para diseñar diferentes estrategias para destruir estos vórtices en pistas de aterrizaje y despegue de aeropuertos. Los parámetros teóricos, tales como la fuerza del vórtice, así como la formación del vórtice en el campo cercano y lejano, son muy importantes para caracterizar estos vórtices de estela de ala. Los resultados presentados sobre la dinámica de los torbellinos en el extremo del ala dan una idea de que este estudio requiere una mayor profundidad y un tiempo de investigación superiores si se pretende dar cuenta de los numerosos fenómenos de difusión turbulenta que exhiben este tipo de flujos con fuerte rotación. A medida que avanzaba la investigación, se han hecho varias consideraciones que contemplan numerosas líneas de investigación potencial que podrían derivarse de este estudio. Describamos brevemente algunos de ellos.

Nuestra contribución más novedosa con respecto a la técnica experimental empleada para evitar mediciones complejas mediante la ténica PIV en un túnel de viento podría ser extendida al modelo MS. Sólo el modelo B se ha introducido en las ecuaciones diferenciales para describir las líneas de trayectoria detrás del ala, por lo que el modelo MS podría ser otro candidato. Para este fin, los resultados de este modelo son de gran interés para confirmar la tendencia de la descomposición del vórtice (que viene dado por el parámetro n).

Como trabajo futuro debe ser interesante extender las mediciones PIV de dos a tres dimensiones, dando así más detalles de la estructura de flujo en el canal de arrastre. Además, las implicaciones de los parámetros del modelo B junto con el modelo MS en función de los números de Reynolds han abierto nuevas preguntas. Éstas son esenciales para conocer la naturaleza del modo inestable observado en $Re = 1.3 \times 10^3$ y también para definir otro número de Reynolds crítico en el que la intensidad del torbellino permanece constante ($Re_c = 10\text{-}15 \times 10^3$).

Se debe explorar el control activo a diferentes relaciones de velocidad continua. Los parámetros R_jet pertenecientes al rango bajo son también más significativos para aplicaciones tecnológicas (R_jet del orden de 0,1 o menos). Además, no sólo se podría estudiar el chorro continuo sino también el chorro pulsante. En este sentido, se pueden abordar dos configuraciones: chorro sintético y chorro pulsante sobre una señal constante. Los modelos matemáticos dados en este estudio deben ser el punto de partida del trabajo futuro que corresponde a la respuesta óptima o la respuesta en frecuencia de los vórtices de arrastre. Los resultados de los análisis de estabilidad con los modos más inestables o donde se producen las mayores ganancias de las perturbaciones podrían ser implementados experimentalmente.

Por último, tres aspectos son de gran interés. En primer lugar, la influencia de la turbulencia de la corriente externa, por lo que una malla con diferentes superficies libres que promueven diferentes niveles de intensidad turbulentas podría ser acoplada aguas arriba del perfil aerodinámico en el canal de arrastre. Este estudio experimental explicaría también como la turbulencia de la corriente externa afecta a los posibles mecanismos

de control activo. En segundo lugar, la relación de la geometría del ala con los vórtices generados. Sólo se ha estudiado un ala con una relación de aspecto entre la cuerda y la envergadura $AR=2$, por lo que nuevos valores de la relación de aspecto podrían analizarse en detalle. Finalmente, el mecanismo de soplado se ha realizado solo de forma radial al actuar el chorro continuo en la dirección de la envergadura del perfil aerodinámico. Sin embargo, sería de gran interés para el análisis del control activo un estudio del mecanismo de soplado en la dirección axial, es decir, en la dirección en la cual el torbellino se forma y se desarrolla aguas abajo.

Experimental study in near-and far-field of trailing vortices and their active control

Abstract

In order to predict the axial development of the wingtip vortices' strength, an accurate theoretical model is required. Several experimental techniques have been used to that end, e.g. PIV or hotwire anemometry, but they imply a significant cost and effort. For this reason, we have carried out experiments using the smoke-wire technique to visualize smoke streaks in six planes perpendicular to the main stream flow direction. Using this visualization technique, we obtained quantitative information regarding the vortex velocity field by means of Batchelor's model for two chord based Reynolds numbers, $Re_c = 3.33 \cdot 10^4$ and 10^5. Therefore, this theoretical vortex model has been introduced in the integration of ordinary differential equations which describe the temporal evolution of streak lines as a function of two parameters: the swirl number, S, and the virtual axial origin, $\overline{z_0}$. We have applied two different procedures to minimize the distance between experimental and theoretical flow patterns: individual curve fitting at six different control planes in the streamwise direction as well as the global curve fitting which corresponds to all the control planes simultaneously. Both sets of results have been compared with those provided by del Pino et al. [2011a] and they are in good agreement. Finally, we have observed a weak influence of the Reynolds number on the values S and $\overline{z_0}$ at low-to-moderate Re_c. This experimental technique is proposed as a low cost alternative to characterising wingtip vortices based on flow visualizations.

Secondly, we present a detailed analysis of experimental and numerical results for the flow of wingtip vortices behind a NACA0012 airfoil. Particular attention is paid to a specific value of the angle of attack, $\alpha=9°$, and ultra-low and low chord-based Reynolds numbers ranging from $Re=0.3\times10^3$ to 20×10^3. Spatial-averaged two-dimensional PIV velocity profiles are compared for $Re=7\times10^3$ by using direct numerical simulations (DNS) up to eleven chords from the wing. Once we validate our results, we fit the theoretical parameters as function of Re. Five theoretical parameters are given from computational and experimental results: two corresponding to Batchelor's model and three regarding Moore & Saffman's model. Two critical Reynolds numbers were found. Our DNS computations verify that the onset of instability of the flow around the wing at the first threshold $Re_{C1} \approx 1.3\times10^3$ captures the change in the trend of theoretical parameters. In addition, the theoretical parameters appear to become constant experimentally for a second critical Reynolds number Re_{C2} greater than $10\text{-}20\times10^3$ as our results are compared with those given by other authors. Consequently, Reynolds number plays an important role in the stability analysis for trailing vortices not only taking into account viscous terms but also determining the input parameters for theoretical models.

Finally, we have carried out a study of the blowing effect of continuous jets that are perpendicular to the moving direction, and blowing from the tip of a NACA0012 airfoil. We analyze three Reynolds numbers Re and four jet-to-crossflow blowing ratios R_{jet}. We show how these jets are good candidates to reduce the strength of the wingtip vortices at the lowest Reynolds numbers considered, e.g. $Re = 7\times10^3$. For higher Reynolds numbers up to $Re=20\times10^3$, the forcing has a weak influence on the vortex strength in the near-field once the rolling-up process has already finished, and especially at axial distances greater than 7 chords behind the wing. The reason for the presence of two different strength decays depending on the Reynolds number is explained by the ability of the continuous jet to break the vorticity sheet creating a counter-rotating vortex or co-rotating vortex at low or high values of Re, respectively. This mechanism makes the wingtip vortex decrease or maintain its vortex strength as we apply different blowing ratios R_{jet}. This effect is evident at the lowest Reynolds number at which we observe a strong vortex decay. Conversely, the continuous jet changes the characteristics of the vortex flow in the formation and the near-field evolution

of the wingtip at high Reynolds numbers, but there is not an appreciable effect on the vortex strength and how it evolves downstream.

1
Introduction

1.1 Background

Saffman & Baker [1979] defined vortex as the finite volume of rotational fluid bounded by irrotational fluid or solid walls.

Figure 1.1: Vortex in draining bottle of water introduction [Robert, 2013].

Vortices are found in several applications in quotidian activities such as draining the bottle of water (see Figure 1.1) or the mixture of milk and coffee (see Figure 1.2).

Figure 1.2: Vortex coffee and milk mixture [Astrobob, 2015].

The biggest vortex observed in space is the storm in Saturn (see Figure 1.3 (a)). Also, vortices can be found in nature such as tornados or typhoons (see Figure 1.3 (b)).
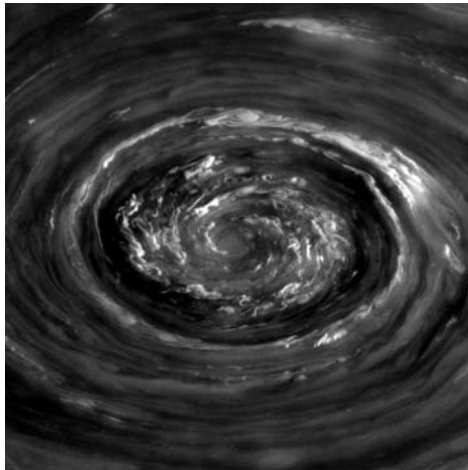
(a)

(b)

Figure 1.3: Vortex in nature: (a) storm in Saturn [NASA, 2012] and (b) tornado [James, 2015].

The study of vortices is present in different engineering applications such as the helicopters blade, propellers or aircraft wings, as shown in Figure 1.4. Concerning rotorcraft, there are also many interesting flow phenomena that arise from complex interactional aerodynamics for both hovering and forward flight. Many of these examples include blade-vortex interactions, vortex pairing, vortex breakdown, vortex-wake interactions and the interaction of several flow characteristics and the fuselage. They can adversely affect rotorcraft aeromechanic and aero-acoustic performance in a significant number of applications. Furthermore, the case of propellers, the so-called tip vortex cavitation widely present within blades at high rotational speeds so that it is considered, among others the first experimental observation of cavitation that appears on ships or boats. Cavitation is an important phenomenon to take into account for propeller design whose requirements are low noise and vibration levels.

Pennings et al. [2015a,b] analysed the sound production from cavitation and its relation with vortex strength. By using flow visualisations, Yang et al. [2012] described how wingtip vortices are also a relevant source of disturbances, noise and vibrations in wind turbines. These examples may occur at moderate or high Re (typically greater than $500{\times}10^3$). Also, and decreasing Re, small-to-medium scale wind turbines

(a)   (b)
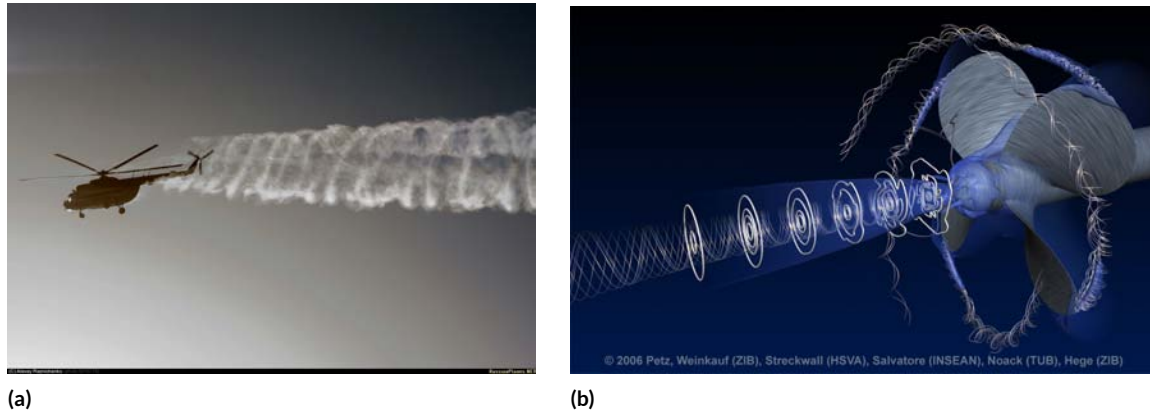
Figure 1.4: Vortex in engineering: (a) helicopters [Alexey, 2006] and (b) propellers [Pet, 2006].

and unmanned aerial vehicles (UAVs) belong to the range of lower Reynolds numbers than those given for aerodynamic purposes [e.g. see Yarusevych et al., 2006, 2009]. These authors studied the boundary layer separation with the use of aluminium NACA0025 airfoil due to the presence of strongly separated flows and separation bubbles at nominally pre-stall angles of attack in the range of Re between 55×10^3 and 210×10^3.

Other recent research in UAVs deals with aerodynamic measurements for wings under subsonic conditions, showing different aerodynamic characteristics as the aspect ratio of the airfoil is varied at moderate, low and ultra-low Re [see Sun & Boyd, 2004; Jones et al., 2008; Ananda et al., 2015, and their references therein]. Besides, there has been a lot of research in recent years regarding ultra-low Reynolds numbers due to its high effect on micro air vehicles, as reported in the thorough review by Shyy et al. [2010]. In particular, Taira & Colonius [2009a,b] showed that active flow control over a flat plate enhanced lift at post-stall angles of attack by changing the 3D dynamics of the wake vortices at Reynolds numbers between 300-500.

Figure 1.5: Boeing B-757 with wingtip vortex on clouds [Aeroclub, 2006].

Finally, in Figure 1.5 it can be observed the wingtip vortex developed behind aircraft. *The study of these vortices and their control is the purpose of this dissertation.*

1.2 Definition

As mentioned above, vortices form because of the difference in pressure between the upper and lower surfaces of a wing which is operating at a positive lift. Since pressure is a continuous function, it becomes equal at the wingtips. In other words, the behaviour of airflow is to move from the lower wing surface around the wingtip to the upper surface (from the region of high pressure to the area of low pressure). In addition, there is an oncoming free-stream flow of air approaching the wing (see Figure 1.6). If these two movements of air are combined, there is an inclined inward flow of air on the upper wing surface and an inclined outward flow of air on the lower wing surface. The flow is strongest at the wingtips and decreases to zero at the midspan point as evidenced by the flow direction there being parallel to the free-stream direction [Pilot Friends, 2000].

Vortices are an unavoidable effect of flight, which appear behind the wing with a bounded length. The vortices strength is due to the lift force, as reported in Prandtl & Tietjens [1957]. That is the reason why this phenomenon is especially relevant during take-off and landing operations. In these cases, when aircraft have just used the airport runway, the following aircraft might find two counter-rotating vortices. Unfortunately, this huge rotation of airflow patterns always destabilises the following aircraft. Consequently, trailing vortices have a mighty influence on the air traffic control of airport runways, and they have justified the research interest in this topic since the 1960s [Spalart, 1998]. However, aeronautical engineers are still searching for different technological strategies to breakdown these wingtip vortices.
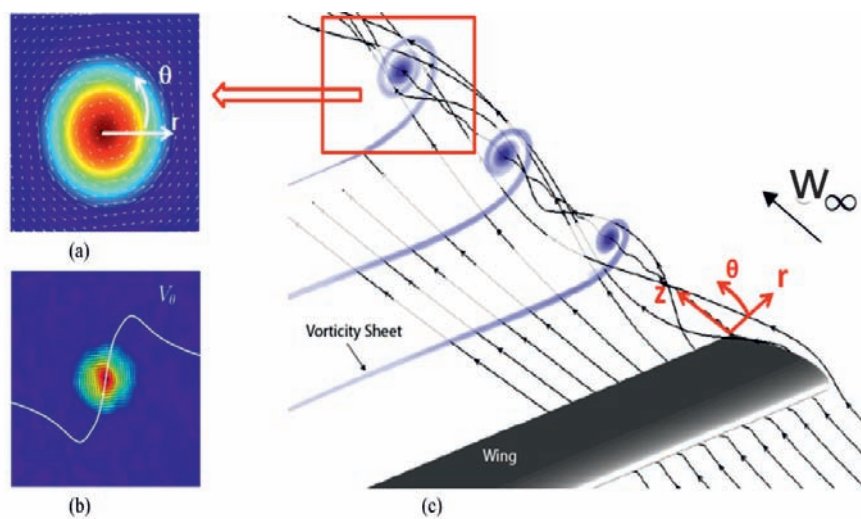
Figure 1.6: Vortex scheme: vortex reference system (a), azimuthal velocity representation (b), vortex roll-up reference system (c).

Two regions characterise the vortex produced at the wingtip. In the inner region called the core, the mean tangential velocity varies approximately proportionally with the radius from zero at the centre to a maximum at the edge of the core (see in Figure 1.6 and the inset shown in (b)). Circulation varies proportionally with the radius squared until it reaches a maximum at the edge of the core. At the outer region, the mean tangential velocity varies approximately with inverse of the radius and asymptotically approaches a value of zero, and the circulation attains a constant value as the radius increases in the outer region [Devenport & Zsoldos, 1992]. Using the reference system depicted in Figure 1.6 (a and c) and the vortex velocity and vorticity fields

presented in (a), amongst other things, the radial profiles of azimuthal velocity can be obtained.

Willian Lanchester[*] described wingtip vortices for the first time in 1907 only four years after the first flight by Wright brothers. They were described as counter-rotating vortices that trail from the wingtip of aircraft. Batchelor [1964] published the first model of trailing vortices, taking into consideration the axial velocity component. He studied the vortex wake far downstream where it decays under the action of viscosity, and its radius is $O(\nu z/W_\infty)^{\frac{1}{2}}$. Here, ν denotes kinematic viscosity, z is the distance downstream of the wing and W_∞ is the velocity at infinity in wing-fixed coordinates. It was found that viscous effects produced an axial velocity deficit due to the dissipation of the kinetic energy of the cross-flow by the viscosity and the transference of induced drag effect from the kinetic energy of rotation to a momentum deficit. However, Batchelor's calculation of the influence of viscosity will not be applicable until $(\nu/W)^{\frac{1}{2}} \sim r$, where r is a characteristic radius of the inviscid rolled up vortex. A reasonable value of r is $\frac{1}{10}b$, where b is the wing span, and hence the downstream distance is $\sim 0.01cRe_cA^2$, where c is the chord, $Re_c = \frac{Wc}{\nu}$ is the based chord Reynolds number, and A is the aspect ratio.

Later, Moore & Saffman [1973] published one theoretical model taking into account the roll-up process in the formation of trailing vortices. This model based on experimental visualisations and quantitative measurements acquired by Olsen [1970], using Laser Doppler Anemometry (LDA) and emerged to improve the discrepancies between Batchelor's model and the experimental results in the near-field. Besides Batchelor's model was extended to azimuthal velocity profiles decaying as an arbitrary power of the radius r of the vortex. Uberoi [1979] developed a theoretical study in which the dynamics of an infinitely long one-dimensional vortex and a swirl is compared with to that from a semi-infinitely long trailing vortex and trailing swirl. He found that with increasing distance, the change in the axial velocity difference between the core of the trailing vortex and the surrounding region causes radial convection with some associated axial convection of angular momentum. As a result, under most conditions of interest, this mechanism was the dominant one to explain the decrease of vortex strength and the increment of the core diffusion. In other words, the radial position at which the maximum azimuthal velocity is achieved increases, whereas the vortex strength decreases, with the axial distance. Based on theoretical considerations and experimental observations, McCormick et al. [1968] showed that the axial velocity difference between the vortex core and the surrounding region is necessary for the level of turbulence to remain constant. Further works have been published to complement this model, such as the solution provided by Chadwick [2006], which arises from the description of the horseshoe vortex. His model of streamwise decay of velocity is different to that Batchelor. Apart from practical applications such as vortex control, we need to take into account the understanding of fundamental mechanisms responsible for the strong stability of vortex flows [Jacquin & Pantano, 2002]. Many numerical studies have given new insights into this phenomenon.

Heyes et al. [2004] observed that, although in the near-field the vortex decayed more rapidly as the free-stream turbulence increased, in the far-field, the rate of decay in the turbulent free-streams were indistinguishable from that in the laminar free-stream case. Finally they concluded that the free-stream turbulence altered vortex formation and roll-up, but did not effect on the fully formed vortex.

Zhou et al. [2004] reported that the tip vortex formation was more intense as the angle of attack increased from eight degrees with an attached flow to sixteen degrees with separation flow. In general, the more the

---

[*]Engineering and Mathematician researcher from England (1868-1946) who worked in vehicles engineering field, aerodynamic and operative investigation.

angle of attack, the stronger tip vortex, as quantified by its increasing maximum streamwise vorticity and tangential velocity. Thus, the spatial scattering of the tip vortex was tiny in the absence of leading edge flow separation from the wing but increased markedly with separation. del Pino et al. [2011b] carried out experimental measurements of the axial evolution of trailing vortices, identifying the path of the vortex core and introduced a new parameter to Batchelor's, $overlinez_{0B}$, and Moore & Saffman's models, $\overline{z}_{0MS}$. Both consist of a virtual axial origin of the vortex taking into account the roll-up process. These parameters are as a function of Re and are necessary to compute a curve fitting in (Batchelor and Moore & Saffman) theoretical models. Finally, five variables must be taken into account. Two of them for the Batchelor model (vortex strength, S, and virtual origin, $\overline{z}_{0B}$), and three for Moore & Saffman's model (vortex strength, b, vortex decay exponent, n, and virtual origin, $\overline{z}_{0MS}$). In this research work, they found that accurately, Moore & Saffman's model profiles better describe the wake-like axial flows near the centre of the vortex than the much-studied Batchelor vortex does, as it is also corroborated later by Feys & Maslowe [2014, 2016]. Moreover, the core axial flow is wake-like when n belongs to the range 0.44 and 1.0, but the flow in the vortex core is jet-like for n lower than 0.44. For this reason, they considered that reporting the function n against Reynolds number could lead to a better understanding of these vortical flow structures.

Regarding ground effects, Sun & Daichin [2011] analysed (studied) the vorticity distributions and lift/drag forces and they concluded that the dissipation of tip vortices for small ground clearance ($h^* = 0.1$, where $h^* = h/c$) is faster than that for larger ground clearance ($h^* = 1.0$). Thus, the vortex core shifts outboard of the wingtip due to it being bound by the ground, and the outboard displacement decreases with the reduction of the angle of attack.

1.3   Meandering
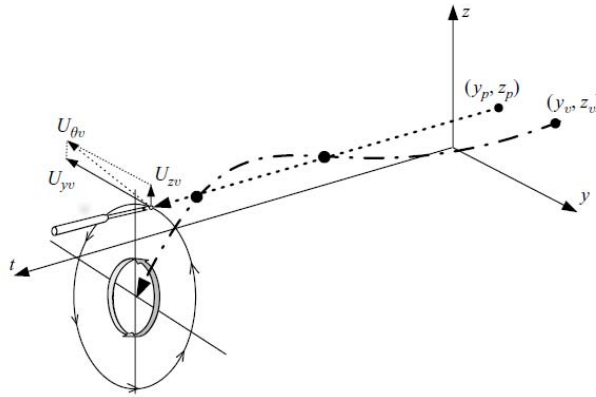
Figure 1.7: Sketch defining vortex position (y_v, z_v) in the (y, z)-plane, probe position (y_p, z_p) in the (y, z)-plane and the velocity components U_{yv}, U_{zv} induced by the vortex at the probe position as the vortex meanders in time [Bailey & Tavoularis, 2008].

Vortex meandering is defined as a random movement of the vortex core introduces several drawbacks in experimental studies of vortices, especially when attempting to measure the velocity using fixed probes (see Figure 1.7). Gaspareck [1960]; Orloff [1974] described these problems firstly and found that the trajectory of the vortex moved when a small diameter probe was inserted into the core, and Mason & Marchman [1972] also reported that a probe changed the vortex path but only if it was pitched or yawed relative to the freestream direction. The lack of turbulence measurements was a result of the fact that tip vortices generated in

wind tunnels tend to meander (i.e. their core location is a function of time) and they are firmly influenced by probe interference. Meandering causes a fixed probe to substantially overestimate turbulence stresses in regions where there are significant mean velocity gradients across the vortex. Baker et al. [1974] conducted experiments in trailing vortices generated by a rectangular wing in a water tunnel employing LDA. They found that vortex meandering decreased the maximum tangential velocities by 30% and increased the measured core radius by a factor of 2.2. Chigier & Corsigilia [1972] & Corsiglia et al. [1973] conducted triple hot-wire measurements in trailing vortex, and they observed a spanwise meandering of about ± 2 chord lengths. As a result, mean-velocity measurements carried out with a fixed hot-wire probe underestimated the peak tangential velocity by over 50%. Baker et al. [1974] attributed the meandering to free-stream turbulence. Singh & Uberoi [1976] measured the vortex generated by a laminar flow over half wing with fixed hot-wire probes. They observed relatively high-frequency unsteadiness in the core due to laminar flow instabilities but little or no low-frequency meandering. They inferred that the laminar flow instabilities had symmetric and helical modes with wavelengths of the same order as the core diameter. Later, Stifle & Panton [1991] examined the effects of passing a small moving wire through the centre (to cut the vortex) of a tip vortex produced by a NACA0012 airfoil profile. They found that disturbances introduced into the vortex core propagated both upstream and downstream with smaller disturbances generated by a slower moving wire.

Devenport et al. [1996] used an analytical approach to determine the magnitude of vortex meandering and to correct the hot-wire measurements. They found that errors in time-averaged measurements due to meandering were significant only within the vortex core, and that meandering occurred in broadband, low-frequency range. Heyes et al. [2004] confirmed the validity of this approach studying a trailing vortex in free-stream turbulence from the particle image velocimetry and evaluated meandering effects. They found a 12.5% over-prediction of the core radius and a 6% under-prediction of the peak tangential velocity and the errors were larger at lower angles of attack. They also found that the meandering amplitude increases linearly with streamwise distance and increase the angle of attack produces a direct reduction so that they concluded that the mechanism responsible for meandering is not self-induced, as had been proposed by Rokhsaz et al. [2000]. More recent experimental studies have corroborated this connection between free-stream turbulence and the amplitude of vortex meandering, Beninati & Marshall [2005] were able to isolate the effects of free-stream turbulence from effects of meandering due to wind tunnel unsteadiness and model vibration, by using a specially designed, low-disturbance vortex generator. They noted that turbulence-induced bending waves in the vortex had a wavelength compatible with the spacing of azimuthally aligned turbulent structures observed in the numerical simulations of Marshall & Beninati [2005] and concluded that it is these structures that induce bending waves into the vortex. In contrast, Bailey et al. [2006] noted that the free-stream turbulence had little effect on the wingtip vortex formation process, noting only the introduction of additional unsteadiness into the vortex.

De Souza & Faghani [2001] experimented near-field employing a rectangular NACA-0012 and investigated Reynolds dependence of vortex properties such as vorticity or core size and the vortex meandering and its influence on high turbulence levels in the core region. They concluded that for a given wingtip, the total turbulence intensity is almost constant. When the meandering effect is removed, the turbulence level increases. Therefore, the fraction of turbulence due to meandering seems to decrease with based chord Reynolds number, Re_c. Turbulence levels were not a good enough indicator of vortex meandering, and a more sensitive tool was required. To that end, De Souza & Faghani [2001] applied Proper Bi-Orthogonal Decomposition (Bi-POD) that is a statistical tool based on the two-point space-time correlations which re-

duce to a Fourier Transform for a stationary and homogeneous flow. This technique shows the vortex flow to be highly coherent for all tip shapes, but somewhat less so for the square tip. These results may indicate that the meandering effect was influenced strongly for the elliptic and round tips, but weakly for square tips.
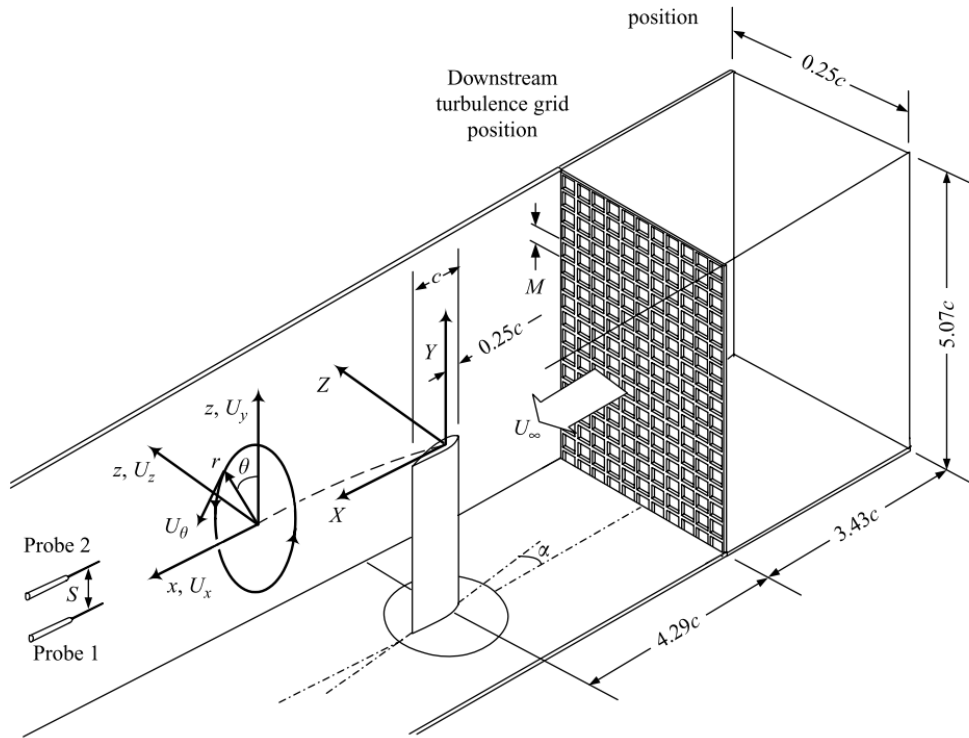
Figure 1.8: Sketch of the experimental arrangement illustrating the coordinate system by Bailey & Tavoularis [2008].

Bailey & Tavoularis [2008] carried out a novel analysis technique which can quantify the vortex meandering and reconstruct the velocity profile of the vortex in the meandering frame of reference (see Figure 1.8). They combined these results to provide a thorough overview of the vortex formation and development in the presence of free-stream turbulence, and they reported that increasing the free-stream turbulence led to increasing the amplitude of vortex meandering, but its wavelength was insensitive to changes in the free-stream condition. They also indicated that the vortex decay increased with the free-stream turbulence, but this last has not a strong influence on the radial distance where the peak of the azimuthal velocity appeared. Igarashi et al. [2010] gave quantitative information of the vortex meandering phenomena by using a Stereoscopic Particle Image Velocimetry (*SPIV*) and a rectangular NACA0012 airfoil as a vortex generator. By tracking the vortex core at every instantaneous frame, the *SPIV* measurement results confirmed the findings of previous studies regarding the characteristics of the wingtip vortex in the near-field, though conversely, they did not observe a direct relationship between the vorticity and meandering amplitude. Jammy et al. [2014] carried out direct numerical simulations of the Batchelor vortex in the presence of freely-decaying turbulence, under periodic and symmetric boundary conditions. They estimated that vortex meandering was strongly influenced by the boundary conditions, and that the modelling of a free vortex by a 'vortex in a box' may not be valid, even if the effect of the walls upon the vortex appears to be small at the leading order. Finally, del Pino et al. [2011a] found low frequencies in the vortex core which were in agreement with previous work. This analysis was performed using Proper Orthogonal Decomposition (POD) from flow visualisations. Using the q-vortex model, Mao & Sherwin [2012] explained the onset of this random movement of the vortex core based on the optimal perturbations which correspond to the continuous eigenmodes. These are responsi-

ble for making the vortex vibrate around its initial location. More recently, Viola et al. [2016] gave another explanation for the meandering effect as a result of the growth of nonlinear instabilities from Batchelor's model. The use of more realistic theoretical models, and how they depend on the Reynolds number, should help researchers to give plausible explanations to understand this phenomenon better.

1.4   NEAR-FIELD

The difference between near- and far-field in wingtip vortices is highly subgective. Following the criteria are given by Francis [1976] and Albano et al. [2003], one can characterise the wingtip vortex in terms of its life which spatially corresponds to three different areas: near-, mid- and far-field. While the formation of the wingtip vortex and its roll-up process belongs to the near-field, the mid- and far-field are not defined accurately due to the variety of airfoils. For this reason, Gerz et al. [2001] considered the mid-field as the region where the wingtip vortex circulation decays at a relatively small rate (diffusion regime), while the far-field shows instability mechanisms which change the structure of wingtip vortices. However, this distinction is not accurate since vortex meandering can be considered the result of instabilities acting on the wingtip vortex. Therefore, we find in the title of this work near- and far-field because the axial evolution of the wingtip vortex will be analysed up to 40 chords.

As stated before, the inquiry of the near-field behaviour of a tip vortex behind a low aspect ratio wing, attached to an axisymmetric body, is critical to detect the formation of the wingtip vortex and the roll-up process accordingly. A sketch of this mechanism, from Computational Fluid Dynamics (CFD), is presented in Figure 1.9.
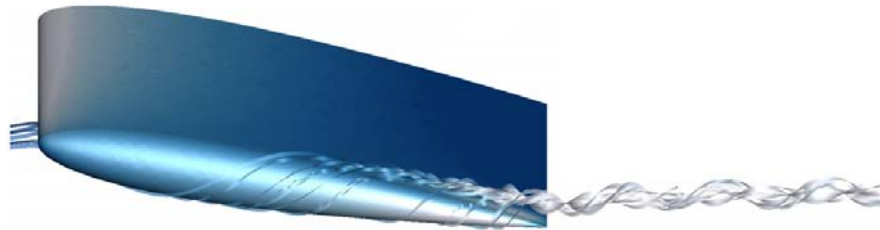
Figure 1.9: Wingtip vortex roll-up [Lombard et al., 2015].

The wingtip vortex formation was investigated by Shekarriz et al. [1993] and their results indicated that roll-up was almost complete at the trailing edge and that less than 66% of the root circulation was entrained into the vortex. At $Re_c = 2.2 \times 10^5$, the spatially averaged tangential velocity agrees well with the existing models. However at $Re_c < 10^5$ the entire flow structure, including the overall circulation, fluctuated from one experiment to the next. The tangential velocity profiles seemed to be dominated by secondary vortices (SV) located mainly outside of the vortex core. The axial velocity deficit increased with incidence angle and decreasing Re_c. Shekarriz et al. [1993] also deduced that the theoretical predictions of the axial velocity developed by Batchelor [1964] and Moore & Saffman [1973] based on the assumption that the axial velocity perturbation $w - W_\infty$ and the azimuthal velocity V_θ, are much smaller than W_∞, it is not necessarily true in the near-field.

Chow et al. [1997] studied the roll-up of wingtip vortex at $Re_c = 4.6 \times 10^6$. They succeeded in inducing a favourable axial pressure gradient in the core from the development of the cross-flow velocities with

chord-wise distance, resulting in acceleration of the core centerline fluid to 1.77 times the free-stream velocity. The factors contributing to this high level of core axial velocity were the strong influence of the wind tunnel model, high Reynolds numbers, and the smoothness of the tip geometry. Hence, squared-off tips behaved differently because of turbulence, thus originating tip-boundary layers which wrap into the roll-up of the vortex. Birch & Lee [2003] characterised the formation and growth of a tip vortex at $Re_c \leq 3.25 \times 10^5$ along the tip of a rectangular high-lift wing and its subsequent development in the near-field (up to 1.5 chords downstream of the trailing edge of the wing) by using a small seven-hole pressure probe and particle image velocimetry. Multiple secondary vortex structures dominate the tip region, and the roll-up was almost complete at the trailing edge. The strength of the vortex remained nearly constant up to 1.5 chords downstream of the trailing edge. For instance, Margaris & Gursul [2009] presented the roll-up process in reference to vorticity as shown in Figure 1.10.
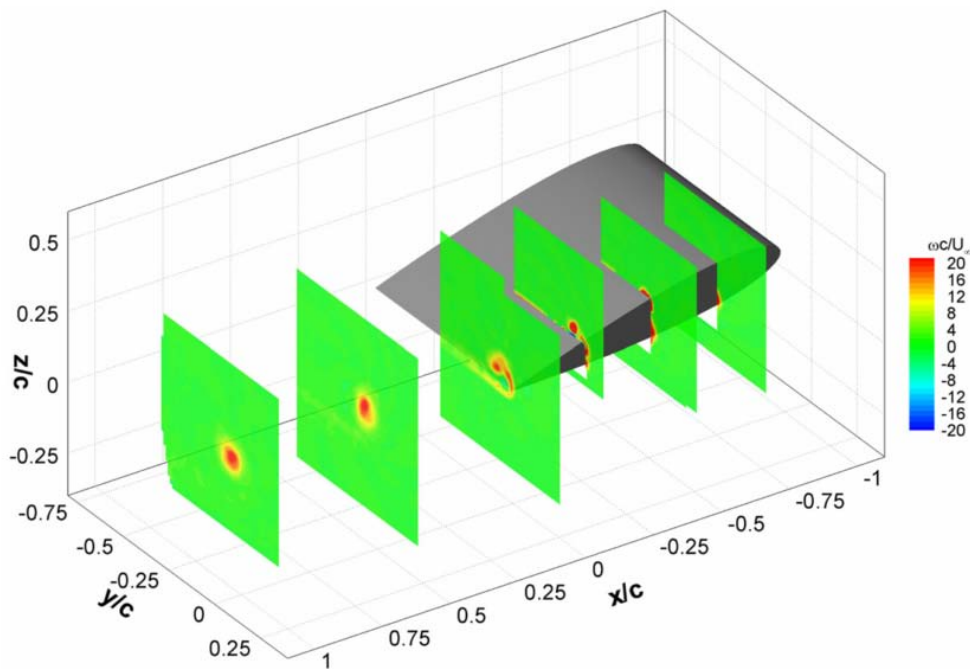
Figure 1.10: Vorticity fields in a near-field for the square tip referenced by Margaris & Gursul [2009].

Birch et al. [2004] investigated the three-dimensional flow structure of a tip vortex generated in the near wake behind both a rectangular, square-tipped NACA0015 and a high-lift cambered airfoil (see Figure 1.11). For the two airfoils tested, the interaction between the multiple secondary vortices and the primary vortex dominated the tip region. The roll-up process was almost complete at $x/c \sim 1.5$, and the overall circulation of the tip vortex remained nearly constant up to $x/c = 3$ (two chord lengths downstream of the trailing edge). As the airfoil incidence increased, the increase in the lift force resulted in a linear increase in the vortex strength and the peak values of the tangential velocity and vorticity. The vortex radius, however, did not appear to have an explicit dependence on the vortex intensity. Depending on the angle of attack, the axial velocity in the core could be either greater than or less than W_∞, that is, either jet-like or wake-like. For the NACA0015 airfoil, the induced drag contributed to less than 20% of the total drag and had a smaller tangential velocity but the same core size compared to a cambered airfoil.

Ahmadi-Baloutaki et al. [2015] investigated the effect of external free-stream turbulence in the near-field of a wingtip vortex and the influence of aerodynamic forces. They found that the free-stream turbulence,
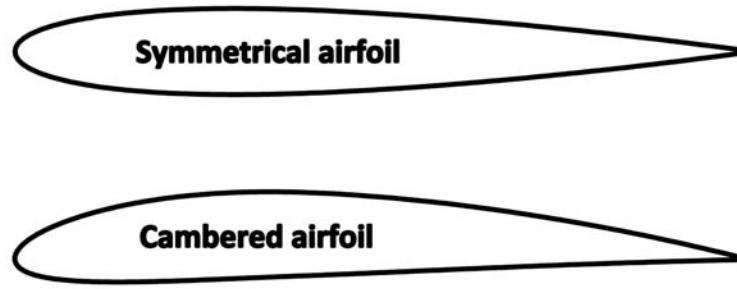
Figure 1.11: Cambered airfoil and symmetrical airfoil used by Birch et al. [2004].

with 4.5% turbulence intensity, tends to increase the vortex diffusion at x/c = 0.77 and 1.03. The inboard and upward movement of the tip vortex downstream of the wing was not significantly affected by the introduction of free-stream turbulence, whereas external free-stream turbulence increased the turbulence intensity peak. External turbulence also increased the tangential velocity and vortex circulation concerning the streamwise distance at radial locations far from the vortex centre. Lombard et al. [2015] studied the development of a wingtip vortex in the near wake (see Figure 1.9) using Large Eddy Simulation (*LES*) in combination with the large Reynolds numbers (Re_c =1.2×10^6). They presented Vanishing Viscosity–implicit LES (*SVV-iLES*) solver to perform the simulations, and they explained how the issues of implementation and mesh generation could be overcome, as well as highlight the benefits that these schemes can have for industrial problems. Chow et al. [1997] compared the results to experimental data reporting a good agreement. Overall, the results showed the potential of this method to compute the large-scale features of the flow, without the use of explicit turbulence and sub-grid scale models. The use of an implicit LES presents a significant advantage over these procedures, given that only two parameters are needed to control regularisation and stability of the simulation.

Dacles-Mariani et al. [1995] and Craft et al. [2005] have studied the near-field vortex development using a RANS formulation with the Baldwin-Barth turbulence model. They examined the effects of numerical schemes, grid requirements, and turbulence model modifications while resolving the vortex formation and roll-up process. They were able to demonstrate that from 15 points per vortex core diameter, fifth order spatial accuracy for inviscid terms and a modification of the turbulence model, the mean flow characteristics could be reasonably captured. It was, however, concluded that the use of isotropic turbulence closure could be deficient in accurately representing the turbulence field.

1.5   Vortex Pairs

The merging phenomenon occurs when two vortices of the same sign with (almost) parallel axes, and within a certain critical distance of each other, mix a substantial portion of their core vorticity to become a single vortex [Reinaud & Dritschel, 2005]. Figure 1.12 shows a sketch of a typical trailing vortex system generated by an aircraft in take-off or landing configurations. There are two co-rotating vortices generated at each wings (at the tip and the flap) and they spin around each other by mutual induction, and merge into a single one over a distance of 5–10 wing spans [see Meunier et al., 2005].
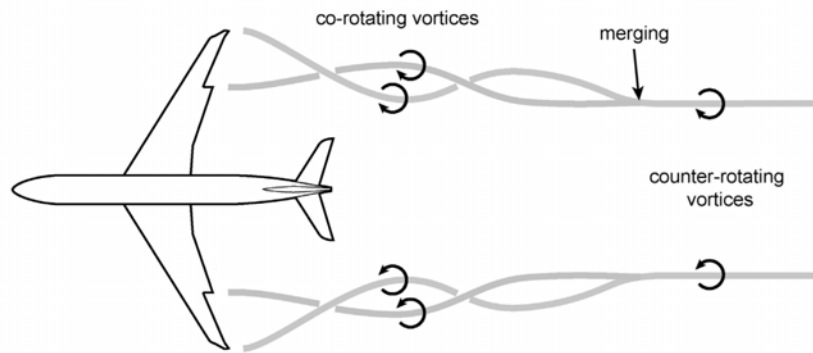
Figure 1.12: Schematic of a typical vortex wake of a transport aircraft in high-lift configuration (flaps deflected) [Meunier et al., 2005].

The extensive relevant literature related to wingtip vortices includes several studies dedicated to the interaction of equal-strength co-rotating pairs. Brandt & Iversen [1977]; Bilanin et al. [1977] established the essential features of this flow through low-Reynolds-number visualisations of vortices generated by pairs of unswept rectangular wings. The wings were placed tip-to-tip by mounting them on opposite or adjacent walls of a rectangular test section (see Figure 1.13). With the wings at equal and opposite angles of attack, equal-strength co-rotating tip vortices are formed in a spiral around each other under their mutual induction and ultimately merge to form a single vortex. The authors observed the initially laminar appearance of the un-merged vortex cores, the distortion of the regions of smoke containing the cores and rapid changes in the angular position of the vortex cores as a merge is approached, the generation of unsteadiness during the merging process, and the formation of a double-spiral structure in the smoke patterns downstream of the merging point that penetrated quite deeply into the new core. The problem was that there had been relatively few quantitative measurements to relate these observations to the physical structure in the velocity or turbulence fields. Corsigilia et al. [1978] attempted to report the mean flow structure produced by a perpendicular-wing configuration using LDA with conditional averaging to eliminate meandering effects, but seeding problems and uncertainty obscured much of the structure they were attempting to reveal.
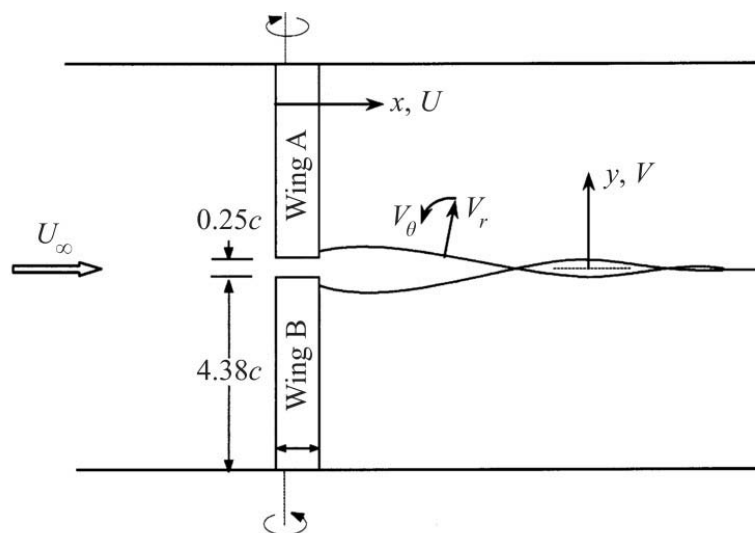
Figure 1.13: Experimental setup to produce vortex pairs [Devenport et al., 1999].

Devenport et al. [1999] performed experiments on a co-rotating wingtip vortex pair generated employing two rectangular NACA0012 wings in a split-wing configuration (see Figure 1.13). He carried out measurements of mean-velocity and turbulence from hot wires and quantified the small-amplitude meandering motions of the vortices. Employing the method of Devenport et al. [1996] to account for their effects on the results, the measurements revealed, for the first time, the complex turbulence structure of this flow. The vortices spiral around each other and they merge near 20 chord lengths downstream of the generating wings. As merger is approached the vortices lose their axisymmetry, so their cores develop asymmetric tangential velocity fields and take on an elliptical appearance. The formation of filaments in the vorticity field, previously predicted by Melander et al. [1988] for analogous two-dimensional vortex interactions, was also observed. Devenport et al. [1999] compared it with the single wingtip vortex studied by Devenport et al. [1996] using the present configuration but with one of the half-wings removed. This comparison enabled effects associated with interactions between the co-rotating vortices to be distinguished from those related to individual vortex development. Similar comparisons were made using the results of Devenport et al. [1997] who studied the turbulence structure of a pair of equal-strength counter-rotating vortices generated using the present configuration but with both wings set at the same angle of attack. Jacquin et al. [2005] studied the dynamics and final decay of the counter-rotating vortex pair in the far wake of an aircraft, involving turbulent dissipation and different three-dimensional instabilities. Meunier et al. [2005] observed the interaction of co-rotating vortices, in configurations similar to those found in the extended near wake of conventional transport aircraft. In the near-field, the vortex sheet quickly rolls up into a set of discrete vortices, which subsequently interact and merge to form a single vortex behind each wing in the aircraft's far-wake. They reviewed the two-dimensional dynamics in detail, and they analysed different stages of joining establishing a merging criterion, including a discussion of the physical origin of merging, and assess the properties of the final vortex. Thus, they studied the three-dimensional effects, in particular, a short-wavelength elliptic instability, which can arise in the co-rotating vortices before merging. Recently, van Jaarsveld et al. [2011] observed that the single vortex could be described by the 'two length scales' model of Jacquin et al. [2001] and a vortex core, which decays like a Lamb–Oseen vortex, and is embedded in a region with an almost constant radius and a much lower azimuthal velocity. For the turbulence levels and the test section length that they used, the single-vortex behaviour is independent from the external turbulence and in contrast with the decay of the vortex pair that strongly depends on the external turbulence. In the initial stages of the vortex pair evolution, the vortices decay due to the cancellation of vorticity at the symmetry plane. At a later date, Crow oscillations are observed, followed by a breakdown of the vortices. This vortex breakdown might be due to direct turbulent action. The observed behaviour is in agreement with the theoretical model of Crow & Bate [1976].
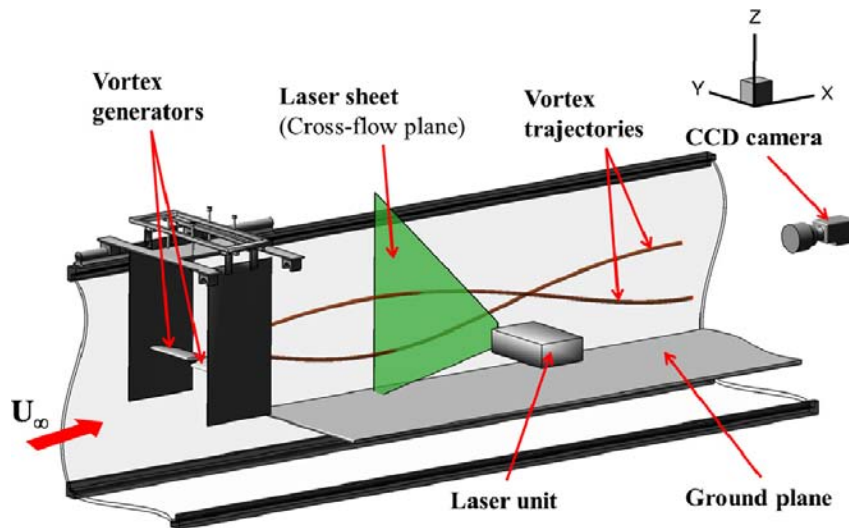
Figure 1.14: Schematic layout of the water tunnel facility [Wang et al., 2016].

Recently, Wang et al. [2016] carried out an investigation of co-rotating vortex merger in ground proximity by water tunnel experiments, as depicted in Figure 1.14. The experiments were aimed to investigate the merging process of co-rotating wake vortices in ground effect. The evolution of vortex pair was attained by means of PIV at different downstream locations. The main finding was that ground effect promotes the merging process and accelerates the vortices' rotation around one another. In addition, vertical movements, known as vortex rebound, and lateral movements were observed. The ground effect also leads to the emergence of a secondary vortex (SV), which adds complexity to the vortex system. The results showed the vortex merging and the rebounding of a co-rotating vortex pair are successfully predicted, and this model improves this prediction of vortex orientation and lateral motion

1.6 Vortex Stability

Many authors have studied the stability of wingtip vortices using two different approaches. Firstly, researchers analyse which is the most unstable mode of trailing vortices by means of line methods and long-wavenumber disturbances [Crouch, 1997; Fabre et al., 2002]. These works concluded that the most unstable mode is always Crow instability. This mechanism has been verified theoretically, and later tested numerically and experimentally [Crouch, 1997; Crouch et al., 2001]. Secondly, other theoretical studies focused on the stability problem from isolated vortices. In general, trailing vortices have been modelled by a Gaussian vortex with a Gaussian axial velocity. This model called q-vortex is as an approximation of Batchelor's model [Batchelor, 1964], where the velocity field does not depend on the axial coordinate. Despite the consideration of these unrealistic assumptions, q-vortex is a widely used model of stability studies, as can be seen in the articles published by Olendraru & Sellier [2002], Parras & Fernandez-Feria [2007] or Heaton [2007]. Researchers such as Fabre and his collaborators are intrigued with establishing the relationship between the introduction of axial flow in the velocity field of the trailing vortices, and their stability analyses [see Fabre & Jacquin, 2004; Fabre & Dizès, 2008; Fabre et al., 2008]. Obviously, these studies strongly depend on the base flow. Mayer & Powell [1992] characterised several unstable modes for the q-vortex model. Fabre & Jacquin [2004] also determined the only kind of unstable modes under flight conditions in the q-vortex for large q, where q is the swirl number which sets the relative magnitudes of the axial and azimuthal velocity distributions. Other authors attribute a precise mechanism for breaking the vortex to instabilities formed in the transient growth, such as Heaton & Peake [2007] who analysed the q-vortex in the inviscid limit, finding

that the most unstable modes correspond to the helical ones, with azimuthal wavenumber m=1. Besides, Tendero et al. [2015] gave plausible control strategies to destroy the vortex wake based on point vortices (2D) and vortex filaments (3D). However, less information is provided for regarding Moore & Saffman's model.

Ragab & Sreedhar [1995]; Jacquin & Pantano [2002] conduct an investigation about the turbulent evolution at $q = 1$ for Batchelor's vortex using direct numerical simulation (DNS) and large eddy simulation (LES). They established that while the helical normal mode instabilities play a dominant role in the early stages of the evolution, the nonlinear interactions with the mean flow result in saturation (during which the axial velocity has diminished significantly) and eventual decay. The initial swirl, in this case, is moderate enough to cause the growth of the instabilities, but the relaxation to a stable high q configuration is very rapid. Furthermore, Duraisamy & Lele [2008] studied the temporal evolution of a low swirl-number, q for the turbulent Batchelor vortex using pseudospectral DNS, with a particular focus on the mechanisms that have a significant influence on the transport of axial and angular momentum. Also, they observed the creation of a polarised vortex layer due to excitation of normal mode instabilities, the radial growth of the helical structures inside the vortex core, and the action of axial shear and differential rotation. Feys & Maslowe [2014] studied the stability of a trailing vortices using mean flow profiles given by an approximate solution of the Navier-Stokes equations, and they found that the Moore-Saffman profiles better describe the jet-like and wake-like axial flows near the centre of the vortex than does the much-studied Batchelor vortex. Not only they found growth rates for unstable perturbations and different values of n but also the growth rates are larger than those obtained for the Batchelor vortex. The most significant amplification is near $n = 0.5$, belonging to the elliptic loading. Very recently, Feys & Maslowe [2016] also demonstrated using Moore & Saffman's model again the distribution and intensity of the axial flow has a significant effect on the elliptical instability (n=0.5) of a trailing vortex, plus associated stability characteristics which depend strongly on the value of n.

Ortega et al. [2003]carried out an experimental study of instability in the wake of similar configuration to that of Fabre et al. [2002]. They used a rectangular plan-form wing, the outboard pair of vortices was produced at the wingtips and the inboard pair of vortices generated by triangular flap extensions to the trailing edge. A rapidly growing instability developed within 20 spans downstream of the wing and converted the consistent two-dimensional flow to a three-dimensional one. The authors argued that these results in rapid reduction in the 2D rotational kinetic energy and therefore the hazard posed by the wake. In this experiment, the instability developed naturally, with perturbations to the vortices caused by background turbulence in the towing tank.

1.7 Wingtip Control

As commented above, wingtip vortices with axial velocity appear due to flight and finite length of the wings so the higher lift force, the greater the intensity of trailing vortices. Since lift force is more influenced during taking off and landing, these vortices strongly affect the frequencies of these manoeuvres, thus, reducing the operation ability of airports. Consequently, there is an increase in the environmental and acoustic pollution due to aircraft remaining on runways. For these reasons, reducing the vortex strength or developing new mechanisms to destroy its rotating flow pattern could provide an increase in traffic in airports. There are research works related to this problem aiming at the characterisation of these vortices to reduce the associated hazard [e.g., Allen & Breitsamter, 2009; Deniau & Nybelen, 2009]. A first strategy is based on radar systems for the empirical knowledge to locate the vortex core in airport areas better [Gerz et al., 2005]. Multiple solutions have been suggested, but so far the winglets are widely extended nowadays. This device is mainly designed to reduce the local lift produced by the wingtip due to the decrease of the induced drag. The winglet will change the spatial structure of the vortex (see Figure 1.15) but not its strength. Furthermore, there are patents for active devices to break trailing vortices developed by Boeing and Airbus, but these patents are based on the perturbation of the flow with oscillating elements which are located on the wings, such as vortex generators or devices in flags [Greenblatt, 2005; Corjon, 2004; Crouch, 2000]. The second patent aims to destabilise the set of vortices using the Crow instability, [Crow, 1970]. These techniques are denominated *Passive Control*, using spanload modifications.

Conventional wingtip   Winglet
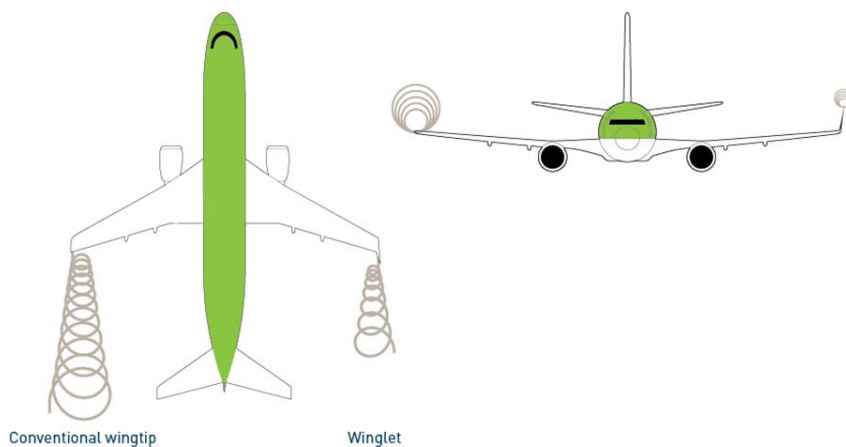
Figure 1.15: Wingtip diagram of Winglets.

Lee & Pereira [2013a,b] carried out passive control modifying a rectangular NACA0012 wing via a tip-mounted slender half-delta wing (*RHDW*) and reverse half-delta-wing (*RHDW*)(see Figures 1.16 and 1.17). The experiments showed that vortex breakdown occurred when the regular half-delta wing (HDW) was mounted, but not for the reverse half-delta wing (*RHDW*) configuration. The *HDW* vortex breakdown led to a rapidly diffused tip vortex, suggesting an enhanced wake-vortex decay. For the *HDW* wing configuration, the tip vortex remained concentrated but had a smaller size and also a weaker strength and rotation compared to the oscillating baseline wing. Also, the vortex centre of the oscillating *RHDW* wing-generated tip vortex was also found to be substantially displaced, especially in the transverse direction, which could translate into an increased blade-vortex-impingement distance and, as a result, an alleviated blade-vortex interaction. The addition of the *HDW* caused an increased total drag. Fortunately, the lift-induced drag was found to be reduced compared to its baseline counterpart for 0° and 5° *HDW* deflections. The change in the lift-induced drag also translates into a virtually unchanged profile drag, regardless of *HDW* deflec-

tion. In short, the largest lift-induced drag reduction achieved by the zero-deflection *HDW* resulted in an improved lift-to-drag ratio, at a high angle-of-attack range, compared to the baseline wing.
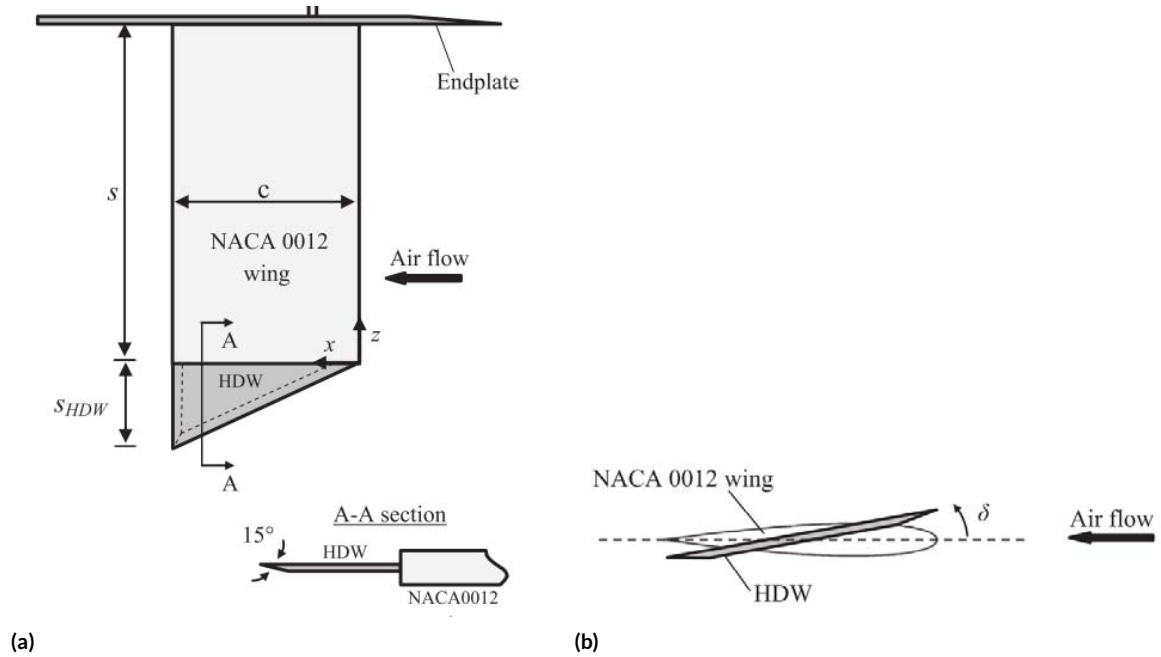
Figure 1.16: Schematics of experimental set-up and wing model. Top (a) and lateral view (b) [Lee & Pereira, 2013a].
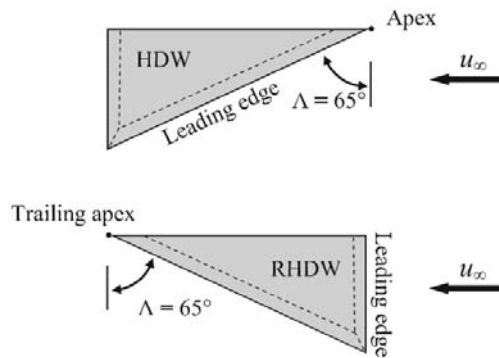
Figure 1.17: Wing delta tip [Lee & Pereira, 2013b].

The techniques that affect the vortex through forcing by an actuator are defined as *Active Control*. These methods take into account wingtip blowing, synthetics jet and morphed wings. Blowing was the first technique and the most studied by researchers, probably due to its easier implementation. The simplest approach was the use of spanwise blowing in an attempt to increase the effective span. In 1956, Ayers & Wilde [1956] was the first to describe the application of this blowing scheme to lift modulation and performed measurements on a swept wing and observed significant gains in the lift as well as a beneficial effect on the stall. Carafoli [1964] formulated a theory and conducted experiments with a straight wing and found that the main reason for lift gain is an effect of the wing enlargement caused by the jet (see Figure 1.18). Later, Carafoli & Camarasescu [1971] reported measurements on small-aspect-ratio wings, observing that lift augmentation is more intense for smaller aspect ratios, further suggesting that the primary mechanism for lift increment is an effective enlargement of the wing span. More experimental work on lateral blowing was carried out by White [1963] who noticed some beneficial effects on drag under certain conditions. Wu et al.

[1982] gave details of a tip blowing arrangement with several thin jets coming from slots whose length was a fraction of the wing chord. Although this procedure was not designed to extend the effective wing span, it exhibited some similarities to the winglet concept.
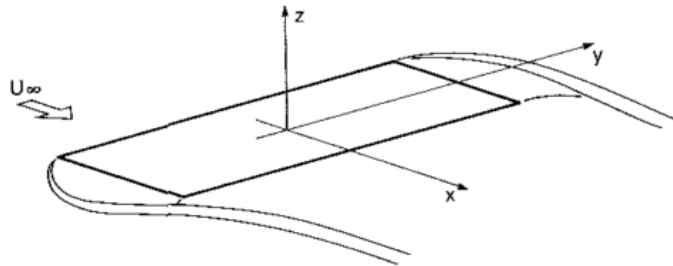
Figure 1.18: Lateral wingtip blowing concept [Tavella et al., 1986].

A study of the vortex structure of the flow field associated with the type of tip blowing considered in our study has been reported by Tavella et al. [1986] (see a sketch in Figure 1.18). These studies indicated that, for a tip jet whose chord is comparable to the wing chord, the wingtip vortex would usually engulf the vortices produced by the jet in cross-flow, with the result that in most cases only one vortex was found downstream of the wingtip. Conversely, in this tip blowing with discrete jets, the work of Wu et al. [1983] suggested that the complex vortex structure of a non-symmetric jet in cross-flow was preserved.
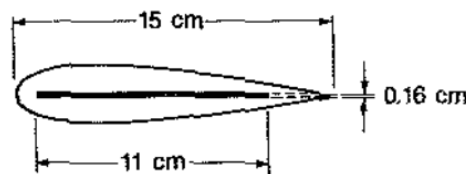
Figure 1.19: Blowing configuration [Tavella et al., 1988].

Later, Tavella et al. [1988] developed a theoretical study based on the same concept of lateral blowing and carried out experiments using a nominalised wing profile, NACA0018 with spanwise direction slot shown in Figure 1.19. As a result, it was found that the lift gain due to lateral blowing depends on the 2/3 power of the jet blowing intensity.

Lee et al. [1989] modified the wing profile using several tip jet configurations giving rise to multiple-vortex structures (e.g., Figure 1.20), in particular, secondary vortices (SV) in the near-field. An analysis of the near-field structure in such of the cases indicated that the presence of high SV provided the mechanism for the breakdown scaling laws.
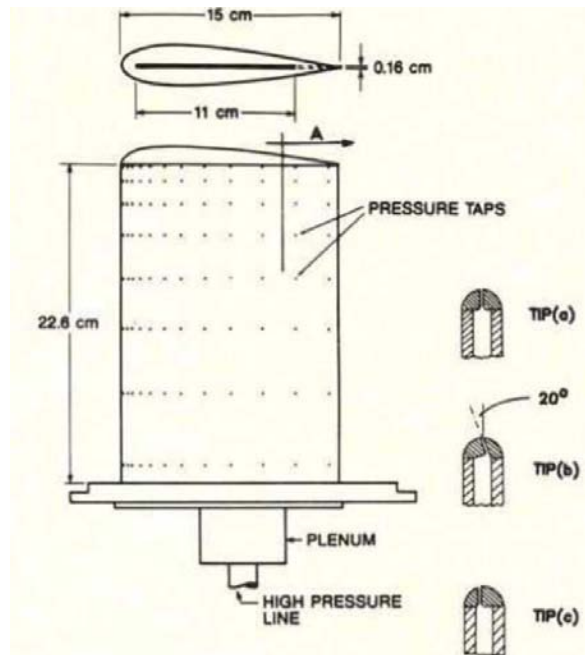
Figure 1.20: Blowing configuration [Lee et al., 1989].

More recently, Zhou et al. [2004] measured the near-field of tip vortices ($x/c \leq 5$) with spanwise blowing as a means to modifying vortex growth. They managed to reduce the rotational momentum of the tip vortex using a high-speed jet blowing at the core of the tip vortex, for example, the maximum streamwise vorticity was halved by a jet velocity of about $10 W_\infty$.
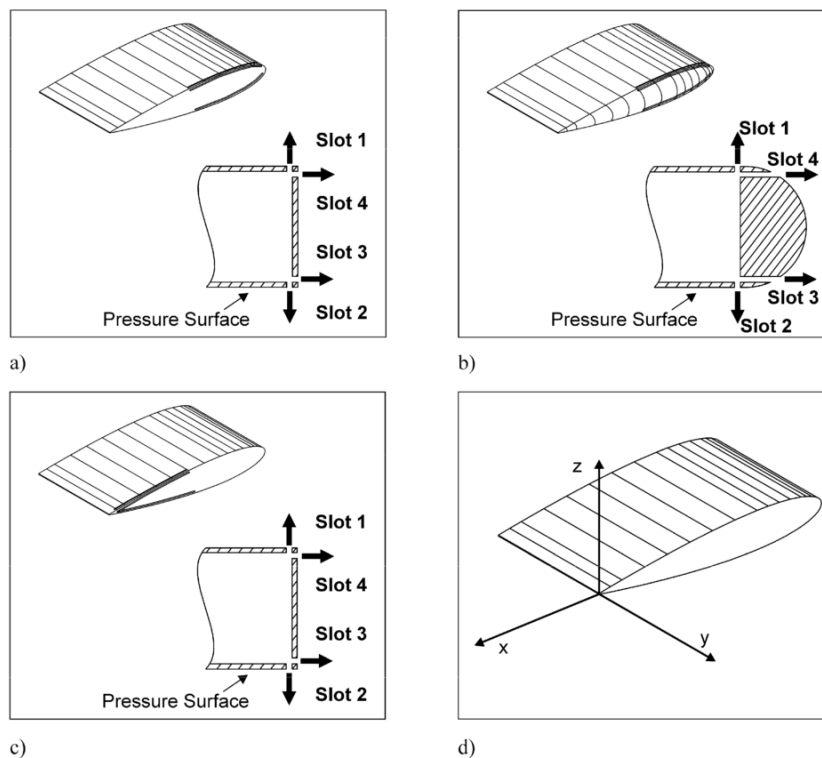
Figure 1.21: Blowing configuration tested. [Margaris & Gursul, 2009].

Margaris & Gursul [2009] analysed the effect of continuous jet blowing at the tip vortex on the growth

in the near-wake using the different wingtip-jet configurations shown in Figure 1.21. It was found that the high aspect ratio jet produces a pair of counter-rotating vortices of different strength; their interaction with the tip vortex leads to single or multiple-vortex wakes. The blowing from near the pressure surface resulted in diffused vortices in the near wake whereas blowing from near the suction surface producing the opposite effect. The tip shape was also varied; the round tip showed the ability to promote the Coanda effect, thus modifying the vortex interaction. The wing incidence was found to affect not only the tip vortex but also the jet-generated vortices.

A synthetic jet technique consists of a vibrating surface, the most common of which is a piezoelectric disc. This configuration is bound to a cavity with a small aperture. Synthetics jets are produced by periodic compressions and expansions in a diaphragm. The fluid inside the cavity vibrates, resulting in an oscillation of the fluid at the orifice and it introduces momentum into the flow-field with zero-net-mass-flux as depicted in Figure 1.22. During the blowing portion of the cycle, a pair of vortices is generated at the orifice edges due to the air being pushed through the hole. This vortex pair advects downstream with its induced velocity. During the suction portion of the cycle, the surrounding air near the orifice is pulled into the cavity, whereas the vortex pair has moved far enough downstream from the orifice not to be affected by the fluid drawn into the cavity. This rapid formation of vortex pairs advecting downstream yields a time-averaged outward velocity along the axis of the orifice.
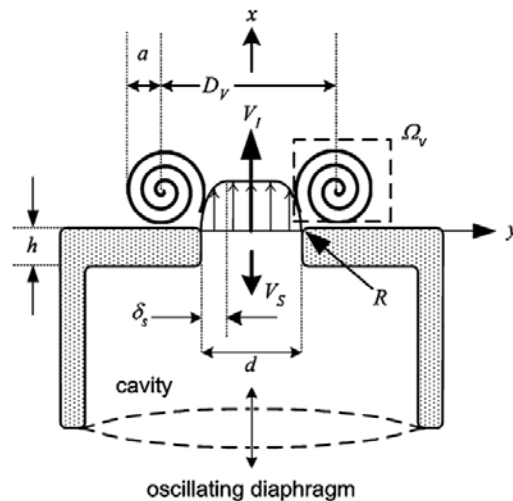
Figure 1.22: Schematic of a synthetic jet [Holman et al., 2005].

Holman et al. [2005] studied the formation criteria for a synthetic jet and found that to create it, the driving frequency of the jet and its stroke length must fulfill certain criteria:

- the reciprocal of the Strouhal number must be lower than 1 for a two-dimensional jet and,

- less than 0.16 for an axisymmetric jet.

Synthetic jets need no fluidic plumbing and require a minimal power ($O(10W)$), which is a huge advantage. Amitay & Cannelle [2006] observed the effect of the slot aspect ratio on the development of the synthetic jet, and the spatial evolution of secondary three-dimensional vortical structures in the flow field. The measurements in the plane along the slot revealed a unique flow pattern, where near the orifice the flow is two-dimensional, while further downstream the vortex pair lines develop secondary counter-rotating structures. The streamwise and spanwise spacing between these structures vary with the stroke length and

formation frequency. As the orifice aspect ratio increases the effect of the slot edges decreases, thus the secondary structures are less pronounced. van Buren et al. [2014] observed the formation and evolution of flow structures of a high-speed, finite-span synthetic jet issued into a quiescent flow. It was found that the velocity and vorticity fields were significantly affected by the Reynolds number. Lowest Reynolds number produced the highest normalised peak velocities and vorticity. As the Reynolds number increases, it is observed axis switching and its streamwise location increases. They utilised the Q-criterion[†] for the identification of vortices in the flow field and the reconstruction of the 3D vortex ring that was formed near the orifice, and to track its evolution and advection. The effect of the Reynolds number has a pronounced influence on the development of the flow structures and, as a result, may alter the effectiveness of flow control. Therefore, this method is being used for separation control in wing airfoil.

Firstly Amitay et al. [2001] investigated the control of separation on an unconventional symmetric airfoil using synthetic jet actuators. The symmetric airfoil is a NACA and a leading edge section that is one-half of a round cylinder. When synthetic jet control was applied near the leading edge, they observed the effect of the actuation frequency, actuator location, and momentum coefficient for different angles of attack. Margaris [2006] carried out an experimental investigation to study the effect of synthetic jet blowing near the wingtip vortex, as a means of diffusing the trailing vortex. A schedule of the experimental setup is presented in Figure 1.22. The effect of the synthetic jet was compared to that of a continuous jet blowing from the same configurations. The results showed that the use of synthetic jet blowing was beneficial to diffuse the trailing vortex and comparable to the utilisation of the continuous jet. The influence was significant for the highest blowing coefficient. The driving frequency of the jet did not prove to be an important parameter.
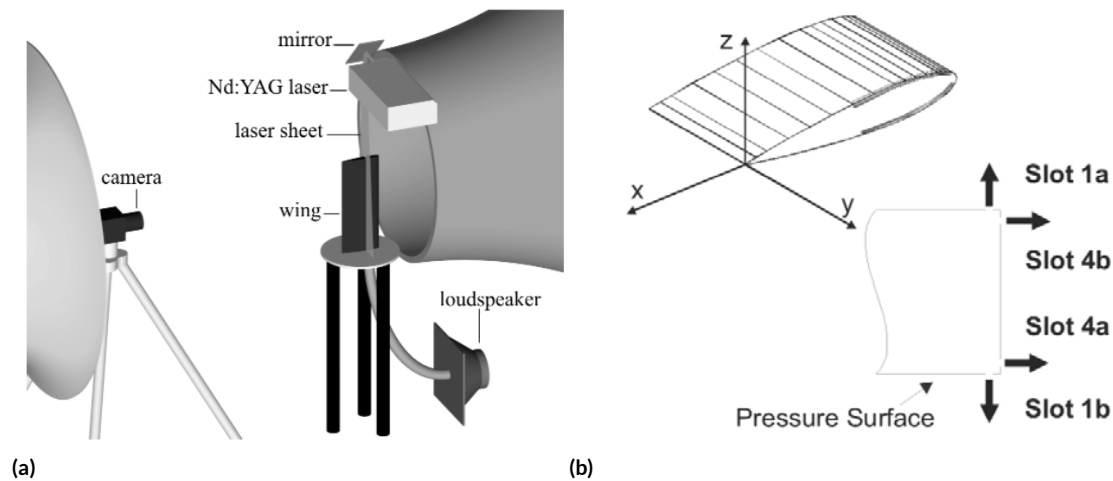
Figure 1.23: Margaris [2006] experimental set-up and blowing configuration.

Dghim et al. [2016] investigated the effectiveness of synthetic jet actuation in controlling a wingtip vortex. They used another slot configuration on the tip, shown in Figure 1.24, and concluded that forcing the wingtip vortex at a frequency in the range of frequencies of the long and short-wave instabilities resulted in decreased pressure coefficients as compared to natural vortex measurements. Furthermore, they considered two control configurations, namely, a "least effective" configuration with synthetic jet momentum coefficient C_μ =0.004 and non-dimensionalised actuation frequency F^+ =0.71 and a "most effective" configuration with C_μ =0.04 and F^+ =0.213. Measurements at x/c=1 showed that, under the latter case, the

---

[†]Q-criterion is a technique to identify the presence (or absence) of vortices in regions of vorticity concentrations by identify regions in the flow field where rotation dominates the strain.

vortex was stretched into an ellipsoid shape with a 50% average decrease in the peak tangential velocity, and 30% broadening of the effective vortex core radius. Further downstream, the vortex seemed to regain its universal shape but with reduced strength. These results suggested that the lower frequency control configuration allowed the synthetic jet to travel larger distances into the vortex, bringing turbulent structures within its core, and thus resulting in a significant increase of mixing, and the subsequent decrease of vortex strength.
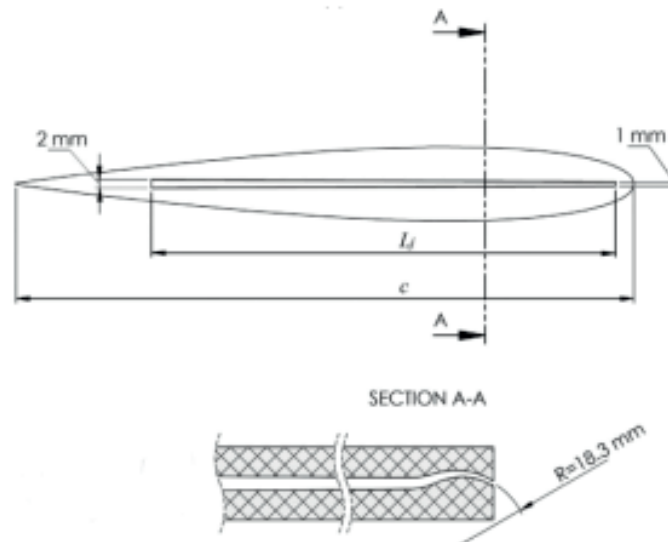
Figure 1.24: Slot geometry [Dghim et al., 2016].

Sahni et al. [2011] performed a numerical and experimental study to analyse the three-dimensional flow structures and interactions of a finite-span synthetic jet in a cross-flow at a chord-based Reynolds number of 100×10^3 and $0°$ angle of attack. They considered six blowing ratios in the range of 0.2 to 1.2 (see Figure1.25). For the high blowing ratio range, turbulent vortical structures were dominant, leading to larger spanwise structures, with greater spanwise wavelength. Moreover, the phase-locked flow fields exhibited a train of counter-rotating coherent vortices that lifted off the surface as they advected downstream. In the mid-blowing ratio range, combined features of the low range (near the slot) and high range (in downstream locations) were found, where a pair of counter-rotating vortices issued in the same jet cycle collided with each other. In all cases, the spanwise extent of the secondary coherent structures reduced with downstream distance with a larger decrease at higher blowing ratios.
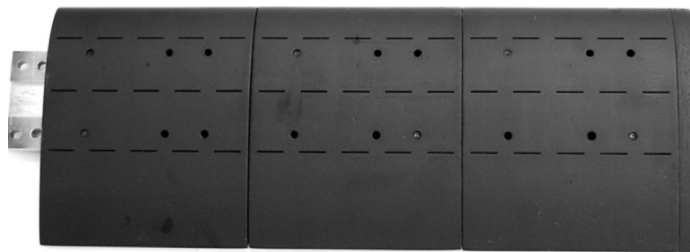
Figure 1.25: Wing model, NACA4421 used by Sahni et al. [2011].

Employing the same wing airfoil but another synthetic jet blowing, shown in Figure 1.26, Elimelech et al. [2011] concluded that the flow field is governed by the superposition of spanwise structures. These are gen-

erated along the orifices span due to the synthetic jet's vortex pairs, and also streamwise structures that are associated with the finite span of the jet (edge vortices). These flow structures are formed almost immediately downstream of the synthetic jet hole and evolve into a well-organised three-dimensional flow field further downstream.
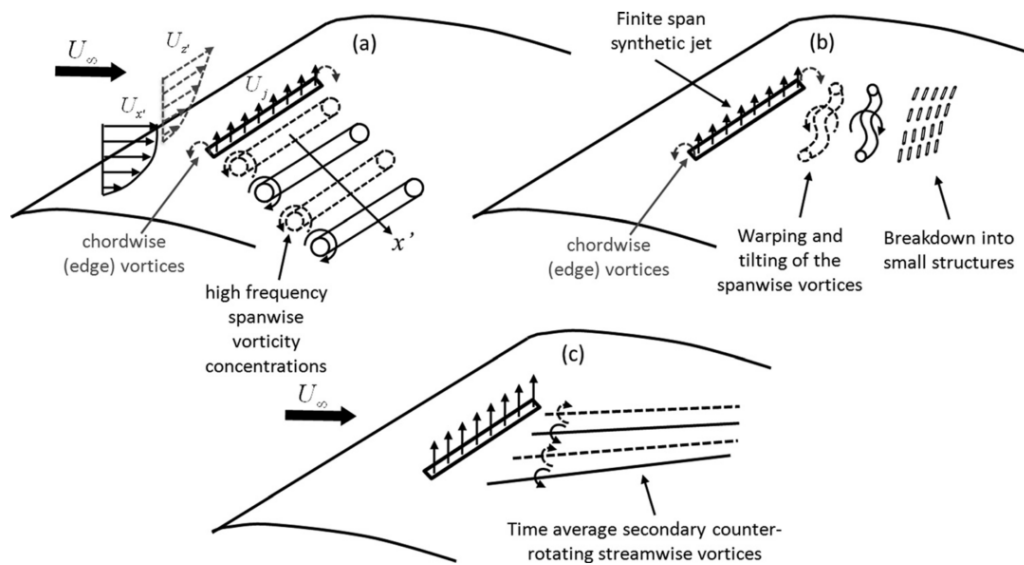
Figure 1.26: Schematics of vorticity generation due to the interaction of the finite span synthetic jet and the cross-flow; the baseline flow and a description of the flow structures that are part of the interaction (a), description of the phase-averaged flow structures (b) , and the structure of the time-averaged flow field (c) [Elimelech et al., 2011].

Quite recently, Şugar Gabor et al. [2016] carried out numerical simulation and experimental wind tunnel. A sketch is shown in Figure 1.27. They tested a morphing wing (a) equipped with a flexible upper surface and controllable actuated aileron (b). The model was fitted with a composite material upper skin whose shape can be morphed, as a function of the flight condition, by four electrical actuators placed inside the wing structure. This technology of morphing modifies the aircraft lifting surface that can be activated and deformed according to the flight conditions, thus allowing a multi-point design of the aircraft and improving aerodynamic performance. A morphing wing could enable the aircraft to fly at optimal lift-to-drag ratios for any condition encountered during flight by changing some of the wing's characteristics. The optimisations are developed with the aim of controlling the extent of the laminar flow region.
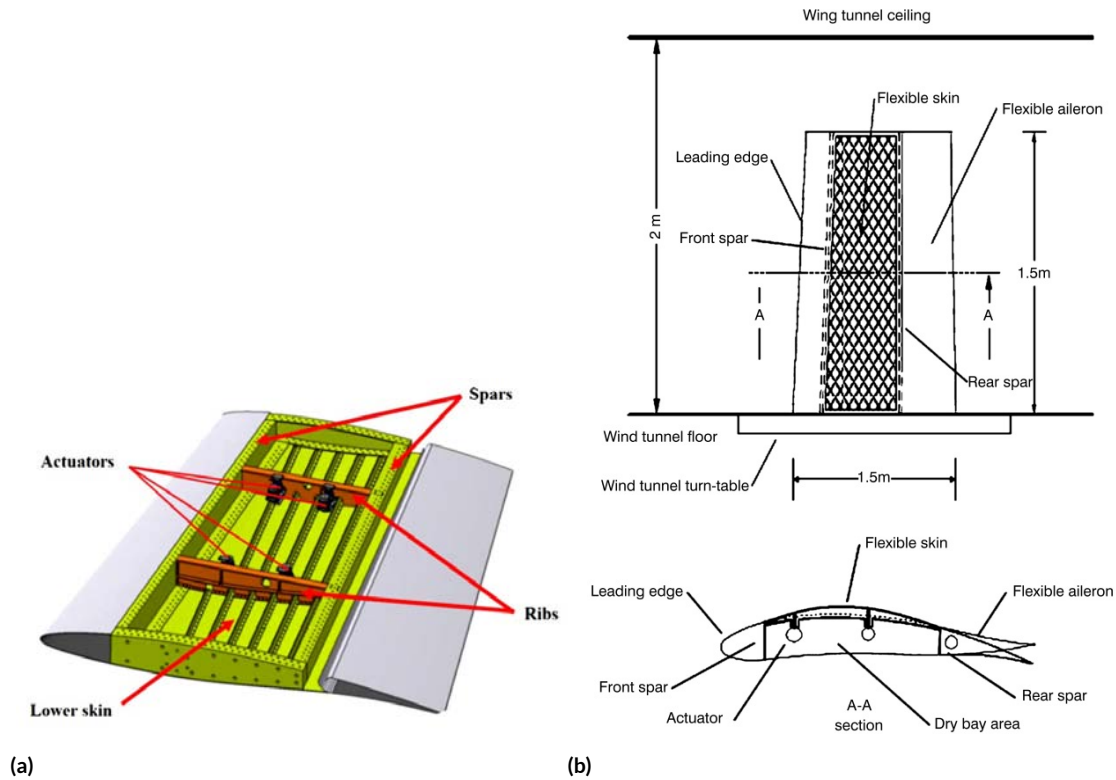
Figure 1.27: CRIAQ MDO 505 morphing wing concept and the structural elements of the CRIAQ MDO 505 morphing wing concept (the morphing skin is not shown in the Figure)[?ugar Gabor et al., 2016]

1.8 Objectives

This work aims to propose a new application in the context of the experimental characterization of wingtip vortices in the near-field. To that end, one would obtain a quantitative description of the velocity field in the roll-up process by means of a smoke-wire system together with a set of ordinary differential equations. The origin of the idea behind this experimental study was formulated by Meunier & Villermaux [2003].

On the other hand, also we explore the influence of the Reynolds number on the theoretical parameters in the range of ultra-low or low values both experimental and numerically since this dependence has not been considered elsewhere. The theoretical parameters considered are of Batchelor's model $(S, \overline{z}_{OB})$ and Moore & Saffman's model $(b, n, \overline{z}_{OMS})$ as function of Re_c. For that, the department's PIV knowledge will be used to create an accurate database of transverse velocity results in the wing wake vortex, at long distances from the wing.

Finally, we will apply two active Control method based on wingtip continuous jets for several aspect ratios, defined as velocity injection $R_{jet} = \frac{W_{jet}}{W_\infty}$. Our objective is to establish how the active Control in the radial direction interacts whit the wing-tip vortex. So we explore the strong or weak influence or the blowing jet on the vortex strength.

2

Experimental setup

2.1 Wing model

The scaled wing model used to generate wing tip vortices was a rectangular wing profile with a rounded (half-circular) tip. It has a NACA0012 airfoil section which is symmetrical (0% of the maximum chamber) with a maximum thickness of 12% of the chord. The main dimensions are a semispan of 200mm and a chord of 100 mm (see Figure 2.1).
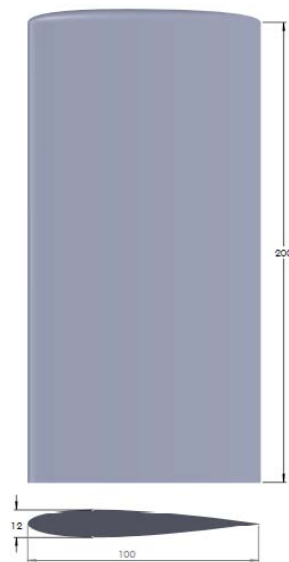
Figure 2.1: 3D view of the wing model NACA0012.

It was manufactured in aluminum, and painted with a special pigment to avoid or minimize water corrosion. We have selected this particular wing model because it is the commonest one used in previous experimental works on the wing tip vortex [del Pino et al., 2011b,a]. Of course, the particular rounded tip geometry has an influence on the flow, especially on the roll-up process close to the wing tip. However, we have not checked this point because we have only used this geometry. We believe that the influence of the rounded tip geometry becomes negligible sufficiently far from the wing tip. The model was assembled to

select different angles of attack, between the free-stream and the wing model. Details of the mounting will be shown in the sections below.

2.2   Camera

One high-speed camera PHOTRON model FASTCAM SA-3 was used, which records 1024×1024 pixel resolution at frames rate up to 1000 fps and 384×288 pixel up to 60000fps. This camera has an internal storage of 4GB and it is connected to the laptop by an Ethernet cable.

In Chapter 3 facility, we used a Nikon 105 mm lens (model AF Micro Nikkor 105mm) and f/2.8. and the Chapters' 4-5 facilities used a TAMROM SP 70-200 lens (model A009 DI VC USD), and f/2.8. (see Figure 2.2).

Figure 2.2: High Speed camera with TAMROM SP 70-200 lens.

2.3   Facility

We will describe the experimental arrangement in each chapter and also the techniques applied. Nevertheless, we introduce the two large facilities and their main characteristics in this chapter: the wind tunnel and the towing tank.

2.3.1   Wind tunnel

All experimental data results of Chapter 3 were conducted in a subsonic wind tunnel located in the Vehicles Aero-Hydrodynamics Laboratory at Málaga University. The wind tunnel has 1x1m^2 square test section that extends 4m. Several sides of the test section were built in glass to allow us to observe the wing model plus associated equipment. This configuration also guarantees visually how the experiment has been running under certain conditions. Figure 2.3 shows the different parts of the Aero-Hydrodynamics Laboratory wind tunnel.
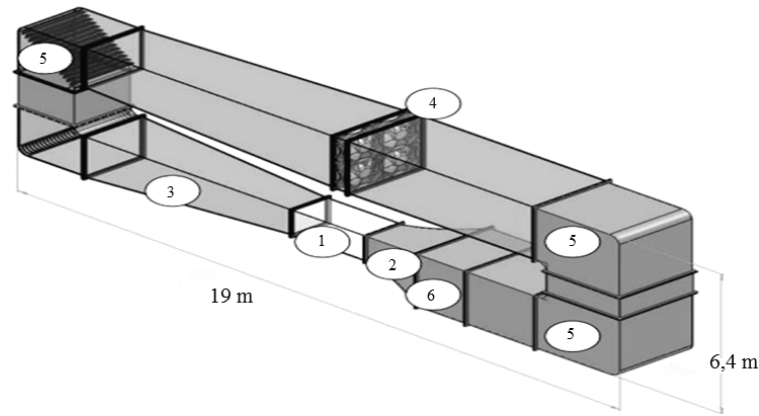
Figure 2.3: 3D Schematic of Wind tunnel: Test section(1), contraction section (2), diffuser (3), fan (4), turning vanes (5), settling chamber (6).

The wind tunnel test section can achieve a range of speed between 2 and 30m/s, and the airflow is supplied by four fans driven by 3-phase AC motor of 15kW each. The fan speed is controlled by using variable frequency excitation in open-loop. National Instruments' LabView software was used to monitor, in real time, atmospheric parameters and to control the airflow velocity inside the test section. The variables that were controlled instantaneously included the airflow velocity and the temperature inside the test section. The velocity was measured by using a hot wire anemometer while the temperature was recorded with a probe PT100. Therefore, we can compute the chord based Reynolds number with the expression $Re_c = \frac{W_\infty c}{\nu}$, where ν is the temperature dependent kinematic viscosity and W_∞ is the free-stream velocity and c is the chord.

Figure 2.4: Wind tunnel's inlet mesh.

To measure a time averaged velocity measurements and to perform flow visualisations the airflow entering the inlet test section must be uniform. To that end, the airflow was accelerated through the conditioning chamber which has two devices: honeycomb and stainless steel net. Firstly, a grid was located at the entrance of the inlet conditioning chamber to reduce the overall turbulence level. This grid consists of 50mm thick plastic honeycomb. Each circular cell of the honeycomb had a nominal size of 8mm diameter. Secondly, a stainless steel grid of 1mm cross section was installed, thus obtaining a maximum turbulence intensity is lower than 3% [Fedoul et al., 2014]. The blockage area is lower than 0.35% using a NACA0012 airfoil of 100 mm chord and 200 spanwise length, which confirms the absence of tunnel blockage effects. Two pictures of the conditioning chamber are shown in Figure 2.4.

(a)

(b)   (c)
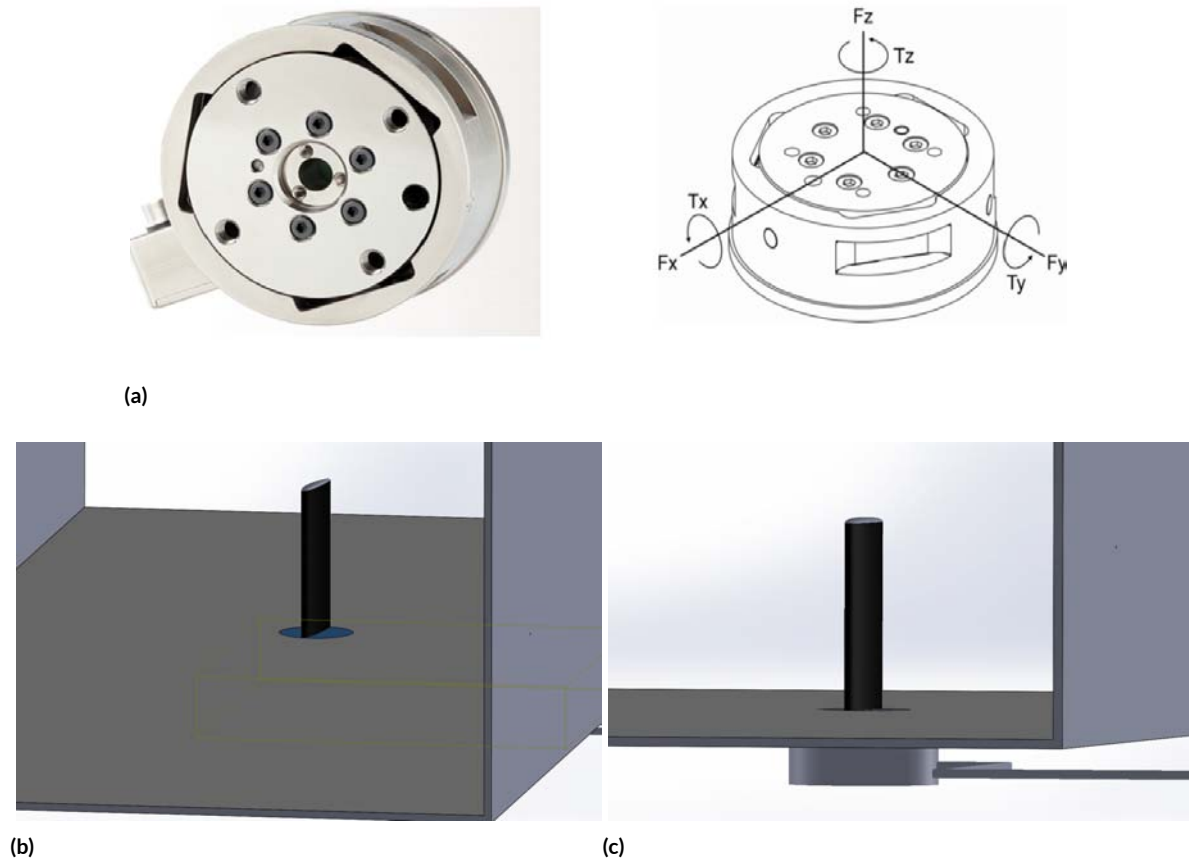
Figure 2.5: Digital six components force/torque sensor (a) and detailed of wing model mounting (b,c).

The laser sheet (less than 1 mm thick in the measurement section) was obtained using a 2 W green laser source (532 nm, CVI Melles Griot 85-GHS-301) in conjunction with a set of lenses (cylindrical lens of -6.25 mm focal length). The distance d from the wing trailing edge and the laser sheet can be modified. A tilted mirror was located far downstream at 15 chords from the wing so that the digital camera can record the control plane from the top of the test chamber.

The section chamber has at its base a rotating bracket along with a precision digital force/torque sensor which holds the wing model (see Figure 2.5). A servomotor rotates around its vertical axis to set the angle of attack, α. The limitations of the force/torque sensor are:

Limit values			
	X	Y	Z
Force	$32N$	$32N$	$100N$
Torque	$2.5Nm$	$2.5Nm$	$2.5Nm$

Table 2.1: Limit values of the force sensor.

2.3.2 TOWING TANK

The experimental test that are described in Chapters' 4 and 5 were conducted in a towing tank located in the same laboratory (see a 3D layout in Figure 2.6). The main reason for the use of a towing tank is the absence
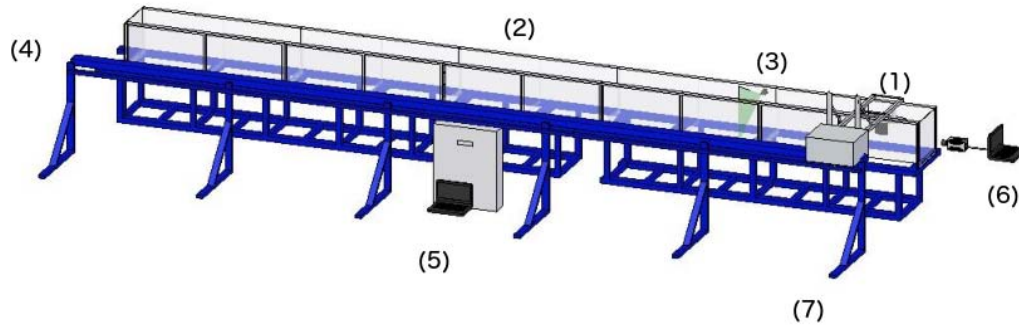
Figure 2.6: 3D Schematic of towing tank: wing model NACA0012 in a support moving from right to left (1), perspex channel (2), laser sheet (3), guide rail (4), velocity control of guide rail (5), high-speed camera (6), and blue iron structure (7).

of elements that move the fluid and turbulence levels achieved are extremely small (less than 1%). The wing model (1) is a NACA0012 airfoil as commented below. The towing tank is 10 m long, and 0.5×0.5 m^2 cross-section, in perspex which had a thickness of 25mm (2) in order to allow for optical visualizations, as well as for 2D-PIV measurements of the velocity field. The water in the tank is at rest and the wind model moves through it. The wing model is vertically assembled on a guide rail (4) that moves (from right to left in the schematic) through the whole towing tank. This guide was designed to achieve versatility for several experimental conditions (no control or active control). Besides, not only the wing model, but also different types of equipment could be moved such as the camera, lasers or pumps to carry out several tests. The towing tank used two rails which were made of iron. They were mounted with 90 degrees to bear the weight of the water and to guarantee the correct alignment within $\pm$ 0.1 °. All the iron structure (7) is aligned using a digital inclinometer within $\pm$0.1°. We imposed a constant velocity to the wing model. To that end, an electric motor has been installed which provides a velocity between 1 and 1000 mm/s with an error lower than 0.5%. The electric motor is controlled by a laptop with feedback by means of an encoder (5) and the control of the acceleration from rest and the final position of the model was set using Matlab® through the *USB* port. A high-speed camera (6). The wing's support (1) is vertically mounted on the upper surface of the first sector of the channel working section, in such a way that the wing tip was approximately at the centre of the test section and allows different attack angles between the upstream flow and the wing model (details of the mounting are shown in Figure 2.7). This experimental set-up allowed us to obtain measures up to 50 chords downstream the wing. The laser sheet was located 2.5 m from one end of the structure to allow the wing movement to start.

In addition, the water temperature was measured by equipment that consists of nine sensors in three groups along the towing tank. Each group had three sensors at different heights in the tank, so the average temperature was measured along the tunnel. The sampling rate is a measurement per second in each sensor obtaining an accuracy of $\pm$ 0.1 °C.

(a)

(b)   (c)
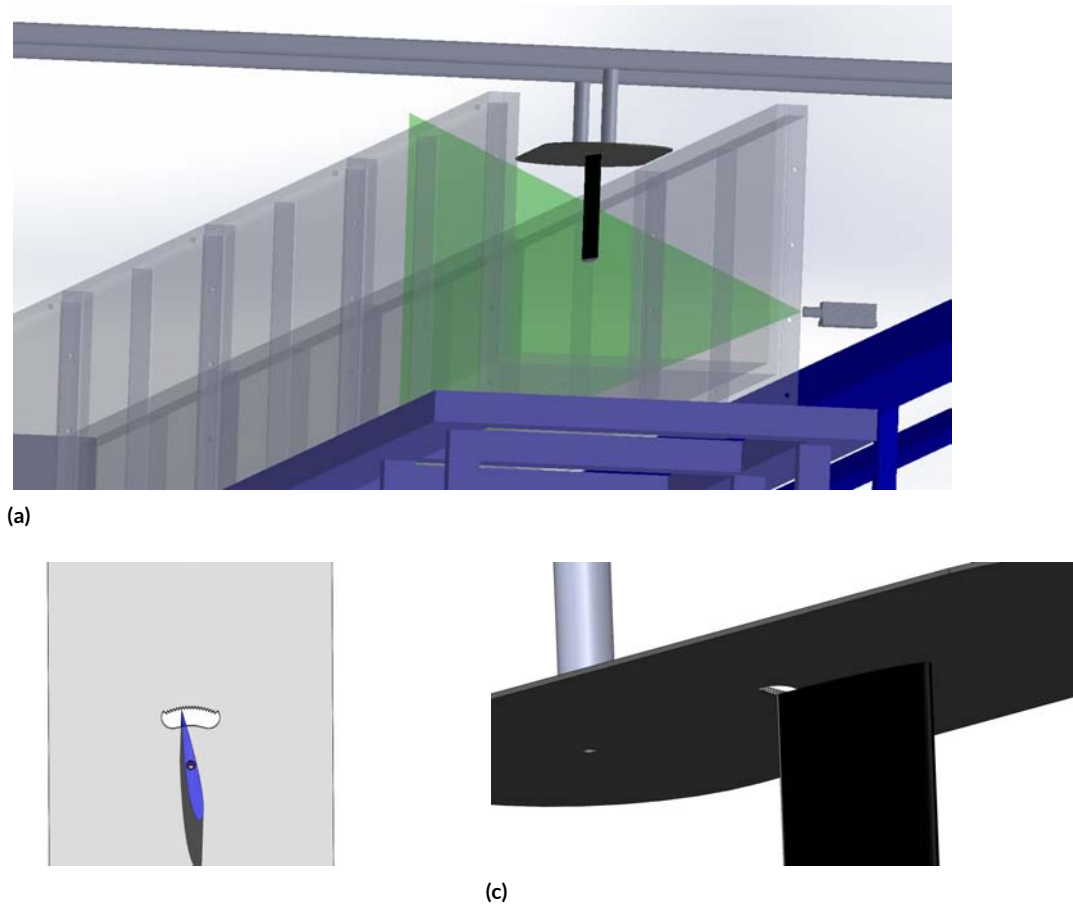
Figure 2.7: 3D general wing model mounting view (a) and detailed of wing model mounting (b,c).

2.4 PIV MEASUREMENTS

As it is well known, the PIV technique consists of the accurate, quantitative measurement of fluid velocity vectors at a considerable number of points by tracking, registering, and processing the successive positions of particles inoculated into the flow. 2D-PIV is used to obtain the two-component velocity field in the planar region illuminated by a laser light sheet at the experiments indicated in Chapters' 4 and 5. The analysis of the recorded image is one of the most important steps of the entire procedure, as it couples with the acquisition process to determine the accuracy, reliability, and spatial resolution of the measurement; usually, it is also the most time-consuming part of the process. This technique allows for capturing velocity information of whole flow fields in fractions of a second using two consecutive images. To obtain these images, we seeded the tank with glass silver coated spheres of 10 μm (HGS-10 from Dantec). These particles are neutrally buoyant in water, thus minimising their relative motion to the water flow due to gravity and centrifugal forces. The illuminated plane of the flow is located perpendicularly to the wing model movement, represented in Figure 2.8 and the images were recorded by a high-speed camera located downstream to model movement.

In order to illuminate the particles we used a laser sheet (less than 1mm thick in the measurement section) which is obtained by means of three 0.5 W green laser sources (532 nm-model SDL-532-500T) in conjunction with a set of lenses (cylindrical lens of -6.25mm focal length) and a mirror was installed in front of the laser plane to obtain a better illumination sheet (see Figure 2.9).

The PIV algorithm employed was DPIVSoft which performs a double pass PIV method. DPIVsoft is based on the cross-correlation PIV algorithm. The software takes a small interrogation box around each

(a)   **(b)**
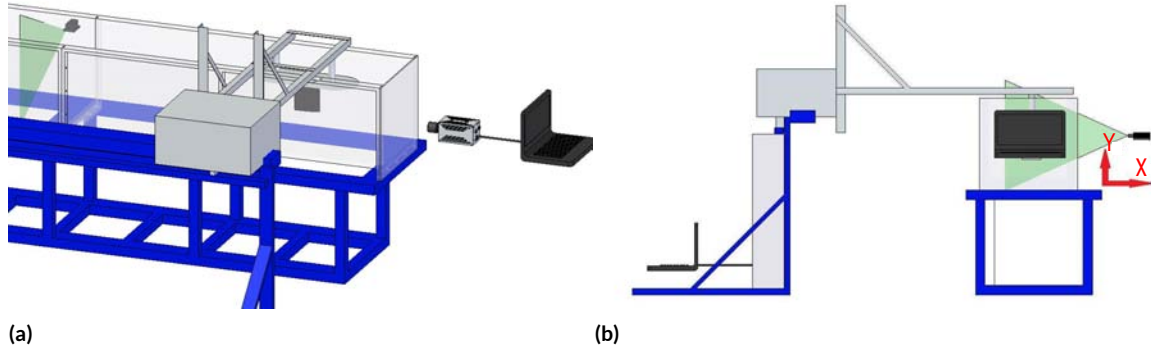
Figure 2.8: Towing tank details: 3D view of the guide rail, the wing model, digital fast camera and laser (a); 2D view with the computer that controls the guide rail on left hand side (b).

velocity vector and calculates on this window the intercorrelation function between the two images, whose maximum peak gives the average displacement of the particles on the interrogation window. The cross-correlation functions are calculated through Fast Fourier Transform (FFT), to accelerate the process. The in-plane loss of pairs error is decreased by translating the interrogation windows in a second run. DPIVsoft is optimised for the velocity fields containing high-velocity gradients using a deformation of the interrogation windows based on the velocity gradients. It reduces the margin of error by a factor of 10 for moderate velocity gradients. Because the interrogation windows are deformed according to the velocity gradients, the algorithm achieves a first run in which a rough estimate of the velocity field is calculated (see Figure 2.10). The velocity gradients are then computed by finite differences and smoothed to obtain a good estimate of the deformation that will be achieved in the second run. The second run is more accurate and has a better spatial resolution than the first run. This method using two runs is very efficient. A comprehensive review of the algorithm and its accuracy can be found in Meunier & Leweke [2003].

2.4.1   First run parameters

The first run is aimed at calculating a rough estimate of the velocities and the velocity gradients. As seen in Figure 2.10, the number of boxes corresponds to the number of velocity vectors to be calculated in each direction. This number of vectors depends on the size of the image and the size B of the correlation box. For the first run, there is no overlap between the interrogation windows. The number of boxes should thus be roughly the size of the image divided by the correlation box size. The value is 30 vectors in each direction. The correlation box size (in pixels) B for the first run is a power of 2 because of we use FFT (Fast Fourier Transform). The choice of this parameter is very subtle and directly influences the quality of the results. First, the interrogation window should be big enough so that there are enough particles in each sub-window. The minimum number of particles is:

$$N_{part} > 4, \tag{2.1}$$

but the results will be better if 10 to 20 particles are visible in the interrogation window. This criterion depends on the density of particles and is fulfilled for correlation box sizes of 32 or bigger. Another rule for the correlation box size is induced by the in-plane loss of pairs. To have less than a third of the particles leaving the interrogation window on the second image, the maximum displacement should be lower than

(a)   (b)

(c)
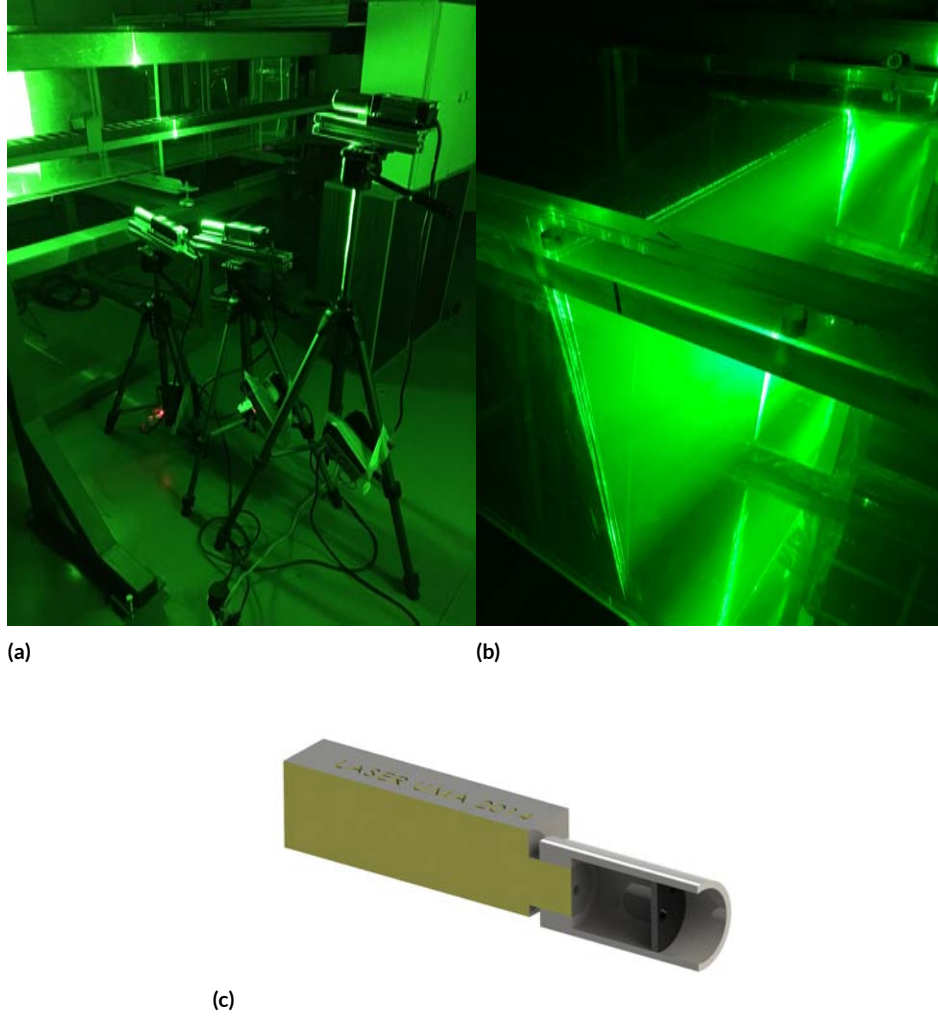
Figure 2.9: Picture of three align laser sheets (a), the resulting illuminated plane inside the towing tank (b) and laser lens assembly section (c).

$$\| u \|_{max} < B/3. \tag{2.2}$$

A final criterion of the first run is linked to the velocity gradients. Indeed the correlation is not efficient if the movements of the particles are not homogeneous inside the interrogation window. In fact, the difference between the displacement of a particle at the top of the window and a particle at the bottom of the window must be smaller than the size of the particles d (see Meunier & Leweke [2003]). This leads to the following criterion:

$$| \frac{du}{dr} |_{max} B < d. \tag{2.3}$$

The size of the particles is usually of the order of 2 pixels, and the displacement gradient was estimated after a first calculation. If the two criteria (2.2) and (2.3) cannot be fulfilled at the same time, it means the velocity gradients in the experiment are very high, and the user should play with the advanced parameters.

The default value for the correlation box size is 32 pixels. The maximum of the correlation function is sought in a window of size $W_x \times W_y$, which it is smaller than the correlation box size. This prevents the detection of peaks with a large displacement. The only criterion for this parameter is:

$$W_x > 2 \mid u \mid_{max}; W_y > 2 \mid v \mid_{max} \qquad (2.4)$$

The value is the largest advised value for a box of 32 pixels, i.e. 28 pixels. Indeed, the algorithm cannot calculate the sub-pixel displacement if the peak is on the edge of the correlation window.
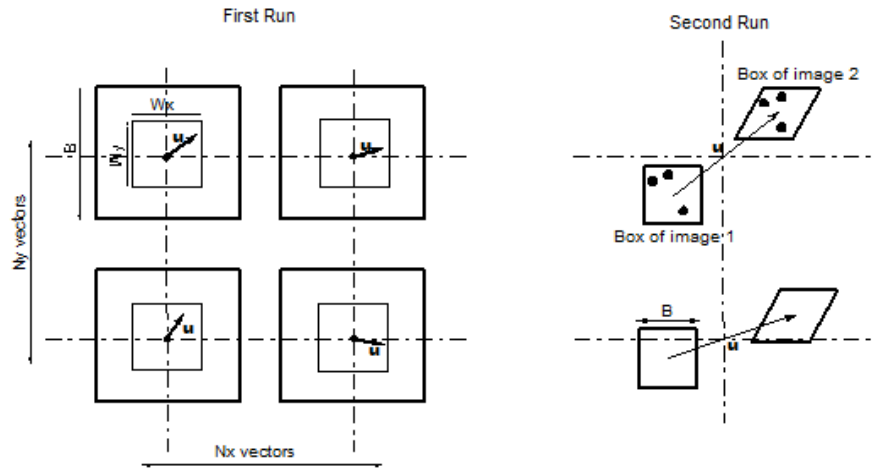
Figure 2.10: Scheme of the translation and deformation of interrogation boxes in both runs [Patrice et al., 2004].

2.4.2 Second run parameters

For the second run, the same parameters have to be defined: number of vectors, correlation box size and search window. However, their role is slightly different because of the translation and deformation of the interrogation boxes. The criteria are not as restrictive as in the first run. The number of boxes should be bigger in each direction so that the velocity field has a high spatial resolution. We use a 50% overlap between two adjacent windows. If there is more overlap, the two neighbouring vectors are also correlated. If there is less overlap, the spatial resolution is lower. In our case, the images have dimensions 1024×1024 pixel, and we calculate 60 vectors in each direction for a correlation box size of 32 pixels.

The size B (see Figure 2.10) of the boxes is easier to choose in the second run. Indeed, criteria (2.2) and (2.3) are not necessary since the boxes are translated and deformed. The box should be big enough so that there are enough particles, as stated by criterion (2.1). The size of the search window does not need to be very large. Indeed, after translation of the boxes, the peak is very close to the centre of the correlation function. It can thus be tiny, but this parameter has a feeble influence on the result. In conclusion, the parameters in the second run only have to respect the criterion shown in Equation (2.1). The values are 60 vectors per direction, a correlation box size of 32 pixels and a search window of 20×20 pixels.

After each run, the velocity field is filtered with a median filter to remove the false vectors. The median filter is adjusted by a parameter α defined as follows. For each vector v, the software calculates the median

vector v_{med} of its 8 neighbours and replaces it by the median vector if:

$$\| v - v_{med} \| > \alpha \cdot \| v_{med} \|, \tag{2.5}$$

the value used for α is 0.5, but it can be increased up to 1 for very noisy velocity fields.

2.4.3 NUMBER OF ITERATIONS IN THE FIRST RUN

When the velocity gradients are very high, the first run is very noisy and the determination of the velocity gradients for the second run is thus scattered. It can be useful to apply a second iteration (or more) in the first run, with deformation and translation of the boxes, for the velocity gradients to be better converged. We carried out 2 iterations at the first run.

2.5 CALIBRATION

Finally, the calibration of a 2D-PIV imaging set-up relies on images of a planar calibration target which was placed alongside the light sheet plane. This calibration target consisted of an equally spaced grid of dot markers (10 mm) that were easily detected with simple image processing techniques (see Figure 2.11) . A single image of planar calibration marks was enough to calculate adequate mappings between image space and object space. In this case, we only required the relationship between pixel & mm.

(a)   (b)
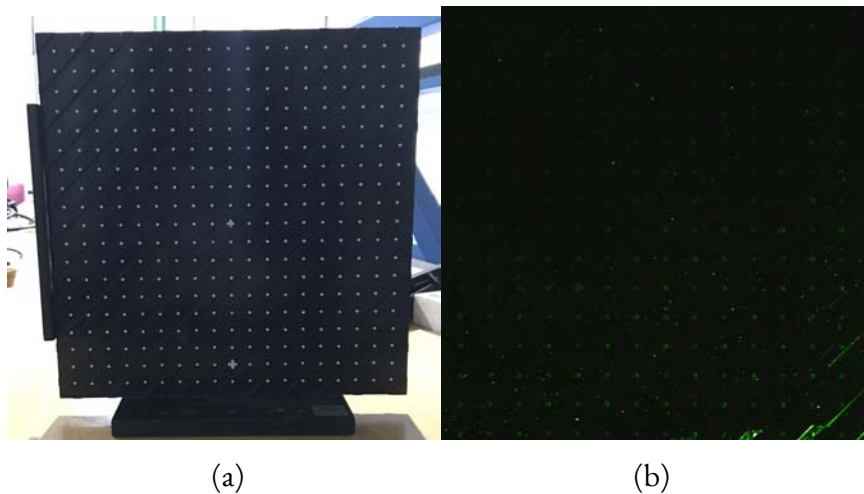
Figure 2.11: Target TSI (a) and calibration image inside the towing tank(b).

3

Experimental characterization of wing-tip vortices in the near field using smoke flow visualizations

According to the application of the current work, one of the first references dealing with the experimental characterisation of wingtip vortices was carried out by Baker et al. [1974]. Laser Doppler Anemometry (LDA) development made it possible to obtain measurements in a free-surface water tunnel. Two components of velocity in the vortex wake were acquired, up to sixty chord lengths in the axial direction, while Phillips & Graham [1984] used the hot wire technique at stations from 45 to 109 chord lengths downstream of the wing. Additionally, the NACA0012 airfoil is a common model used in experiments at lab scale. The same wing model was used by Sarpkaya & Daly [1987] to study the effects of ambient turbulence on the lifespan of wingtip vortices. Besides, Iungo et al. [2009]; del Pino et al. [2011a] used it to analyse the meandering effects. Lee & Su [2012] have also experimentally investigated vortex control devices using this airfoil as well. More recently, Particle Image Velocimetry (PIV) has been used in Heyes & Smith [2005], who tested the influence of the wingtip geometry in the vortex roll-up process. Further research has been accomplished by means of Stereo-PIV, whereby the three velocity field components are measured. That is the case of Roy et al. [2011], Bhagwat et al. [2015] or del Pino et al. [2011a] whose experimental results were compared with Batchelor's and Moore & Saffman's models, including the axial velocity evolution. Current researchers, e.g. Lee [2011], Sohn & Chang [2012], Gim & Lee [2013] and Manar et al. [2014], show that PIV is a useful and widespread technique. However, PIV requires complex facilities which are quite expensive. On the contrary, some traditional flow visualisation techniques like the smoke-wire technique do not need such an elaborate system to gather qualitative information on airflow patterns.

The origin of the idea behind this experimental study was formulated by Meunier & Leweke [2003]. In this manuscript, the authors describe how the advection of a passive scalar blob in the deformation field of an axisymmetric vortex is a simple mixing protocol through which the advection-diffusion problem is amenable to a near-exact description. The blob rolls up in a spiral which ultimately fades away in the diluting medium. Therefore, this work aims to propose a new application in the context of the experimental characterisation of wingtip vortices in the near-field. To that end, one would obtain a quantitative description of the velocity field in the roll-up process by means of a smoke-wire system together with a set of ordinary differential
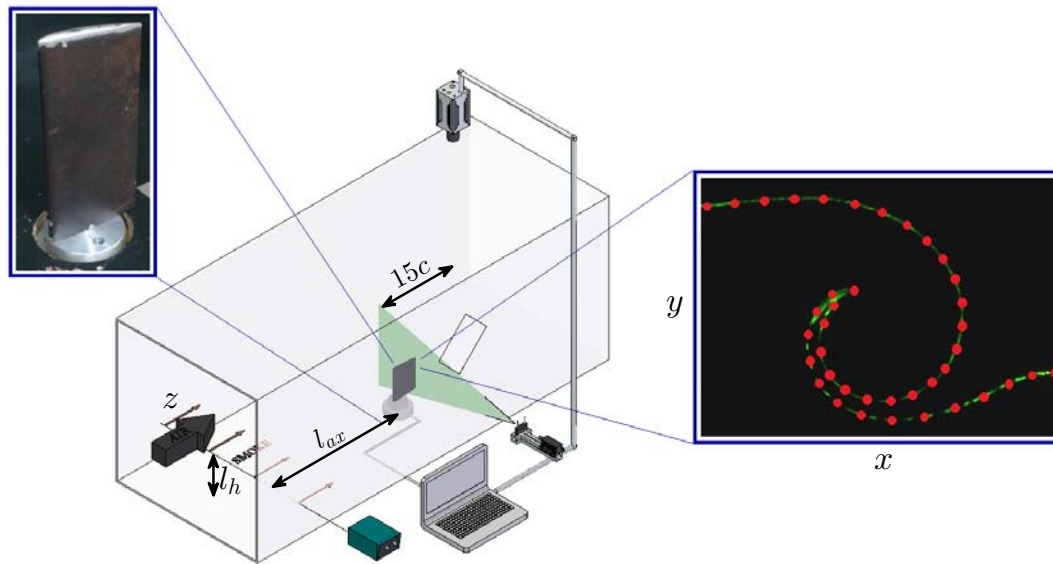
Figure 3.1: Experimental setup layout.

equations. The quantitative information can be compared with the Batchelor's model to characterise the wingtip vortex. The experimental procedure developed in this work may be applied to real aircraft in order to estimate the vortex strength, although the movement and width of the tracer would be more intense (or less precise) due to the existence of an atmospheric boundary layer, the effect of stratification and, finally, the turbulent mixing.

3.1 EXPERIMENTAL SETUP

Our experimental system is based on the smoke-wire technique as commented in chapter 2. This method allows us to visualise the airflow intersection of streak lines generated by the smoke-wire and the control plane highlighted by a laser sheet (see Figure 3.1). These two-dimensional flow visualisations provide qualitative information on complex airflow patterns produced by the wing model. Such an approach is a relatively simple way to study and characterise the wingtip vortices. In this case, we used a Nikon 105 mm lens (model AF Micro Nikkor 105mm) and f/2.8. Only a maximum frame rate of 250 fps was required for this experimental work although lower frame-rates were also used, so we believe that these images could have been obtained with a standard camera. We select only one snapshot to analyse the wingtip vortex in the near-field.

The experimental procedure requires coating the smoke-wire with oil manually. The wire is a resistor through which a high electrical current pulse is conducted and allows for a sudden temperature increase in the wire leading to the vaporisation oil temperature on the wire surface. At this moment, a discrete smoke surface is generated which follows the main stream passing through the wingtip thus reaching the control plane. In this area, the laser sheet highlights the intersection between the smoke surface and the control plane, where the smoke line is twisted according to the wingtip vortex velocity field (see the snapshot on the right-hand side in Figure 3.1). In this inset, the cartesian coordinate system is defined as follows: y and x-coordinates are spanwise and transverse (wall-normal) directions, respectively. The virtual origin in the (x, y)-plane will be described in the next section. The z-coordinate is the streamwise direction which is defined along the free stream. This coordinate is measured from the trailing edge of the model. Though we are able to measure the vortex strength (see sections below), it is worth mentioning that there is a constraint in the experimental method since it can not be extended to measure the velocity of the vortex in the streamwise

direction. This is related to the axial length of the smoke surface that is generated by the smoke-wire. The duration of the pulse to heat the wire is 25 ms, approximately. That means that the axial length of the smoke surface is near 30-40 cm taking into account the velocities tested in the wind tunnel.

A steady-state flow was achieved in the test section of the wind tunnel before any action was taken in the smoke wire. It is essential to synchronize all the actuators and elements in both the smoke-wire and digital camera systems. Once the wire current pulse is launched at $y = l_h$, the high-speed camera trigger has to activate the recording mode. The appearance/disappearance of the deformed smoke surface through the control plane is registered, and the subsequent snapshots are stored. Note that only the image with the highest intensity of the smoke will be analysed in several planes of the streamwise direction. Hence, these instantaneous pictures provide information regarding flow vortex patterns produced by the wing lift forces when the main stream passed through the airfoil. A set of experimental points $\vec{Q}_k^d$ has to be selected in these instantaneous frames (red points of the right inset in Figure 3.1). Consequently, a two-dimensional description of the vortex is gathered in the control plane. Every *kth* point is required for the numerical procedure regarding the control plane located at a certain distance z downstream from the wing trailing edge. Five control planes at z=0, c, $2c$, $3c$, $4c$, and $5c$ together with two representative values of W_∞ are used in this chapter (see below).

3.2   Post-processing the experimental results

As the smoke streak lines move downstream in the streamwise direction under steady-state conditions, a characteristic curve fitting can be obtained experimentally with the intersection of these smoke streak lines and the control plane, gathering all the red points $\vec{Q}_k^d$. As commented on above, this surface is perpendicular to the axial direction at a certain distance z. The choice of this 2D description of the wingtip vortex at consecutive axial distances lead, to some extent, to quantitative information regarding the path followed by the fluid particles which pass through the smoke wire located upstream from the NACA0012 wing model. We use the model reported by Batchelor [1964] to give an initial description of this experimental technique. The velocity field components (u, v, w) in a cylindrical coordinates (r, θ, z) are obtained as a solution based on the boundary-layer-type approximation: $\frac{\partial}{\partial z} << \frac{\partial}{\partial r}$ and $u << w$. This limitation explains the reason why this solution is an accurate model in the far field downstream from the airfoil: the axial velocity defect is small compared to the free-stream velocity, W_∞. The solution is computed after considering the boundary condition so that the far field tangential velocity follows the potential vortex pattern, i.e. $rv \rightarrow constant \equiv \Gamma_0/(2\pi)$ as $r \rightarrow \infty$, Γ_0 being the circulation of the vortex and

$$u(r, z) = 0, \tag{3.1a}$$

$$v(r, z) = \frac{\Gamma_0}{2\pi r}[1 - e^{-W_\infty r^2/4\nu z}], \tag{3.1b}$$

$$w(r, z) = W_\infty + \frac{\Gamma_0^2}{32\pi^2\nu z}B\left(\frac{W_\infty r^2}{4\nu z}\right) -$$
$$\left[\frac{\Gamma_0^2}{32\pi^2\nu}ln\left(\frac{W_\infty z}{\nu}\right) + \frac{W_\infty^2 L}{8\nu}\right]\frac{e^{-W_\infty r^2/4\nu z}}{z}, \tag{3.1c}$$

where $B(\xi) \equiv e^{-\xi}[ln\xi + E(\xi) - 0.807] + 2E(\xi) - 2E(2\xi)$, E is the exponential integral function, and ν represents the kinematic viscosity which is temperature dependent. The parameter L is an integration constant which depends on the airfoil lift coefficient, C_L, and the chord of the wing, c, following the
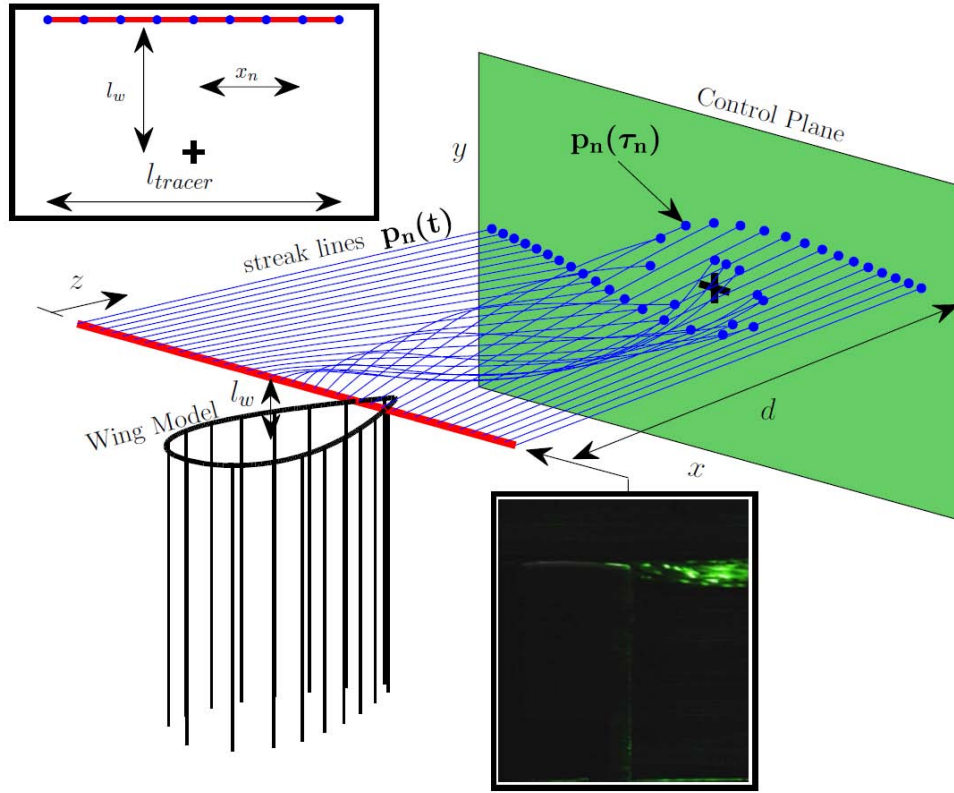
Figure 3.2: Numerical integration of streak lines up to the control plane alongside experimental visualization of the wingtip vortex origin.

expression:

$$L \sim \left(\frac{C_L c}{\pi}\right)^2. \tag{3.2}$$

The NACA0012 lift coefficient $C_L = 0.445$ has been experimentally determined for a single angle of attack value ($\alpha = 10°$) in the same experimental facility.

Variables and velocity components for the theoretical model can be displayed in dimensionless form according to the characteristic magnitudes given in equation (3.3):

$$\overline{r} = \frac{r}{c}, \tag{3.3a}$$

$$\overline{z} = \frac{z}{cRe_c}, \tag{3.3b}$$

$$\overline{v} = \frac{v}{W_\infty}, \tag{3.3c}$$

$$\overline{w} = \frac{w}{W_\infty}, \tag{3.3d}$$

where Re_c represents, as mentioned above, the chord based Reynolds number, $Re_c = W_\infty c/\nu$.

Therefore, we obtain the following equations of Batchelor's model:

$$\overline{v} = \frac{S}{\overline{r}}(1 - e^\eta), \tag{3.4a}$$

$$\overline{w} = 1 + \frac{S^2}{8\overline{z}}B(-\eta) - [S^2 \, ln(Re_c^2 \, (\overline{z} - \overline{z_0})) + \delta]\frac{e^\eta}{8(\overline{z} - \overline{z_0})}, \tag{3.4b}$$

where

$$S = \frac{\Gamma_0}{2\pi c W_\infty}, \tag{3.5a}$$

$$\eta = -\frac{\overline{r}^2}{4(\overline{z} - \overline{z_0})}, \tag{3.5b}$$

$$\delta = \frac{L}{c^2}. \tag{3.5c}$$

Two sets of experimental measurements have been performed for two different inlet main stream velocities: W_∞=5 an 15 m/s which correspond to Re_c =33,3×10³ ±1.26×10³, and Re_c =100× 10⁵±3.4×10³, respectively. The errors in the chord based Reynolds numbers are computed taking into account temperature (errors within ± 0.1K in the set of tests) and velocity fluctuations (errors within the turbulence intensity).

The work proposed by del Pino et al. [2011b] points out the relevance of adding one free parameter $\overline{z_0}$ to the Batchelor's model included in equations (3.4) and (3.5). This new parameter sets a virtual vortex origin in the streamwise direction which represents a different location of the origin from the wingtip in the airfoil. The axial origin in the self-similar solution of the governing equations is not well-defined, and the roll-up process takes place just behind the virtual vortex origin. This extra degree of freedom applied to the model enhances the theoretical curve fitting of the experimental results in the near field, thus avoiding the singularity of Batchelor's model near $\overline{z} = 0$ [see equation (3.4b)]. According to Batchelor's model, there are four free parameters: S and $\overline{z_0}$ (both dimensionless parameters are required to describe the vortex velocity field), and the vortex centre (x_0, y_0). We have included these last two parameters in the fitting procedure to avoid the effect of the vortex meandering (rapid and aleatory movement of the vortices in trailing vortex experiments). The radial coordinate is defined as,

$$r = \sqrt{(x - x_0)^2 + (y - y_0)^2}. \tag{3.6}$$

Due to the use of instantaneous snapshots, the experimental procedure developed in this work allows us to centre the vortex core for each axial location. This method was also used in del Pino et al. [2011b] to obtain the parameters of the vortex, thus providing very accurate results.

We model the smoke-wire with the horizontal line such as the red one shown in Figure 3.2. In addition, in the inset of the diagram, we plot the distance l_{tracer}, which corresponds to the numerical line from where the streak lines depart. We impose l_{tracer}=0.1 m in our numerics. A set of N equally-spaced points can be aligned along it. This segment passes through the wingtip end edge and therefore close to the vortex origin. Both $\overline{v}$ and $\overline{w}$ define the velocity field along with $u = 0$. Under steady state flow, at the initial time (t=0) these points are supposed to leave this initial segment following the velocity field. Each one of these n points defines a specific path defined by $\vec{p_n}(t) = [x_n(t), y_n(t), z_n(t)] = [r_n, \theta_n(t), z_n(t)]$ in cartesian or cylindrical coordinates, respectively, and where r is not time-dependent due to the constraint $u(t)$ =0.

Each one of these n points defines a specific path defined by $\vec{p_n}(t) = [x_n(t), y_n(t), z_n(t)]$. Every nth streak line can be obtained integrating the next system of three coupled ODEs numerically:

$$\frac{d}{dt}[x_n(t)] = \overline{V_x}(\overline{r}_n, \overline{z}_n(t)) W_\infty, \tag{3.7a}$$

$$\frac{d}{dt}[y_n(t)] = \overline{V_y}(\overline{r}_n, \overline{z}_n(t)) W_\infty, \tag{3.7b}$$

$$\frac{d}{dt}[z_n(t)] = \overline{V_z}(\overline{r}_n, \overline{z}_n(t)) W_\infty, \tag{3.7c}$$

where $\overline{r}_n = \sqrt{x_n^2 + y_n^2}/c$ and $(\overline{V_x}, \overline{V_y}, \overline{V_z})$ stand for the Batchelor's velocity field in Cartesian coordinates according to equation (3.4). The initial conditions for the previous system belong to the smoke-wire position: $x_n(t = 0)$ is linearly distributed along the wire, whereas:

$$y_n(t = 0) = l_w, \tag{3.8a}$$

$$z_n(t = 0) = -3c, \tag{3.8b}$$

l_w being equal to l_h-l, and the points x_n which lie along the initial segment which is located at the height $y_n(t = 0) = l_w$. The initial condition for the axial coordinate is constant and equals to -3c according to our experimental setup. The position of the wire was selected to provide a clear rolling spiral picture in the five planes studied for the velocities used. Noticing that the deformation of the smoke stream cannot start upstream of the vortex origin, as has been confirmed by the numerics.

As mentioned above, the control plane is a normal surface to the main stream direction that can be defined as $z_n(\tau_n)$ (green surface in Figure 3.2). This implies that each of the point paths has to be integrated up to $t = \tau_n$, so that it reaches this plane at a certain distance $z = d$, d being 0, c, 2c, 3c, 4c, and 5c. Every point path is obtained by integrating equation (3.7) with a 4th order Runge-Kutta method, and the intersection between the control plane ($z = d$) and the nth point path is located at $\vec{p}_n(\tau_n) = [r_n, \theta_n(\tau_n), d]$, where τ_n is the time required for each point to reach the control plane $z=d_i$.

Batchelor's model depends on free parameters $(\overline{z_0}, S)$ which must be computed. As a result, this set of numerical points $\vec{p}_n(\tau_n)$ which stems from the theoretical model provide a description of the specific velocity field. For this reason, it contains information regarding not only the flow patterns but also the velocity field within a bounded region passing from the starting smoke-wire through the wing model up to the control plane. Both the experimental $\vec{Q}_k$ and numerical $\vec{p}_n(\tau_n)$ set of points are gathered after aligning their vortex centres (x_0, y_0). This origin is represented by a cross symbol in Figures 3.2 and 3.3. To compute the vortex centre, it is necessary to match up experimental and numerical points within the control plane according to their relative positions. Given any point $\vec{p}_n(\tau_n)$, it is possible to find the closest point among the experimental set of points $\vec{Q}_k$. Afterwards, the closest experimental point to $\vec{p}_n(\tau_n)$ can be noted as $\vec{Q}_n$. This approach to obtaining a set of points is displayed in Figure 3.3. Based on the distance between every couple of points, the global objective function follows the equation

$$F(\overline{z_0}, S, x_0, y_0) = \sum_{n=1}^{N} ||\vec{p}_n(\tau_n) - \vec{Q}_n(x_0, y_0)||. \tag{3.9}$$

The applied optimization algorithm is a derivative-free method based on the simplex search method by Lagarias et al. [1998]. Furthermore, the fitting procedure can be accomplished simultaneously for multiple control planes $z = d_1, d_2, ... d_J$. Therefore, the optimization algorithm has to regard all the control planes in the same objective function:

$$F(\overline{z_0}, S) = \sum_{j=1}^{J} \sum_{n=1}^{N} ||\vec{p}_n^{d_j}(\tau_n) - \vec{Q}_n^{d_j}(x_0, y_0)||, \tag{3.10}$$

where $\vec{p}_n^{d_j}(\tau_n)$ and $\vec{Q}_n^{d_j}$ are the numerical and experimental sets of points located at the $z = d_j$ control surface. To accelerate the convergence of the simultaneous/global curve fitting, we use the values of the position of the centre at each plane (x_0, y_0) obtained from the local optimisation analysis.

This objective function implies an optimisation problem whose solution can be solved using Batchelor's

model ($\overline{z_0}$, S), and the experimental points $\vec{Q}_n$. This model is, therefore, the result of the fitting procedure in several control planes at different axial distances $z = d_1, d_2, ... d_J$. We remark that one limitation of this experimental technique stems from the lack of a clear pattern of the experimental points $\vec{Q}_n^{d_j}$ as the twisted smoke lines evolve downstream. For this reason, we apply this experimental technique only up to z=5c (near-field of the wingtip vortex). As the smoke moves in the streamwise direction, there is a mixing process due to the diffusion produced by the shear, and the wake instability from the wire. In any case, and though the average of the smoke thickness increases almost ten times, it does not change the main features of the airflow significantly.

We have repeated the fitting procedure technique for four different experiments performed during different days, obtaining a dispersion of the results of 2% in S. These results confirm a good experimental procedure and a suitable numerical scheme. Finally, it is worth mentioning again that the integration starts at z =-3c, providing the condition $\overline{z_0}Re_c c < $ -3c in all the results given in the next section.
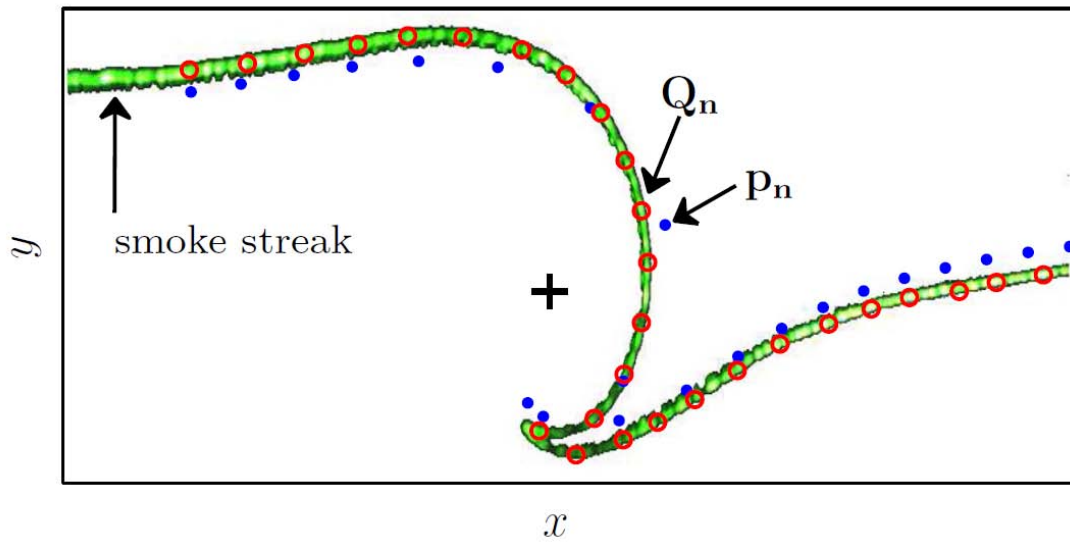
Figure 3.3: Smoke visualization at a single control plane (experimental black background removed). Experimental points ($\vec{Q}_k$) are depicted in red over the smoke streak. Blue points ($\vec{p}_n$) represent the numerical points obtained using the theoretical model (3.4). $\vec{Q}_n$ is the closest point to ($\vec{p}_n$) in the $\vec{Q}_k$ set of points.

3.3   Results

EExperimental smoke streaks are displayed in Figures 3.4 and 3.5 for our two representative chord-based Reynolds numbers Re_c =33.3 × 10³ and Re_c =100 × 10³, respectively, for six control planes: z=0, c, 2c, 3c, 4c, and 5c in (a)-(f), respectively. Flow visualisations are compared with Batchelor's model for every case including both the individual and the simultaneous curve fittings. As depicted in these figures, the individual curve fitting in a red solid line is closer to the experimental smoke streak (in green). Since this individual fitting is the result of just a local adjustment in a particular downstream location, it is not valid for the whole axial range. In contrast, the simultaneous/global curve fittings represented in dashed blue lines aim to provide a better three-dimensional description for a specific Reynolds number. Though we introduce the virtual origin $\overline{z_0}$, the reader must notice that Batchelor's model does not accurately predict the vortex formation in the very near-field. The model is singular near z=0, so it is not able to predict the velocity field in that region. This fact also explains the poor agreement between the simultaneous fitting model and the experimental visualisation at z=0 (Figures 3.4(a) and 3.5(a)).

(a) z=0

(b) z=1c

(c) z=2c

(d) z=3c

(e) z=4c

(f) z=5c

Figure 3.4: Comparison between the experimental smoke streak (green) and the numerical results for the control planes at several locations for $Re_c = 33.3 \times 10^3$. Batchelor's solution corresponding to the simultaneous fitting is represented in dashed blue and the individual fitting in solid red.

In order to analyze the influence of the wake produced by the wire on the airflow patterns, the Reynolds number based on the diameter of the wire, Re_D, has been calculated. The values are in the range between 60 and 168 for the tested velocities. Neglecting the effect of the short heating time needed to evaporate the oil. Taking into account Williamson's review (1996), the flow belongs to the laminar 2D vortex shedding and the 3D transition regimes. Due to the fact that the smoke is generated on the surface of the wire, any wake instability stems from an increase of the width of smoke lines in the case of 2D instabilities, while 3D ones break on the smoke lines in the spanwise direction. The last experimental evidence can be observed in Figures 3.4 and 3.5. The main effect is the increase of the uncertainty in the determination of the points $\vec{Q}_k^d$ selected for the smoke line. We can confirm that the error is lower than 3% for the parameters of Batchelor's model.

All the results can be seen in table 3.1, where we show the values for S and $\overline{z_0}$ depicted in Figures 3.6 and 3.7. Both parameters increase with the streamwise direction. This feature is very common using other parameters related to the wingtip vortex, e.g. meandering of the vortex core, [see del Pino et al., 2011a]. The main strength of the experimental technique presented is the observation of this behaviour even with the use of Batchelor's model. In addition, we observed that these figures show that the global curve fitting attains final values inside the range of the individual curve fittings. This characteristic makes us believe that the numerical approach proposed is robust. We must also highlight that the values reported here do not use

(a) z=0

(b) z=c

(c) z=2c

(d) z=3c

(e) z=4c

(f) z=5c

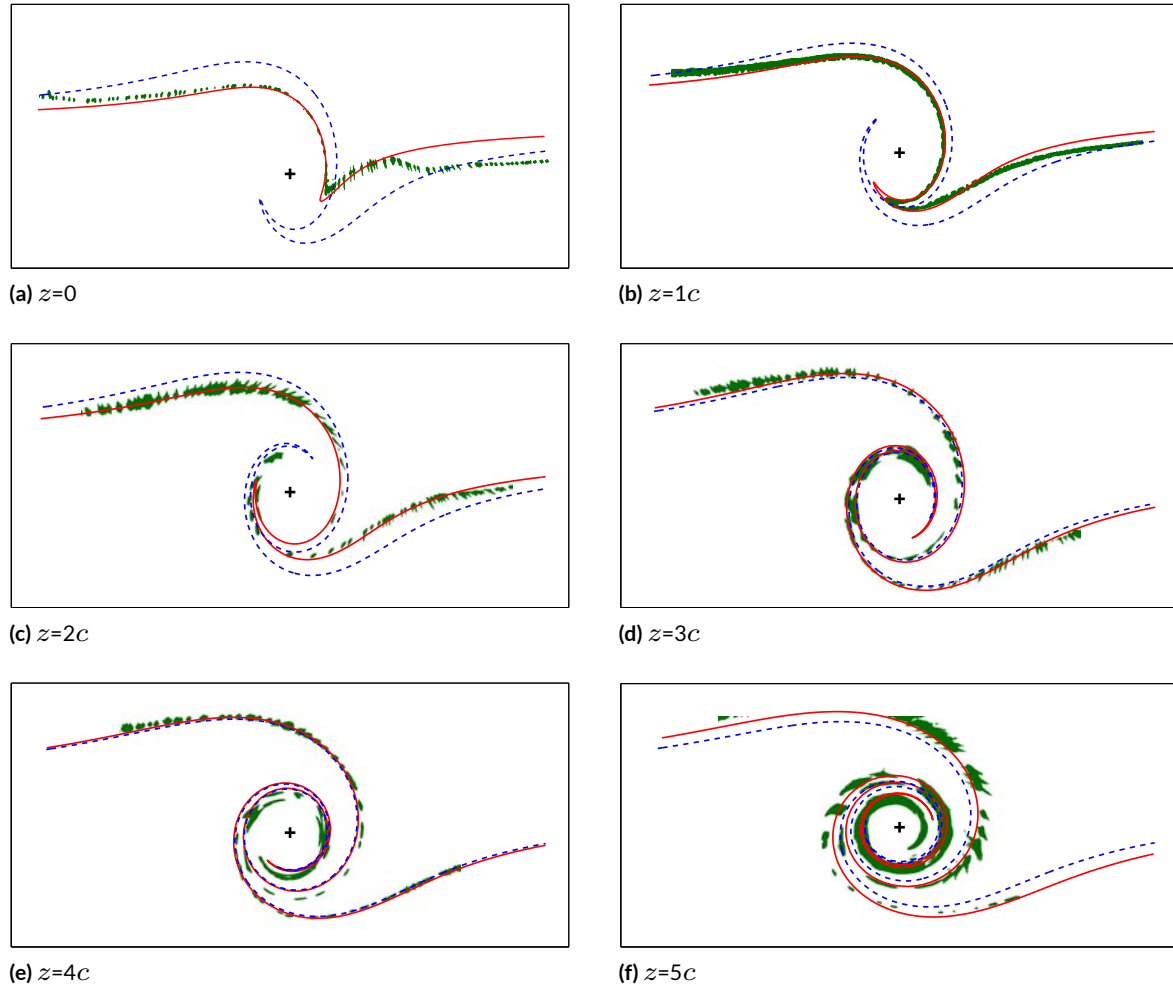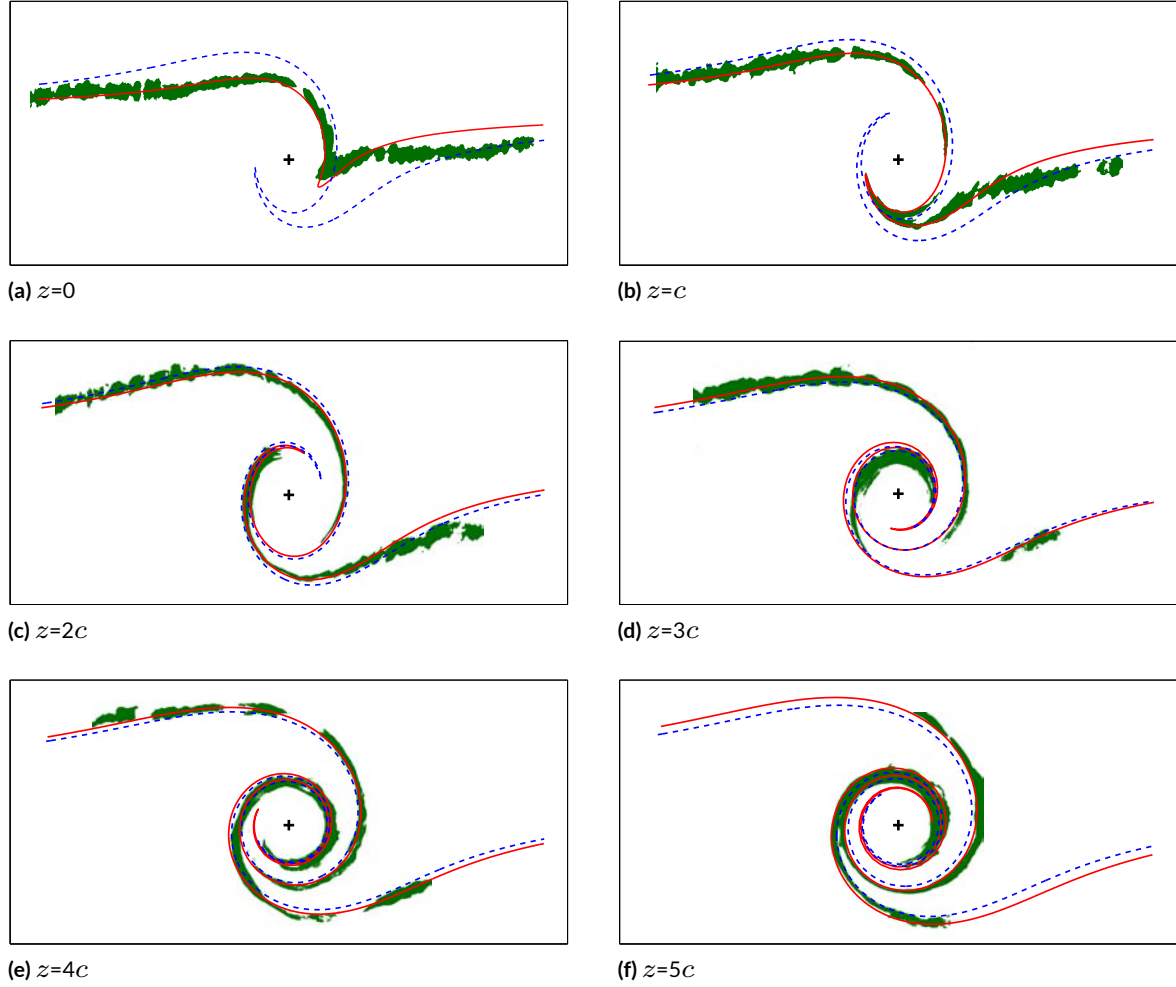**Figure 3.5:** Comparison between the experimental smoke streak (green) and the numerical results at several locations for $Re_c = 10^5$. Batchelor's solution corresponding to the simultaneous curve fitting is represented in dashed blue and the individual fitting in solid red.

quantitative techniques such as LDA, PIV or hot wire. Although quite analogous results were obtained by a stereo-PIV system in del Pino et al. [2011b], but were obtained in a hydraulic tank with the same airfoil model. These results correspond to Re_c =20× 10^3 and 40×10^3, where Batchelor's model was fitted individually for several control planes (up to z/c=16). More specifically, we show the average values of S/α and $\overline{z_0}$ for z/c=0.5, 3, 4, and 6 in order to compare the simultaneous curve fitting of the current work for Re_c =33.3× 10^3 and 100×10^3.

The dependence of parameters S and $\overline{z_0}$ as function of Re_c is depicted in Figures 3.8. In this figure, the simultaneous values of S and $\overline{z_0}$ are represented by non-filled triangles and circles, respectively, while the data provided in del Pino et al. [2011b] are shown using the same filled symbols. One can observe a reasonably good agreement between the PIV results and the ones presented using our experimental technique combined with the numerical integration using the same theoretical model. This fact confirms the suitability of our experimental procedure. In addition, we also confirm again that the Reynolds number has a weak influence on the theoretical parameters in the near-field of the wingtip vortex at low-to-moderate values. This range of Re_c is handy to study the aerodynamic of Unmanned Aerial Vehicles, UAV's. It is still an open question if these parameters will be almost constant up to Re_c=O(10^7) which correspond to real aircraft applications. Unfortunately, our wind tunnel facility does not achieve the mean velocity required to that end.

Table 3.1: Fitted values for the free parameter S and $\overline{z_0}$ in the Batchelor's model

	z/c	$Re_c = 33.3 \times 10^3$		$Re_c = 100 \times 10^3$	
S	0		0.01204		0.01235
	1		0.01792		0.01979
	2	$S = 0.02527$	0.01794	$S = 0.02705$	0.02447
	3		0.02729		0.02922
	4		0.02622		0.02960
	5		0.03118		0.03128
$\overline{z_0}$	0		-1.46		-1.34
	1		-1.09		-1.26
	2	$\overline{z_0} = -6.99$	-1.82	$\overline{z_0} = -7.79$	-1.23
	3		-6.26		-4.38
$\times 10^{-4}$	4		-6.61		-6.83
	5		-7.80		-8.69

Figure 3.6: Axial evolution of fitted parameters (S and $\overline{z_0}$) according to Batchelor's model for $Re_c = 33.3 \times 10^3$. Both individual (discrete points) and simultaneous fitting results are shown.
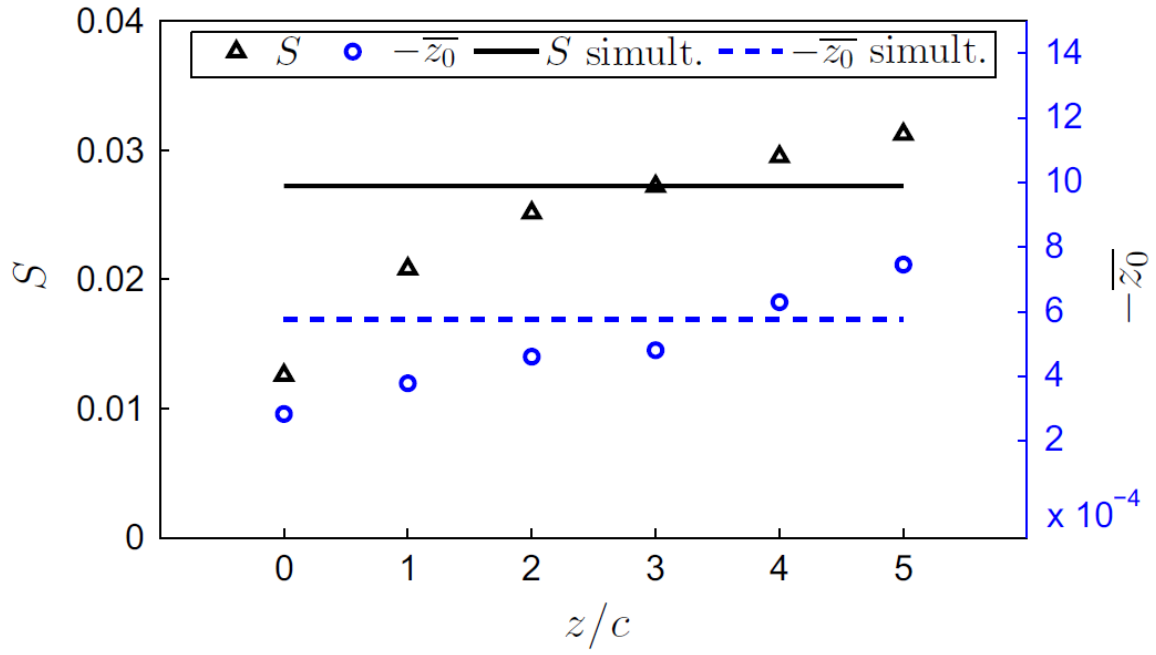
Figure 3.7: Axial evolution of fitted parameters (S and $\overline{z_0}$) according to Batchelor's model for $Re_c = 100 \times 10^3$. Both individual (discrete points) and simultaneous fitting results are shown.
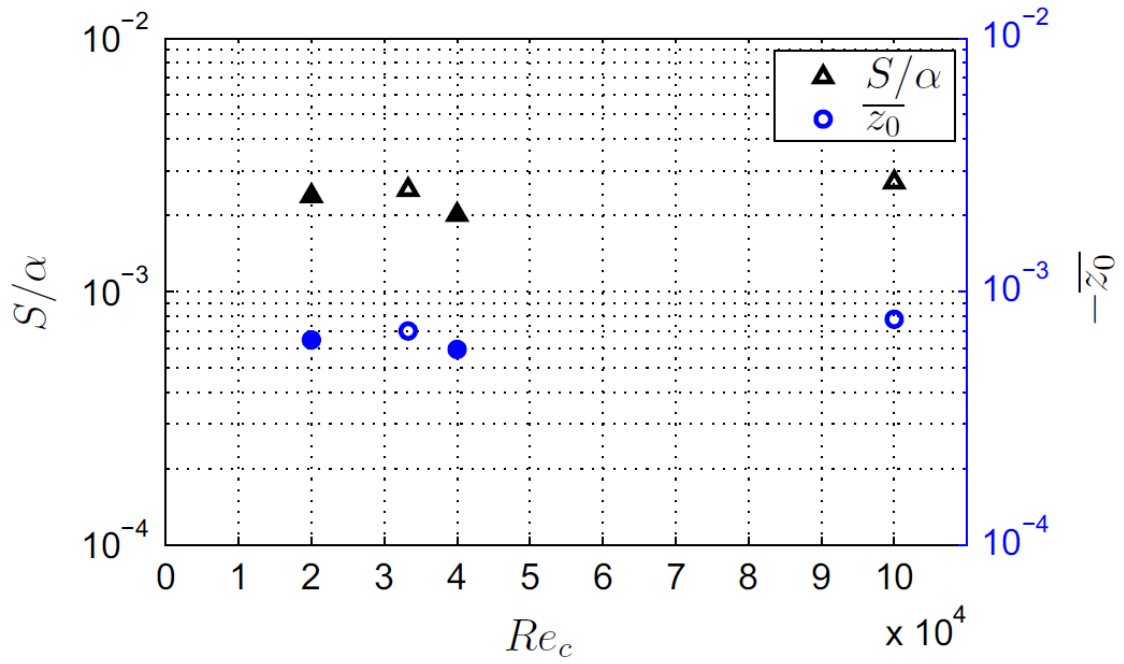
Figure 3.8: Virtual origins of the Batchelor's model $\overline{z_0}$ and S/α for different values of Re_c. Points for $Re_c = 20 \times 10^3$ and 40×10^3 are reported in del Pino et al. [2011b] with filled triangles and circles. The non-filled triangles and circles correspond to the simultaneous curve fitting of this experimental study.

(a)   **(b)**
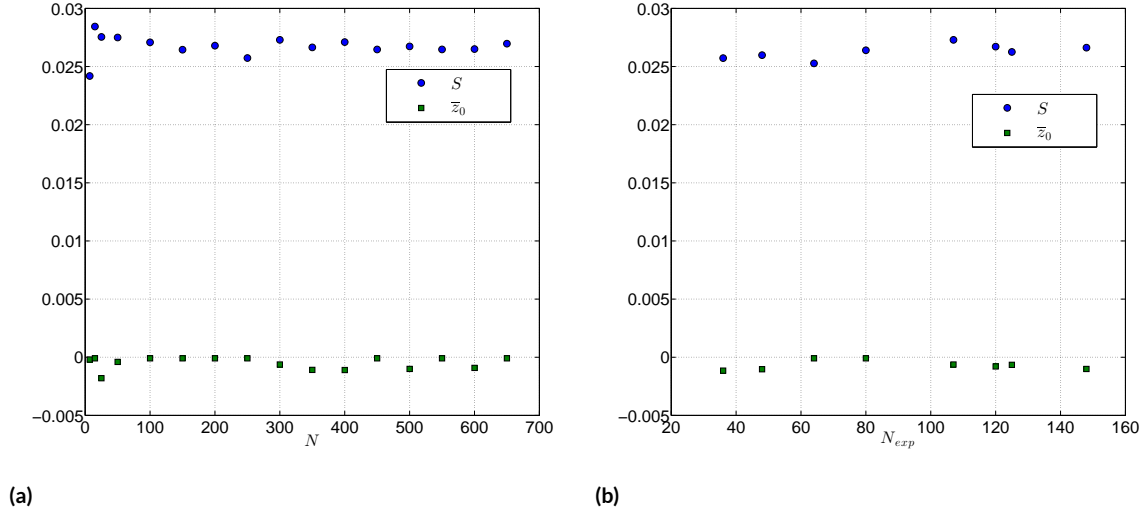
Figure 3.9: Parameters S and $\overline{z}_0$ as function of the theoretical points N, for N_{exp}=107 (a), and (b) of the number of experimental points N_{exp} for N=300 (b). In both cases Re =100×10^3 and z=3c.

3.4   Sensitivity to optimization parameters.

In this section, we study the influence of different parameters which are present in the optimisation procedure. Recall that we solve equation 3.9 to find four parameters, S, $\overline{z}_0$, x_0 and y_0. We impose two different numbers of points: N theoretical points to integrate the velocity field of the vortex, and N_{exp} experimental points which describe the spiral, as shown in Figs. 3.1, and 3.3. We check the effect of the variation of these parameters for the case of Re =100×10^3 and z =3c. In figure 3.9 (a) we show the evolution of the two main parameters obtained from the optimisation for N_{exp}=107, and a different number of theoretical points. It can be observed that there are small variations in a number of theoretical points greater than 250, approximately. For this reason, we establish N=300, so the changes in the parameter S are lower than 2.5% concerning the mean value for any value of N in the range 250-650. More fluctuations are observed in the case of $\overline{z}_0$, though they are considered acceptable. In Figure 3.9 (b) we show the effect of N_{exp} using the same image, and N=300. It is clear again that N_{exp} has a weak influence on the variation of the main parameters in the optimisation procedure, whenever this number is approximately greater than 100. For example, if one compares the value of S to the mean value for any N_{exp}, the error is lower than 3.8%, which is considered very small. We set N_{exp}=107 in our computations.

Finally, we have modified the length of the numerical line used as a tracer (see the line from where streak lines departure in Fig. 3.2). We show in figure 3.10 the results and it can be observed that for lengths greater than 0.07, the solution does not change significantly. We consider l_{tracer}=0.1 m (or $\phi = l_{tracer}/0.1$=1) in our computations.

3.5   Conclusions

A novel experimental technique has been proposed to characterise wingtip vortices. Our approach is based on a low cost experimental system which describes the vortex velocity field based on smoke-wire flow visualisations and one theoretical vortex model. Experimental tests have been performed in a subsonic wind tunnel using a NACA0012 airfoil with a single angle of attack $\alpha = 10°$, and two different Reynolds numbers (33.3 and 10×10^3). Batchelor's model, which only depends on two free parameters, i.e. the vortex strength, S, and the virtual origin, z_0 has been fitted for six control planes at different locations in the near-field (up to
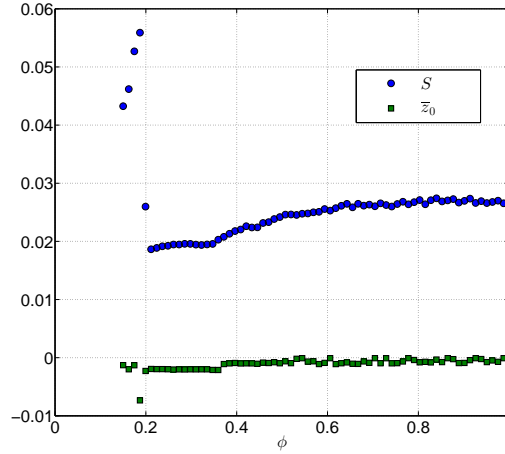
Figure 3.10: Parameters S and $\overline{z}_0$ as function of the length of the numerical integration tracer line for the case $Re = 100 \times 10^3$ and z=3c.

z=5c). Results for each control plane have been gathered to find the difference between global and individual curve fittings, showing the vortex evolution in the near-field. Experimental smoke and numerical streaks are compared, finding slight differences between the real flow pattern and the one adjusted by the theoretical model. The final values of S and z_0 obtained by this experimental method have been compared with those provided by del Pino et al. [2011b] using the stereo-PIV technique. We find a reasonably good agreement between the methods. The values given in this work also detect the weak influence of the Reynolds number on the parameters which characterise Batchelor's model in the near-field of the wingtip vortex. This work is a preliminary step to presenting the strengths of this novel technique. Further work can be performed to test its feasibility with more complex theoretical models, which will provide a more accurate description of the near-field vortex structure and the roll-up process, e.g. Moore and Safmann's model.

4

A complementary experimental and numerical study of the influence of Reynolds number on theoretical models for wing-tip vortices

Several types of (symmetric) airfoils have been widely used to analyse the wingtip vortex development, in particular, the airfoil NACA0012 from different points of view. Giuni [2013] examined the vortex formation on square and round tips finding that the vortex shape influenced the rolling-up process strongly. Wang et al. [2016] discovered that the ground effect promotes the merging process and accelerates the vortices' rotation around one another. Nash et al. [1999]; Desquesnes et al. [2007]; Pröbsting et al. [2015] reported the tonal noise generation and the identification of its source at moderate Reynolds numbers (30-230×10^3). On the other hand, Lombard et al. [2015] provided Implicit Large Eddy Simulations of the roll-up process at Re=1200×10^3, and the comparison with experimental measurements in the near field given by Chow et al. [1997]. Finally, Hoarau et al. [2003] identified two transition mechanisms to turbulence for Re between 800 and 10×10^3: a period-doubling scenario and the development of the shear-layer instability. Besides, Jones et al. [2008] performed direct numerical simulations (DNS) at Re=50×10^3, showing three-dimensional absolute instability of the two-dimensional vortex shedding that occurs naturally. These 3D perturbations were amplified in the braid region of developing vortices and subsequently convected upstream by local regions of reverse flow, within which the upstream velocity magnitude substantially exceeded that of the time-average. Later, the same authors have found that the onset of absolute instabilities was not linked to the laminar separation bubble phenomenon [see Jones et al., 2010]. Other researchers have been capable of reducing the computational cost of doing numerics using a Parabolic Navier-Stokes (PNS) algorithm and comparing their results with those given by a NACA0012 [see Paredes et al., 2013]. Moreover, the integration between computational and experimental fluid dynamics (CFD, EFD) is a new trend entitled 'data assimilation in fluid dynamics' [see Suzuki, 2015]. In fact, Suzuki et al. [2009a,b] used a NACA0012 airfoil to develop a hybrid unsteady-flow simulation technique to integrate DNS and Particle Tracking Velocimetry (PTV). In particular, they studied in detail the vortex shedding phenomenon under a deep stall condition (α=$15°$), giving lift and drag coefficients as a function of Re in the range of Re=1-10×10^3. Very recently, Martinez-Aranda et al. [2016] also provided aerodynamic characteristics of the NACA0012 airfoil for different aspect ratios.

In this chapter, we provide a set of data from three points of view: numerics, experiments and theory. First, the experimental set-up along with the dimensionless parameters and measurement techniques, are briefly introduced in section 2. Second, we describe in detail the numerical scheme and the grid convergence. Subsequently, DNS together with PIV results are accounted for and discussed adequately in the fourth section, where we compare these results and their connection with theoretical models. Lastly, we show the main conclusions drawn in this study. Our primary goal is to explore the influence of the Reynolds number on the theoretical parameters in the range of ultra-low or low values both experimental and numerically since this dependence has not been considered elsewhere. Very recently, the vortex strength has given against Reynolds numbers at low-to-moderate values using smoke visualisations in Serrano-Aguilera et al. [2016] for the Batchelor's model in comparison with those provided by Stereo-PIV in del Pino et al. [2011b]. For this reason, we explore in this work theory, numerics and experiments to give a whole scenario of the wingtip vortex from Re_c=0.3×10^3 to Re_c=20×10^3.

4.1   POST-PROCESSING DATA

Vortices are so sensitive that they are disturbed by turbulence, which causes random shifts in the centre of the vortex. This phenomenon is known as meandering and it hinders experimental measurements (see section 1.3). Once the pair of images to be processed was determined, the particles' displacement between them and, therefore, the velocity field at each instant was obtained. Once the velocity field was determined, the vortex core corresponded to the maximum point of vorticity. Using equation 4.1, the location of the identified vorticity peak fell onto the grid point.

$$(\omega_Z)_{i,j} = \frac{\Gamma_{i,j}}{4\Delta x \Delta y}, \tag{4.1}$$

where

$$\begin{aligned}
\Gamma_{i,j} = &\frac{1}{2}\Delta x(u_{i-1,j-1} + 2u_{i,j-1} + u_{i+1,j-1}), \\
&+\frac{1}{2}\Delta y(v_{i+1,j-1} + 2v_{i+1,j} + v_{i+1,j+1}), \\
&-\frac{1}{2}\Delta x(u_{i+1,j+1} + 2u_{i,j+1} + u_{i-1,j+1}), \\
&-\frac{1}{2}\Delta y(v_{i-1,j+1} + 2v_{i-1,j} + v_{i-1,j-1}).
\end{aligned} \tag{4.2}$$

A 2-dimensional second order polynomial function was used to fit the measured vortex field in the adjacent points. The vorticity peak location improved the accuracy when it came to identifying to identify the vortex core at the sub-grid interpolation level, which is shown as follows:

$$P(y, z) = a_1 + a_2 y^2 + a_3 z^2 + a_4 yz + a_5 y + a_6 z. \tag{4.3}$$

where six unknown coefficients were determined by the maximum of the function, and the coordinates of the vortex core are:

$$y_{cv} = \frac{-(2a_3a_5 - a_4a_6)}{(-a_4^2 + 4a_2a_3)}, \tag{4.4}$$

$$z_{cv} = \frac{-(2a_2a_6 - a_4a_5)}{(-a_4^2 + 4a_2a_3)}. \tag{4.5}$$
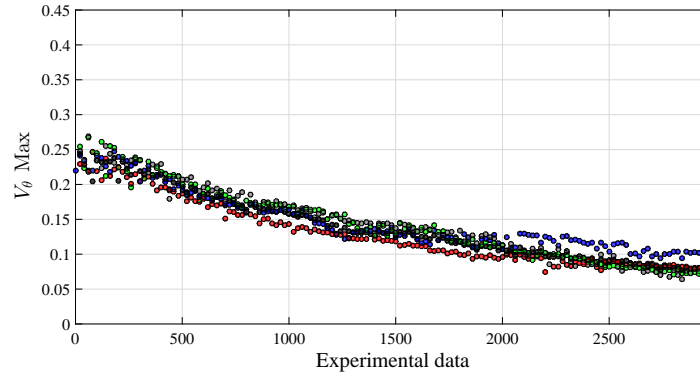
Figure 4.1: Re_c=7$\times$10^3. Maximum of azimuthal velocity for each experiment in the same case of study.

As the experimental studies have a certain error in the estimation of the results, four different experiments have been carried out for each case study. In the data post-processing, it has been verified the four experiments have the same trend for preset parameters, rejecting the incorrect experimental data (see Figure 4.1). To obtain the average of the results, and due to the meandering or random motion of the vortex, the position of the vortex is not the same in each experimental frame. For this reason, we use a common mesh for the experiments. Once the centre of the vortex was determined, each experimental profile was "re-centred" at the same instant of time and linearly interpolated on the common mesh. The final result consisted of the mean value of four different experimental tests in each plane of study, such as the velocity and vorticity fields represented in Figure 4.2.

(a)   **(b)**
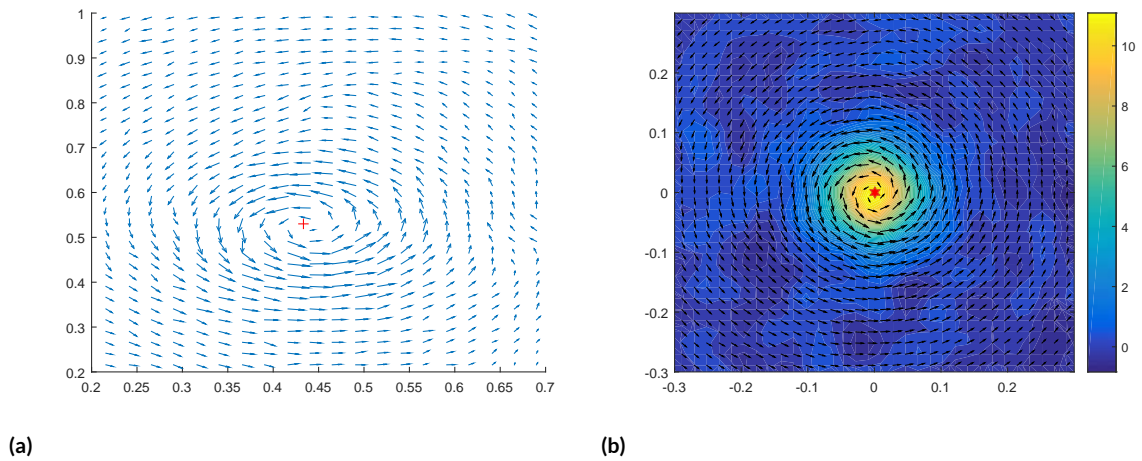
Figure 4.2: Vortex core before (a) and after (b) being "re-centred".

[]

[]
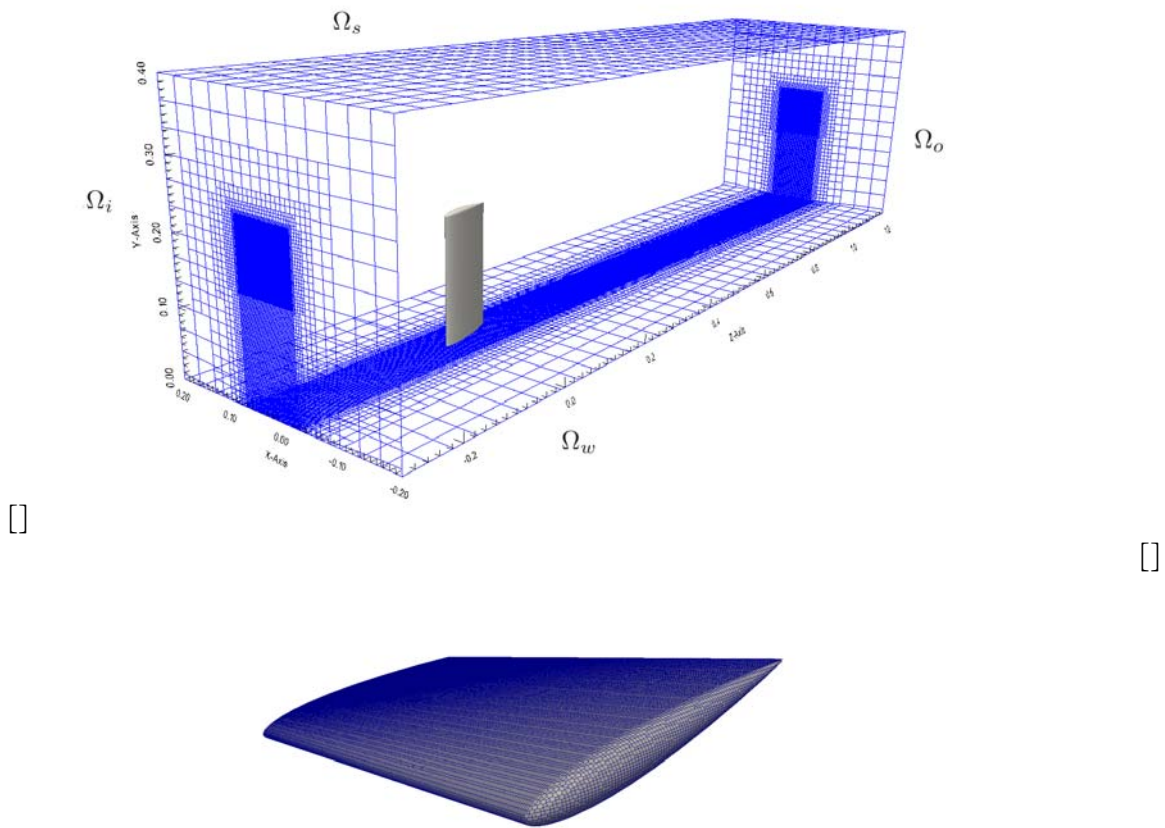
Figure 4.3: Computational domain (a) and detailed mesh of the wing model inside the computational domain (b).

4.2   Numerical Scheme

We solve the Navier-Stokes equations in the computational domain D shown in detail in Figure 4.3. This domain simulates a wind tunnel with a cross-section of $0.4 \times 0.4 \, \mathrm{m}^2$ and $1.5 \, \mathrm{m}$ long where the wing model NACA0012 airfoil is located vertically inside for a constant angle of attack, $\alpha = 9°$. This computational domain allowed us to obtain numerical results up to eleven chords downstream the wing. The numerical spatial domain is slightly smaller than the experimental setup due to the computational cost of doing DNS. Nevertheless, the comparison between DNS and experimental data shows an excellent agreement, so boundary conditions reproduce the experimental arrangement precisely.

To obtain numerical results, we use the dimensionless, incompressible Navier-Stokes equations which are described as follows,

$$\nabla \cdot v^* = 0, \tag{4.6}$$

$$\frac{\partial v^*}{\partial t^*} + v^* \cdot \nabla v^* + \nabla P^* - \frac{1}{Re_c}\nabla^2 v^* = 0, \tag{4.7}$$

where $v^* = (u^*, v^*, w^*)$ and P^* denote the scaled velocity vector and pressure, respectively, in the x^*, y^* and z^* non-dimensional directions in a Cartesian coordinate system, being z^* the axial coordinate. We use the chord of the wing model c as the characteristic length, and also the free-stream velocity W_∞ to render the dimensionless equations, so that c/W_∞ and $\rho W_\infty^2$ are the time and pressure scales, respectively, being ρ the density of the fluid. Thus, the chord-based Reynolds number is defined as $Re = cW_\infty/\nu$, where ν is the kinematic viscosity of the fluid which is highly temperature dependent.

The origin of the coordinate system for the simulations is located at the lower wall at the centre of the attack cross-section of the wing model. The boundary of the computational domain was decomposed into four surfaces: the inlet surface Ω_i at $z^* = z/c = -3$; the outlet surface Ω_o at $z^* = 12$; the lower surface and the surface of the wing model Ω_w; and the upper and lateral surfaces Ω_s. Three non-structured, uniform meshes of hexahedral elements were used. For all meshes, the axial dimension of each cell is 25 % greater than those given for the coordinates x and y, the latter two of which were equal. These meshes have been refined at the wingtip along the axial coordinate so as to ensure accurate numerical results for the trailing vortex. Some properties of each mesh are found in table 4.1.

Characteristics	Mesh 1	Mesh 2	Mesh 3
Min axial dimension (mm)	1.9531	1.3023	0.9756
Min x, y dimensions (mm)	1.5625	1.0414	0.7813
Cells on wing width	7	11	15
Points of mesh	4090169	13264686	31242495

Table 4.1: Mesh dimensions.

Equations (4.6) and (4.7) are solved with the following boundary conditions:

$$v^*(z^*, t^*) = (1, 0, 0), \quad z^* \in \Omega_i, \, t^* > 0, \tag{4.8}$$

$$P^* n - n \cdot \nabla v^*(z^*, t^*)/Re = 0, \quad z^* \in \Omega_o, \, t^* > 0, \tag{4.9}$$

$$v^*(z^*, t^*) = 0, \quad z^* \in \Omega_w, \, t^* > 0, \tag{4.10}$$

$$n \cdot v^*(z^*, t^*) = 0,$$

$$\nabla(t \cdot v^*(z^*, t^*)) = 0, \quad z^* \in \Omega_s, \, t^* > 0, \tag{4.11}$$

where z^* represents the vector (x^*, y^*, z^*), while n and t are normal and tangential surface vectors projected outside the computational domain, respectively.

A uniform velocity field, W_∞, parallel to the axial coordinate z is imposed at the inlet [see equation. 4.8]. Thus, the Dirichlet boundary condition for the velocity field at Ω_i depends on the chord-based Reynolds number. At the outlet surface, Ω_o, we set an open boundary condition [see equation (4.9)], which verifies a homogeneous Neumann condition in a weak sense. This last condition is equivalent to impose the normal component of the stress tensor to zero, which constitutes a weak condition for the velocity field downstream the wing, thus minimizing the possibility of numerical oscillations and reflections of outgoing waves. Null velocity is set at the lower wall, and the wing model surface Ω_w and slip conditions are applied to the upper wall and lateral surfaces, Ω_s. Therefore, non-slip boundary conditions are applied to walls, as shown in equation (4.10), and slip boundary conditions are imposed at lateral surfaces equation (4.11). The pressure values at Ω_i, Ω_w and Ω_s are implicitly obtained using the continuity equation (4.6). Finally, the initial condition for the velocity field also depends on the chord-based Reynolds number as follows:

$$v^*(z^*, 0) = (1, 0, 0), \quad z \in D. \tag{4.12}$$

The Navier-Stokes equations (4.6) and (4.7) are discretized using the finite volume method in the computational fluid dynamics software and open-source package OpenFOAM. The solver simpleFOAM, which provides an SST $k - w$ turbulent model, was used to obtain a first solution from the initial condition. Then, a DNS simulation was performed using the solver icoFOAM to get the steady final solution of the problem in the whole domain. The spatial discretization was conducted with a linear scheme (central differencing) and the time discretization was performed with an implicit Euler scheme. The numerical simulations were carried out in parallel on the *Picasso* supercomputer with forty-eight processors. This supercomputer belongs to the Spanish Supercomputer Network (RES), and it includes a seven-node cluster of 80 cores and 2 TB RAM computers, 32 nodes with 16 cores, 41 nodes with 24 cores and 16 nodes with 2 GPUs each, totalling 63 TFLOP/s. The calculations typically took about four weeks with mesh 3, one week with mesh 2 and one day with mesh 1. To solve incompressible flows, OpenFOAM uses SIMPLE and PISO algorithms, in which pressure is used to obtain a solenoidal velocity field. The pressure field verifies homogeneous Neumann conditions at all surfaces except at output surface, in which its value is set to zero. The reader must notice that once the post-processing procedure of the results has been completed, we considered the cylindrical polar coordinates with the same orientation shown above, but with origin at the wingtip at the trailing edge. The mean values presented in the following section are based on four different experiments, while we consider one snapshot to provide the average value of the direct numerical simulations. In addition, all the standard deviation values shown are given by using one hundred steps of 3.6 degrees of evenly distributed data in the azimuthal direction.

66

4.3   Theoretical models: Batchelor, and Moore & Saffman

We briefly introduce in this section the base flow and the parameters of these theoretical models. The main constraint is that the stall angle of attack cannot be reached in the airfoil used. More information is given in del Pino et al. [2011b] or Serrano-Aguilera et al. [2016]. We use the model reported by Batchelor [1964] to give an initial description of this experimental technique. The velocity field components (u, v, w) in a cylindrical coordinates (r, θ, z) are obtained as a solution based on the boundary-layer-type approximation: $\frac{\partial}{\partial z} << \frac{\partial}{\partial r}$ and $u << w$. This limitation explains the reason why this solution is an accurate model in the far field downstream from the airfoil: the axial velocity defect is small compared to the free-stream velocity, W_∞. The solution is computed after considering the boundary condition so that the far field tangential velocity follows the potential vortex pattern, i.e. $rv \to constant \equiv \Gamma_0/(2\pi)$ as $r \to \infty$, Γ_0 being the circulation of the vortex and

$$u(r, z) = 0, \tag{4.13a}$$

$$v(r, z) = \frac{\Gamma_0}{2\pi r}[1 - e^{-W_\infty r^2/4\nu z}], \tag{4.13b}$$

$$\tag{4.13c}$$

We avoid the axial component $w(r, z)$ since we obtain experimental data from 2D-PIV.

Variables and velocity components for the theoretical model can be displayed in dimensionless form according to the characteristic magnitudes given in equation (4.14):

$$\overline{r} = \frac{r}{c}, \tag{4.14a}$$

$$\overline{z} = \frac{z}{c}, \tag{4.14b}$$

$$\overline{v} = \frac{v}{W_\infty}, \tag{4.14c}$$

$$\tag{4.14d}$$

Therefore, we obtain the following equations of Batchelor's model:

$$\overline{v} = \frac{S}{\overline{r}}\left(1 - e^\eta\right), \tag{4.15}$$

where

$$S = \frac{\Gamma_0}{2\pi c W_\infty}, \tag{4.16a}$$

$$\eta = -\frac{\overline{r}^2}{4(\overline{z} - \overline{z_0})}. \tag{4.16b}$$

The work proposed by del Pino et al. [2011b] points out the relevance of adding one free parameter $\overline{z_0}$ to the Batchelor's model included in equations. (4.15) and (4.16). This new parameter sets a virtual vortex origin in the streamwise direction which represents a different location of the origin from the wingtip in the airfoil. The axial origin in the self-similar solution of the governing equations is not well-defined, and the roll-up process takes place just behind the virtual vortex origin. This extra degree of freedom applied to the

model enhances the theoretical curve fitting of the experimental results in the near field, thus avoiding the singularity of Batchelor's model near $\overline{z} = 0$ [see equation. (4.15)]. According to Batchelor's model, there are two free parameters: S and $\overline{z}_{0B}$.

In terms of the non-dimensional variables (4.14), Moore & Saffman's solution for the azimuthal and axial velocity can be expressed as

$$\overline{v} = \frac{b}{(\overline{z} - \overline{z}_{0MS})^{n/2}} V_n(\eta) \,, \tag{4.17}$$

where b is a non-dimensional constant related to the vortex circulation, n represents the vortex decay, $\overline{z}_{0MS}$ is the virtual origin of Moore & Saffman's model, and $V_n(\eta)$ depends on the gamma function and the hypergeometric function of the first kind. Thus, three parameters must be adjusted in this model: b, n and $\overline{z}_{0MS}$. As mentioned above, the adjustment of theoretical parameters by using both numerical and experimental data has been carried out following the procedure is given in del Pino et al. [2011b]. Again, we do not compute the axial velocity $\overline{w}$ because we performed 2D-PIV.

4.4   Results and discussion

4.4.1   Comparison between 2D-PIV and 3D-DNS for $Re = 7 \times 10^3$

Average vorticity data plus associated 2D vectors of velocity field are presented in Figure 4.4 for $Re_c = 7 \times 10^3$ at $\overline{z}=3$. This comparison has been given taking into account the re-centre process explained in the second section, thus avoiding the undesirable effect of meandering in the vortex core. The results show a reasonably good agreement between DNS and 2D-PIV measurements. The shape of the vortical flow structure near the vortex core is almost symmetrical both numerically and experimentally since the roll-up process has been already finished.

(a) z=3c **(b)** z=3c
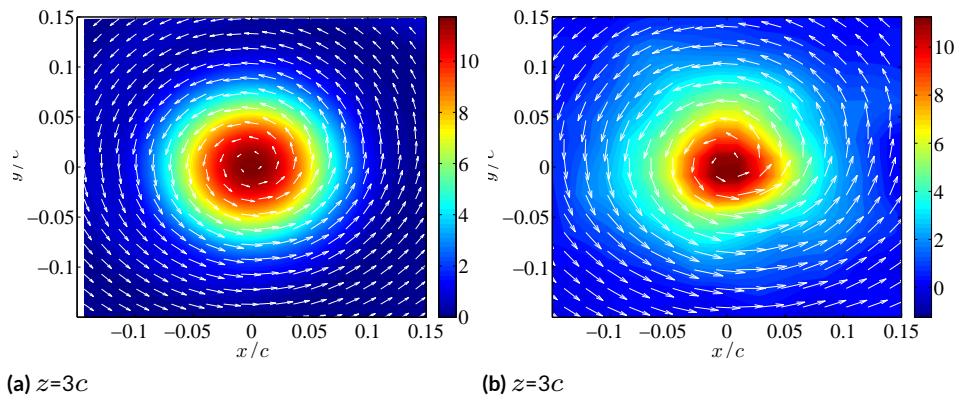
Figure 4.4: Experimental and numerical comparison for vorticity field plus associated vector of the velocity field from DNS (a) and experiments (b).

To double check the goodness of DNS computations against experimental data, azimuthal velocity profiles are also shown in Figure 4.5 at $\overline{z}=4,5,7$, and 10. It can be observed that an excellent agreement is found. Only PIV measurements for a radial distance greater than 0.4 have more dispersion due to the presence of small-magnitude velocities (close to zero) as the vortex core grows radially. Errorbars in these plots represent numerically the standard deviation taking into account one hundred measurements in the azimuthal coordinate θ. However, in the case of the experimental measurements, the dispersion also comes not only from the average in θ but also from the standard deviation of four different experiments. One can observe

(a) z=4c

(b) z=5c

(c) z=7c

(d) z=10c
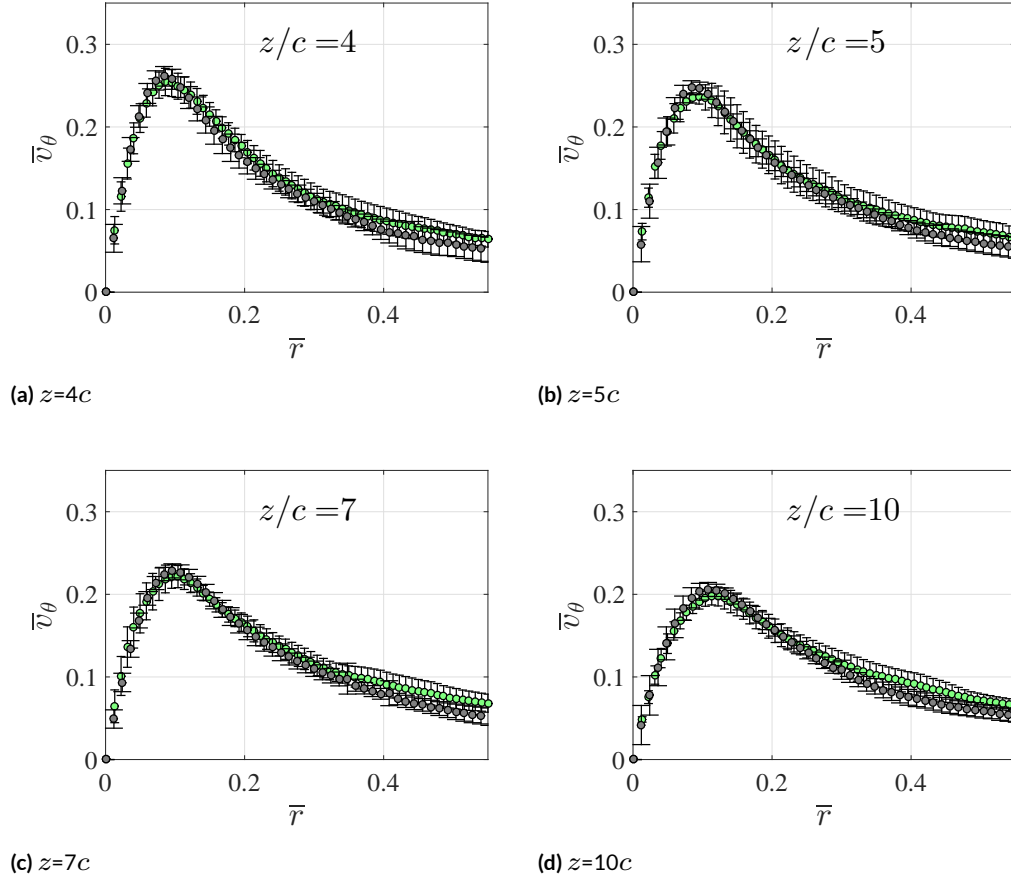
Figure 4.5: Experimental and numerical comparison from DNS (grey) and experiments (green) for azimuthal velocity at $\overline{z} = z/c$=4 (a), $\overline{z}$=5 (b), $\overline{z}$=7 (C) and $\overline{z}$=10 (d), respectively.

how the maximum azimuthal velocity decreases as the trailing vortex moves downstream. Besides, the radial location where the maximum takes place increases its value as a result of the vortex core diffusion. This fact confirms our proper experimental procedure again.

4.4.2 THEORETICAL MODELS: PARAMETERS AS FUNCTION OF THE AXIAL COORDINATE
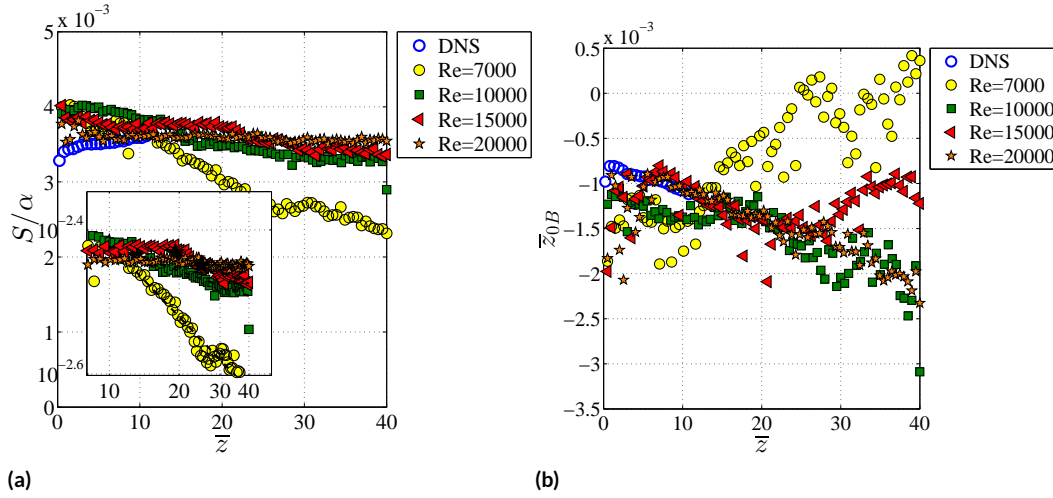
Figure 4.6: Batchelor's model: experimental and numerical evolution of parameters S (a) and $\overline{z}_{OB}$ (b) as function of Reynolds number.

Our main goal is to estimate the theoretical parameters of Batchelor's model (S, $\overline{z}_{OB}$) and Moore & Saffman's model (b, n, $\overline{z}_{OMS}$) as function of Re_c. To that end, we start with Batchelor's model and the dependence of the best fitting with DNS and experiments as a function of the streamwise direction. Therefore, we depict how S and $\overline{z}_{OB}$ evolve in the streamwise direction ($\overline{z}$) depending on the Reynolds number considered in Figure 4.6. In this plot, alongside the theoretical parameters obtained from DNS up to $\overline{z}$=11, we also show those parameters fitted by experimental data up to $\overline{z}$=40. A reasonably good agreement was found again at Re_c=7×10³. We observe that the vortex strength presents in Figure 4.6a two different regions which strongly depend on Re_c in the range considered. The inset shows the same plot but in a logarithmic scale in both axes to better understand the presence of two regions: the first region regarding the roll-up process where the vortex strength S remains almost constant and the second where S decreases with $\overline{z}$ due to the vortex diffusion. In general, the length of the first region increases with Re_c. For instance, it is shown that the parameter S remains almost constant for the largest Reynolds numbers considered, Re_c=20×10³. However, for the smallest Reynolds number, Re_c=7×10³, the second region begins at $\overline{z}$ ≈10. These two regions should be considered in future works to solve the open question related to the definition of near- and far-field of the trailing vortex [see Giuni, 2013]. Authors do believe that this distinction between the roll-up process (near-field) and the vortex decay (far-field) plus the well-defined associated structure of the wingtip vortex (mild-field) must be offered in terms of theoretical parameters following realistic models and the Reynolds number considered, but not in those of subjective perspectives. In other words, the concepts near-, mid-, and far-field should be defined using the Reynolds numbers dependent Batchelor's or Moore & Saffman's models accordingly.

On the other hand, the local virtual origin, $\overline{z}_{OB}$, is weakly influenced by Re_c, as shown in Figure 4.6b. Experimentally, we also observe that the strength of the vortex decreases axially downstream at Re_c=7×10³ in the second region, so the initial negative virtual origin increases even to positive values. This compensation between these two parameters stems from the Batchelor's model formulation described in equation (4.15) when a constant circulation is required to enhance a constant lift coefficient.

We also consider the computation of theoretical parameters regarding Moore & Saffman's model. We depict the results in Figure 4.7, where we show the evolution with the axial coordinate for b (a), n (b) and $\overline{z}_{OMS}$ (c). A good comparison between experiments and DNS data is found again for Re_c=7×10³. The
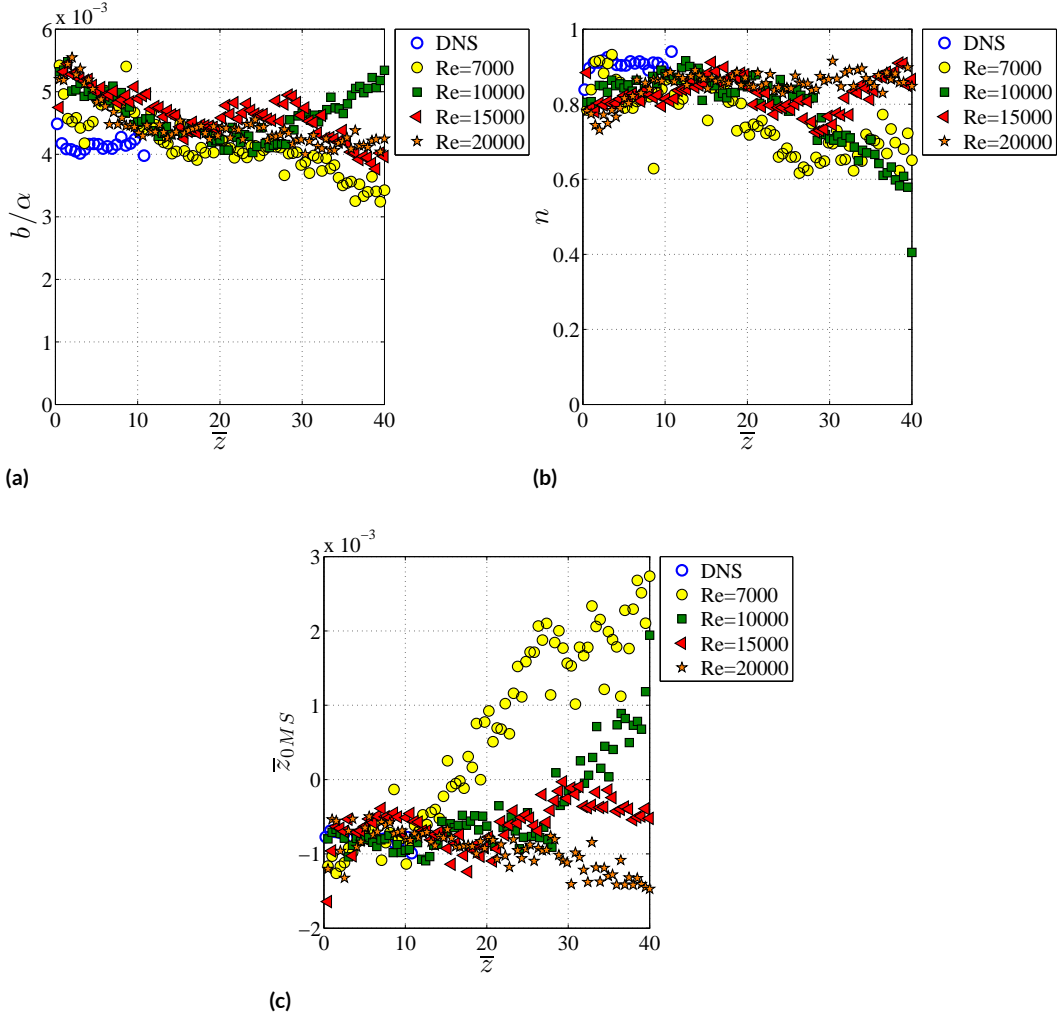
(a)

(b)

(c)

Figure 4.7: Moore & Saffman's model: experimental and numerical axial evolution of parameters b (a) and n (b), and $\overline{z}_{OMS}$ (c) for different Reynolds numbers.

wingtip vortex is always wake-like since n is greater than 0.44 for all the cases studied up to 40 chords. Besides, it is observed that there is a change in the sign of $\overline{z}_{OMS}$ due to the vortex decay for Re_c=7×10^3 and 10×10^3, see parameter n. In the case of Moore & Saffman's model, equation (4.17) explains again why the parameter n decreases as $\overline{z}_{OMS}$ increases.

4.4.3 THEORETICAL MODELS: PARAMETERS AS FUNCTION OF REYNOLDS NUMBER

In the last section, we performed the curve fitting at each axial location of theoretical parameters from experiments and DNS. In this section, we present in Figures 4.8 and 4.9 the dependence of these parameters for Batchelor's and Moore & Saffman's models as a function of Re_c. We depict the average values of the theoretical parameters obtained from DNS and experiments, and only their dispersion taking into account the spatial range up to $\overline{z}$=40 of experimental measurements because the fluctuations of theoretical parameters determined by DNS from $\overline{z}$=0 to 11 are tiny. Also, the reader must remember that DNS results correspond to $Re_c \leq$ 7×10^3 while experimental results are shown for $Re_c \geq$ 7×10^3.

We first focus on Figure 4.8 where the main characteristic of Batchelor's model is presented. We plot in Figure 4.8 not only the data from this work but also from those experimental measurements of three references which use a NACA0012 airfoil: (i) del Pino et al. [2011b] for α=6, 9, and 12°, Re_c= 20×10^3 and 40×10^3 up to $\overline{z}$=16 (PoF2010), Serrano-Aguilera et al. [2016] for α=10° and Re_c= 33.3×10^3 and 100×10^3
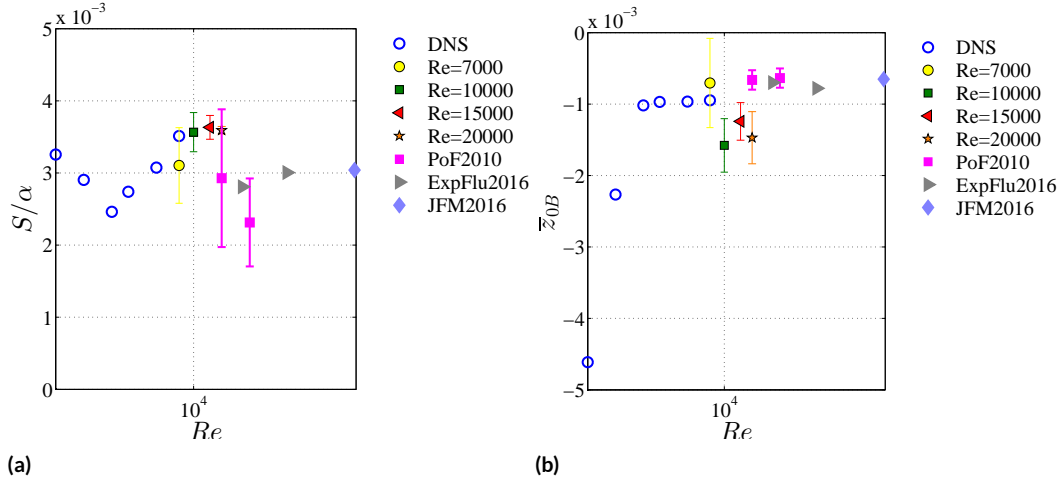
Figure 4.8: Batchelor's model: experimental and numerical evolution of parameters S (a) and $\overline{z}_{OB}$ (b) as function of Reynolds number.

up to $\overline{z}=5$ (ExpFlu2016), and Edstrand et al. [2016] for $\alpha=5^o$ and $Re_c=530\times10^3$ at $\overline{z}=5$ (JFM2016). In this last reference, they reported data using Batchelor's model and 3DPIV. Their results were $\kappa=0.0152$ and $\delta=0.0514$ which correspond to $S/\alpha=3.04\times10^{-3}$ and $\overline{z}_{OB}=-6.51\times10^{-4}$. Recall that only one location of $\overline{z}=5$ is required in this reference, thus confirming that the first two regions described in Figure 4.6a are too small. The same consideration must be given describing the reference EXPFlu2016, in which experimental data is carried out from $\overline{z}=0$ to $\overline{z}=5$. This fact confirms that the near-field or the far-field are concepts that strongly depend on Re_c, as it was commented above. Finally, theoretical parameters from PoF2010 increase the scatter around the average value about 40% experimentally due to the three angles of attack considered and the limitation in the numbers of chords considered in that work ($\overline{z}$ lower than 16).

The results in Figure 4.8 confirm that there are two critical values of the Reynolds number at $Re_{C1}\approx1.3\times10^3$ and $Re_{C2}\approx10$-20×10^3. The main characteristic to detect these two critical Reynolds number is based on the following aspects: the vortex strength S/α versus Re_c changes its trend, increasing instead of decreasing its value, and also the virtual origin $\overline{z}_{OB}$ remains constant when it evolves with Re_c.

In Figures 4.8a and 4.8b we observe that there is a first change in the trend of S/α and $\overline{z}_{OB}$, respectively. The explanation of this first critical Reynolds number at $Re_c=Re_{C1}$ is the onset of instabilities in the vortex wake, as it is shown numerically in Figure 4.10. The vorticity surface from DNS data shows that the wake remains stable at $Re_c=0.67\times10^3$ (a), but becomes unstable at 1.33×10^3 (b) where the snapshot shows fluctuations in the trailing vortex tube. At this point, the flow becomes time-dependent. The exact transition is calculated to be around $Re_c=1.19\times10^3$, which is reasonably near to the value $Re_c=0.8\times10^3$ that can be obtained from the extrapolation of the results shown in Taira & Colonius [2009b] for a flat plate with the same aspect ratio and angle of attack considered in our study. In addition, and for the sake of clarity, a turbulent snapshot is depicted in (c) for $Re_c=7\times10^3$ to observe the difference qualitatively in the vortex wake at the largest Reynolds numbers considered numerically. Focusing again on $Re_c=Re_{C1}$, Suzuki et al. [2009a,b] found some discrepancies with those results given by Hoarau et al. [2003] who performed 2D-DNS at $Re_c\approx1\times10^3$. This discrepancy was characterised by the presence of large fluctuations in the experimental measurements. This value of the Reynolds number $Re_c\approx1\times10^3$ is very close to the onset of 3D instabilities in our case. Therefore, the production of the unsteady flow behind the airfoil beyond $Re_c=Re_{C1}$ has the following effect: the global behaviour of the vortex strength increases its value with Re_c instead of decreasing it due to the pulsating injection of vorticity up to the second critical Reynolds number $Re_c=Re_{C2}$.
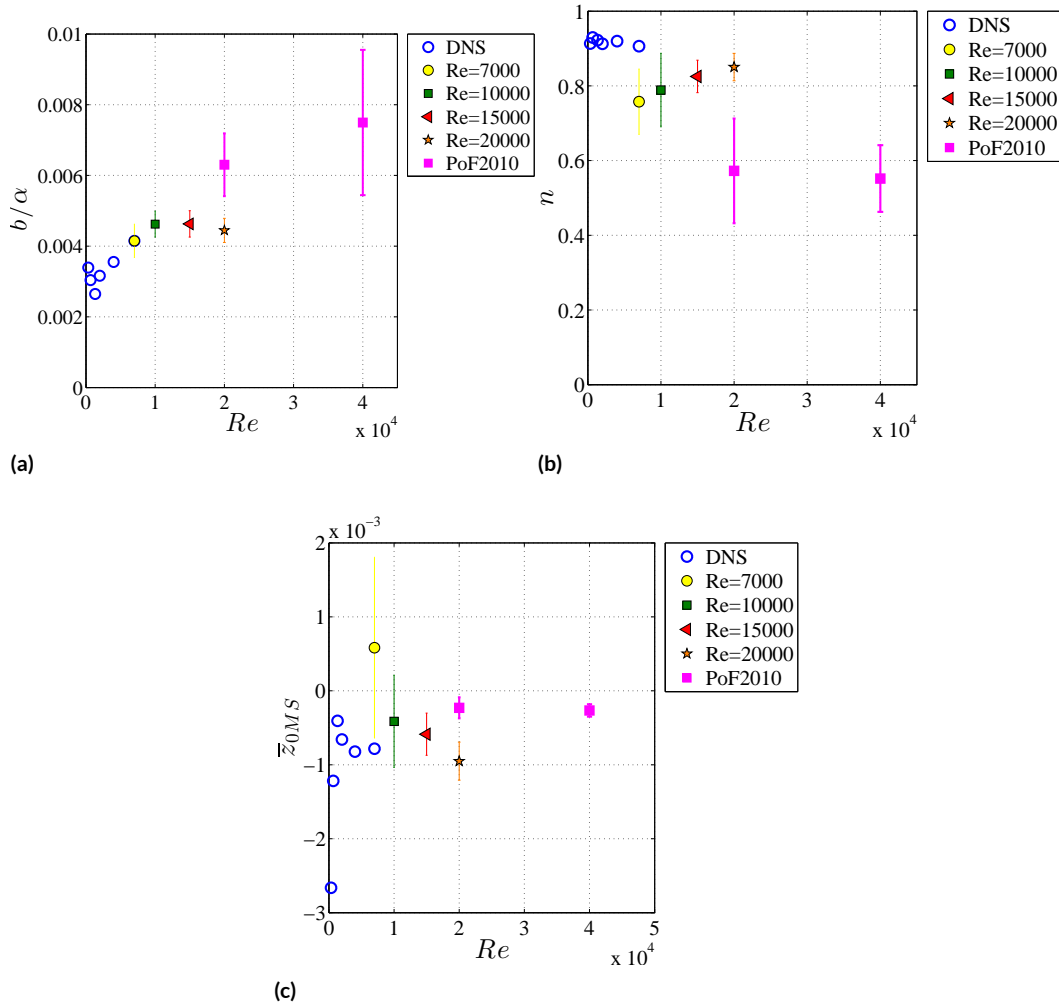
(a)

(b)

(c)

Figure 4.9: Moore & Saffman's model: experimental and numerical evolution of parameters b (a) and n (b), and $\overline{z}_{OMS}$ (c) as function of Reynolds number.

On the other hand, we observe in Figure 4.8 a second critical Reynolds number at $Re_c = Re_{C2}$ greater than 10-20×10³. At this point, the theoretical parameters appear to become constant experimentally. This second threshold should be related to airflow near the airfoil surface from the laminar boundary layer to the turbulent flow in the leading and trailing edges, respectively. For this reason, a plausible explanation might be the evolutionary process that results in a smooth transition to achieve a complete separation of the laminar bubble. When this process is already finished at Reynolds number greater than Re_c=10-20×10³, approximately, there is no reattachment of the turbulent wake to the wing surface, and the bubble stays open. Consequently, the main value of the vortex strength should remain constant, as it happens in the three references introduced in Figure 4.8a. A second possible reason to this second threshold could be the saturation of the instabilities presented in Figure 4.10b after their nonlinear growth [Viola et al., 2016]. Finally, authors would like to point out that the precision shown around Re_{C2} in Figure 4.8a does not allow us to confirm a small descent in the vortex strength beyond this second critical point.

The observations made in Batchelor's model can be extended to the Moore & Saffman's model, as shown in Figure 4.9. Only the reference PoF2010 can be included in this plot (Re_c=20 and 40×10³). It is clear that less attention has been paid to this model in the State of Art to fit the theoretical parameters and more effort must be done in further research. The evolution of theoretical parameters b/α (a), n (b) and $\overline{z}_{OMS}$ (c) with Re_c confirms the change in the trend at $Re_c = Re_{C1}$ numerically, with n being the only variation
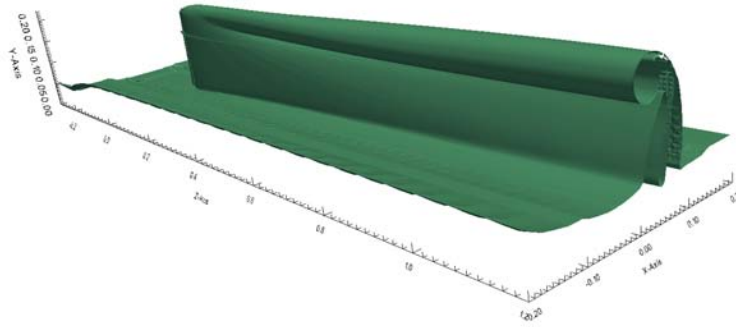
(a)
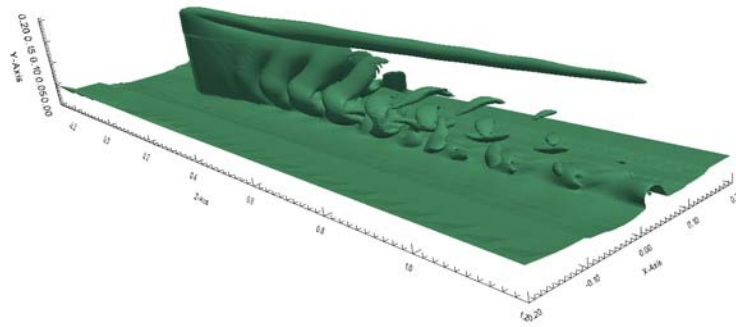
(b)

Figure 4.10: DNS results for stable wake (a), the unstable wake (b) and the turbulent vortex wake (c) at Re_c=0.67, 1.33 and 7×10^3, respectively.
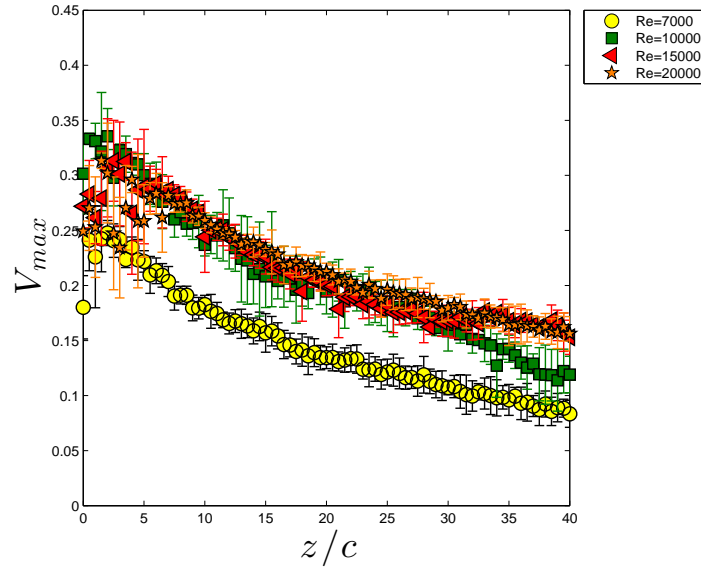
Figure 4.11: Experimental results for the maximum azimuthal velocity as function of z.

and it is too small to detect this first critical point. In the case of the second transition at $Re_c = Re_{C2}$, only a large decrease in the exponent of the vortex decay n has been observed, plus associated increment in b/α. In the case of the parameter $\overline{z}_{OMS}$, it seems to be constant for Re_c greater than Re_{C2}.

Finally, we represent in Figure 4.11 the nondimensional maximum azimuthal velocity V_{max} as function of $\overline{z}$. It is worth mentioning that V_{max} which is linked to the vortex strength (as the parameter S does) increases with Re_c. However, V_{max} tends to saturate as the Reynolds number is near $Re_c = 10 \times 10^3$ thus providing a plausible explanation of the presence of the second critical Reynolds number Re_{C2} shown in Figure 4.8. In other words, the increment of Re has a weak influence on the vortex strength and this fact should be associated with a saturation in the lift coefficient. This aerodynamic study to characterise the NACA0012 airfoil might also be carried out in further research.

4.5 CONCLUSIONS

In this research we have been focusing on DNS and 2D-PIV measurements using a NACA0012 airfoil. The major finding is the dependence of theoretical parameters which arise from Batchelor's and Moore & Saffman's models with the Reynolds number. As mentioned in the introduction section, there is a lack of information for wingtip vortices regarding this topic at ultra-low, low and moderate Reynolds numbers for aeronautical applications. A huge number of numerical and experimental studies have been carried out, but no connection with the Reynolds number has been established previously. We show in this experimental and numerical work a detailed analysis of the trailing vortex behind a NACA0012 airfoil for one angle of attack. Ultra-low and low Reynolds numbers ranging from $Re_c=0.3\times10^3$ to $Re_c=20\times10^3$ have been considered. Five theoretical parameters are obtained from computational and experimental results: two corresponding to Batchelor's model and three regarding Moore & Saffman's model.

To shed some new light on this dependence, we carried out direct numerical simulations (DNS) and experiments. An excellent agreement was found at $Re_c=7\times10^3$ in the near-field up to 10 chords. After this comparison, we gave information at lower Reynolds numbers using DNS due to the extreme difficulties in the experimental realisation of measurements in our facility. Besides, higher Reynolds numbers could be explored in the near- and far-field experimentally because DNS is quite time-consuming. Firstly, our numerical results for Reynolds numbers lower than $Re_c=7\times10^3$ show a significant change of trend in theoretical parameters regarding the vortex strength at a first critical Reynolds number $Re_{C1}\approx1.3\times10^3$, where the onset of unsteadiness in the flow were present numerically in the vortex wake. Secondly, the experimental results show a new change in the trend of theoretical parameters as they evolve with Re_c at $Re_{C2}=10\text{-}20\times10^3$, finding two possible explanations: the smooth transition of the separation bubble or the saturation of the nonlinear instabilities that grows from $Re_c=Re_{C1}$. In general, theoretical parameters remain constant at the largest Re_c considered for Batchelor's model. This fact has been confirmed using the fitting of theoretical parameters from several experimental data of different authors. In the case of Moore & Safmann's model, the parameter n gives us information of the vortex decay. We showed that this value is greater than 0.44, so the vortex is always wake-like. Besides, this parameter seems to be relevant to detect the second critical Reynolds number.

All the information given in this work is of great value for performing future stability analysis in the range of $Re_c=1\text{-}1.5\times10^3$ to detect the nature of the unsteady flow, and further research regarding the specific criterium to detect more precisely the second critical Reynolds number employing DNS.

5

The influence of low blowing ratio continuous jets on wingtip vortex characteristics

In this chapter, we used the same experimental rig and the post-processing procedure as in Chapter 4. The purpose is to provide a good understanding of the effect of continuous blowing from near the tip while also examine the effect on several parameters. Therefore, the results will be presented in contrast with the reference case, without blowing. The model used, NACA0012, has been machined with two holes which are separated $20mm$ and $0.5mm$ in diameter in a way outside all along its length its length to provide spanwise direction blowing. See figure 5.1. Due to the difference between airfoil section and blowing holes section, this kind of continuous blowing is denominated *low aspect ratio blowing* in contrast to Tavella et al. [1986, 1988]; Margaris [2006]; Margaris & Gursul [2009] who used a slot. (See, e.g, fig 1.19). To carry out the continuous blowing we used one syringe pump (Veterinarian Pump) model *KdScientific 120* with differents syringes depending on the kind of experiment. This kind of pump was chosen because it supplies a constant flow without a flowmeter.
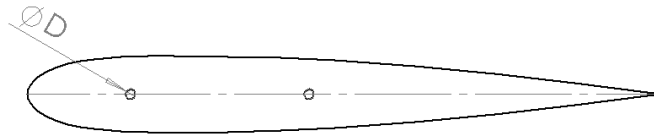
Figure 5.1: Naca0012 Scheme.

In flow control studies by continuous blowing injection, we must define the jet coefficient as:

$$R_{jet} = \frac{W_{jet}}{W_\infty} \tag{5.1}$$

where W_{jet} corresponds to the injection velocity and W_∞ to the airfoil movement. That allows the comparison of different studies by estimating the flow of the model under investigation itself. We carried out various experiments to different R_{jet} values and different Reynolds number. For each R and Reynolds number, four experiments were conducted, and they were processed in the same way as in section 4. The
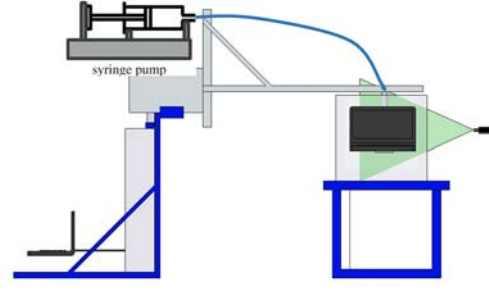
(a)   (b)

Figure 5.2: Syringe pump setup.

cases studied were R_{jet} =0.75,1,2 in order to $Re_=$7,15 and 20×10³. We used a syringe with 20ml volume for Re_c =7×10³ cases and another one with 60ml volume for all other Reynold cases. All measurements were conducted at an angle of attack of α =9°.

The vortex property analysis was performed at the furthest downstream plane and included circulation and tangential velocity, as well as the fitting of theoretical parameters. Unlike the chapter 4, we have only studied up to chord=20 because of the volume limitations of the syringe. On the other hand, we have only carried out experiments up to R_{jet} =2 due to the constraints of the pump (we used the biggest syringe permitted by the pump in each case).

5.1 RESULTS

In this section, we analyse the results obtained from the experimental measurements of continuous jets and the main characteristics of the formation and development of the wingtip vortex. Each experiment for three different Reynolds numbers was performed four times, and the whole arrangement was synchronised to achieve the same flow field at each axial position z. Afterward, 2D PIV technique was applied to obtain the velocity field (v_x^*, v_y^*) for different axial distances from the wing. Once the velocity components v_x^* and v_y^* were computed, the axial vorticity ω^* was derived from the post-processing step following the indications are given in Raffel et al. [2007]. To that end, the vortex core was determined by obtaining the position of the maximum vorticity [see Igarashi et al., 2010; Cohn & Koochesfahani, 2000]. We have checked that the centre computed by using the maximum vorticity was quite similar to the vortex core position of the minimum presented in the 2D velocity field.

Once the results of the vorticity and the vortex core were obtained, we projected the results on a polar coordinate system,this procedure being similar to the one reported by Heyes et al. [2004]. Therefore, we computed the radial, $V_r^*(z^*)$, and azimuthal velocity $V_\theta^*(z^*)$ components. Also, we computed the value of the maximum azimuthal velocity $V_{\theta max}^*(z^*)$ and the radial position at which this value was located, so-called R_{max}. Other two parameters that we obtained were the maximum vorticity $\omega_{max}^*(z^*)$, which was located in the axis (r=0), and also the circulation at each axial distance from the wind, $\Gamma^*(z^*)$, by integrating the vorticity field at each plane (r^*, θ).

We consider the characteristic length, time and velocity c, c/W_∞ and W_∞, respectively, to render the non-dimensional variables $V_{\theta max}(z)$, $R_{max}(z)$, $\omega_{max}(z)$, and $\Gamma(z)$.

We show in Figures 5.3-5.5 all the results considered above. In these figures, we represent the mean value
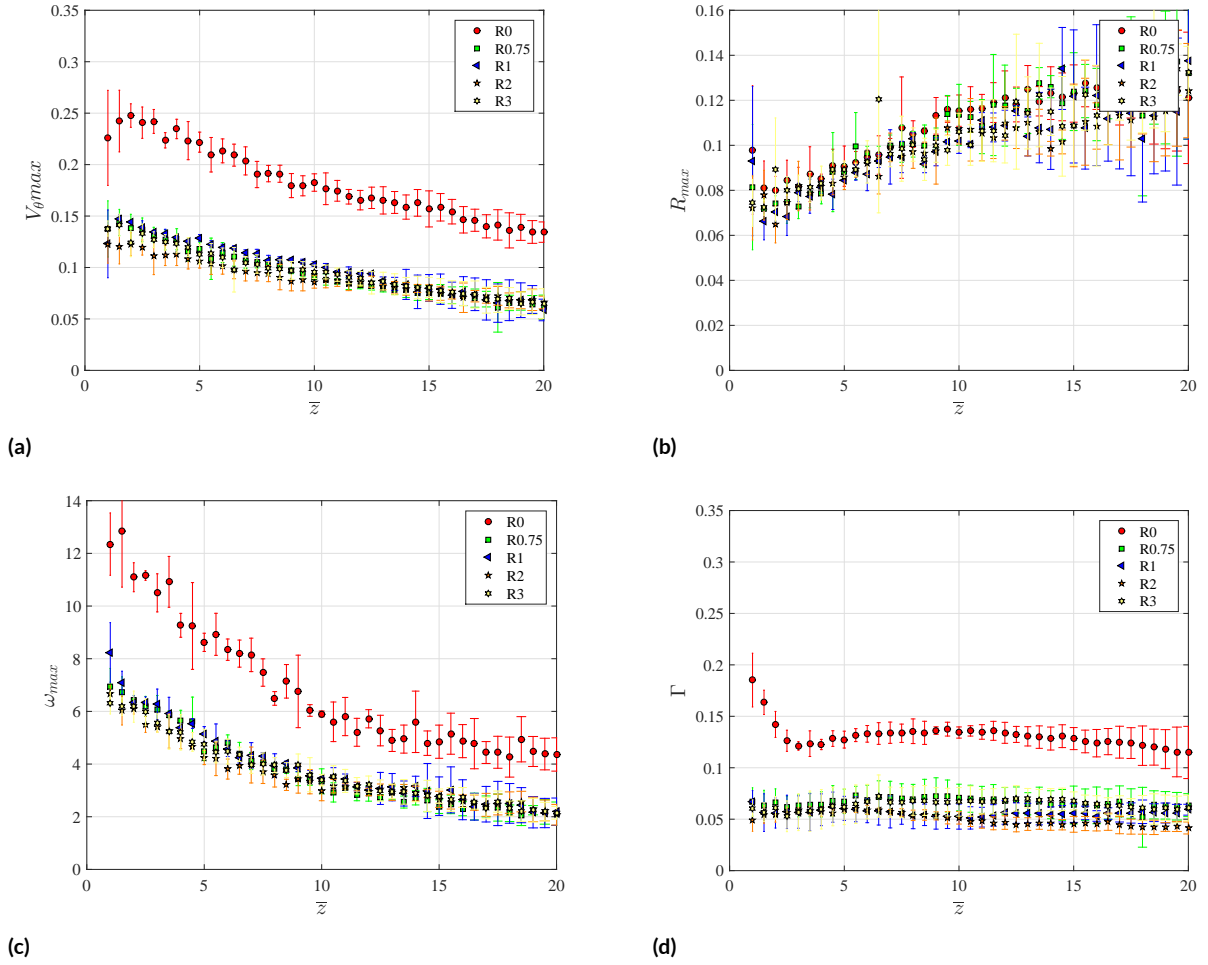
Figure 5.3: Results obtained for $Re = 7 \times 10^3$ and different blowing ratios R_{jet}. $V_{\theta\,max}$ (a), r_{max} (b), ω_{max} (c) and Γ(d).

of $V_{\theta max}$ (a), R_{max} (b), ω_{max} (c) and Γ (d) at each axial position and the errorbars represent the standard deviation for four different experiments at a constant value of the Reynolds number. Figure 5.3 shows the results obtained for $Re=7\times10^3$ and different blowing ratios, R_{jet}. We observe that there is a considerable variation in the structure of the flow for the lowest Reynolds number considered depending on R_{jet} in Figures 5.3 (a), (c) and (d). Hence, maximum azimuthal velocity, the maximum vorticity, and the circulation are strongly influenced by the blowing ratio at the wingtip. In general, these magnitudes decrease with z, but only a small increment in R_{jet} makes the vortex strength to decay drastically. Conversely, the position R_{max}, at which the maximum azimuthal velocity is achieved, does not change with the blowing ratio R_{jet}.

The results for the cases $Re=15\times10^3$ and $Re=20\times10^3$ are depicted in Figures 5.4 and 5.5, respectively. In these cases, the effect of the continuous blowing has a weak influence on the flow properties. Figures (d) show that the main effect is an overall reduction of the circulation Γ for any value of R_{jet} up to $z \approx 7$ for both $Re=15\times10^3$ and $Re=20\times10^3$.

(a)

(b)

(c)

(d)

Figure 5.4: Results obtained for $Re_c = 15 \times 10^3$ and different blowing ratios R_{jet}. $V_{\theta\,max}$ (a), r_{max} (b), ω_{max} (c) and Γ (d).

(a)

(b)
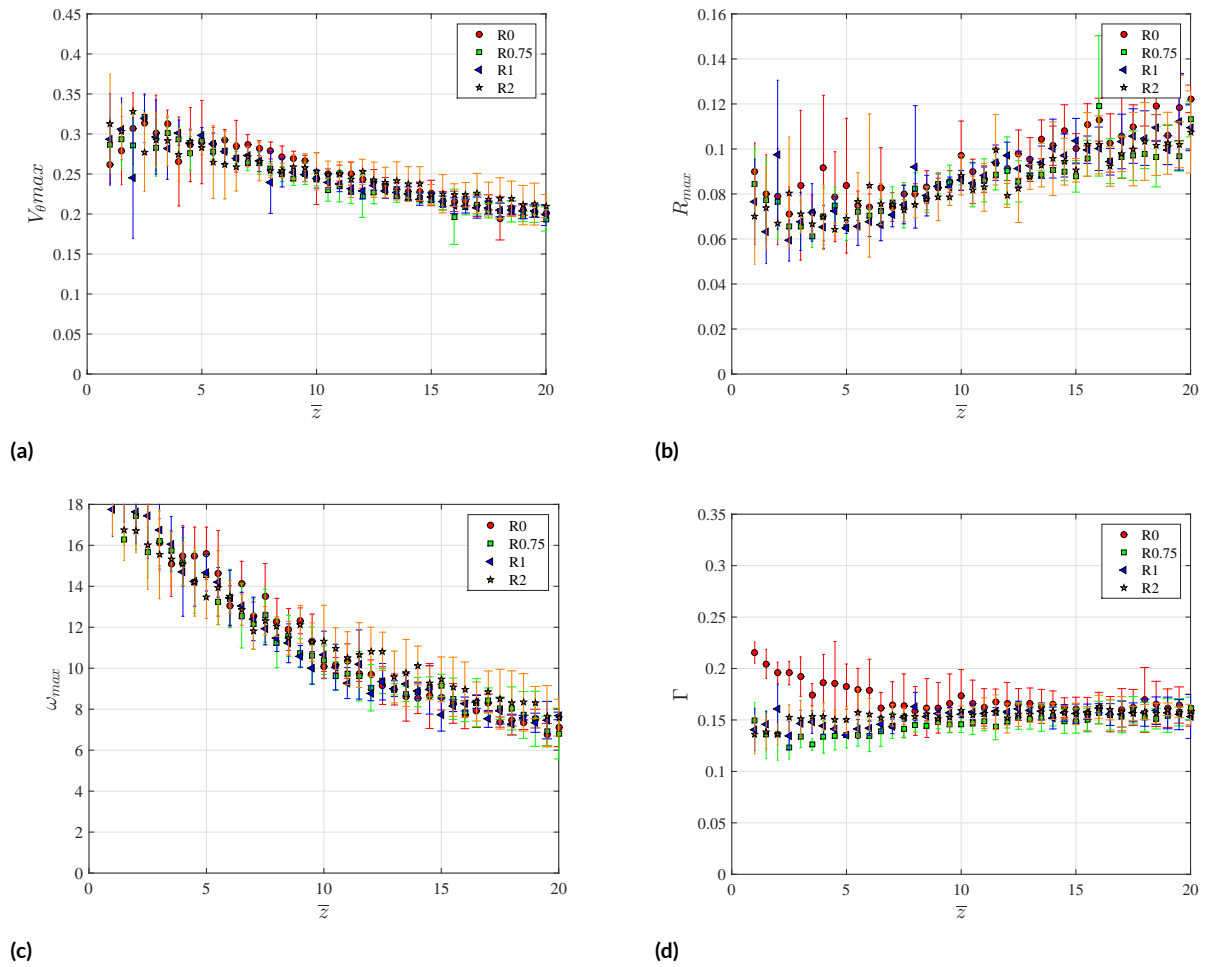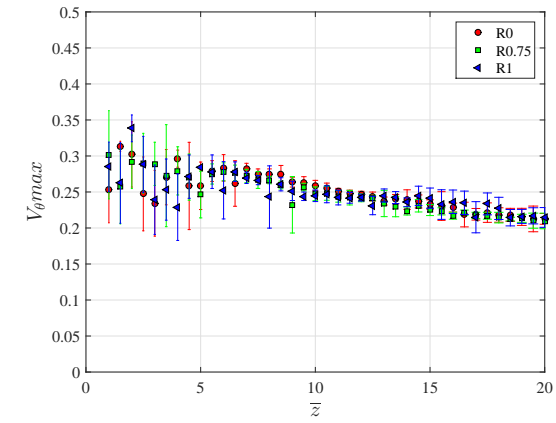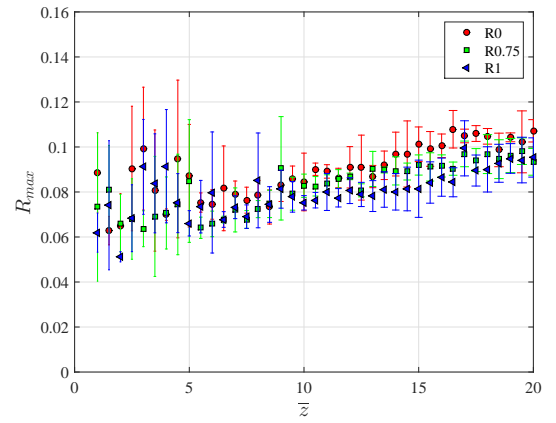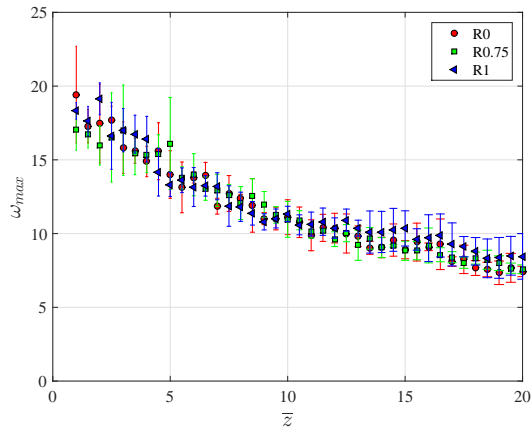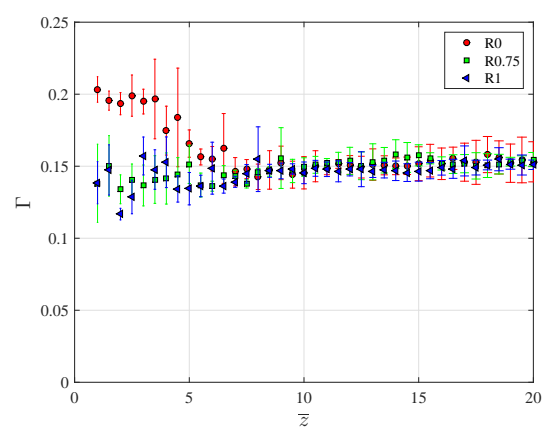
(c)

(d)

Figure 5.5: Results obtained for $Re_c = 20 \times 10^3$ and different blowing ratios R_{jet}. $V_{\theta\,max}$ (a), r_{max} (b), ω_{max} (c) and Γ (d).

5.2   Discussion

The continuous jet affects at any value of R_{jet} at the lowest Re considered. However, for Reynolds numbers equal to or greater than 15×10^3, the continuous jet affects the near-field for distances lower than 7 chords from the wing. The reason for this different behaviour is explained by the ability of the jet to break the vorticity sheet and to create a counter-rotating vortex or co-rotating vortex at low or high values of Re, respectively. This is observed in the schematic presented in Figures 5.6 (a) and (b).

(a)

(b)
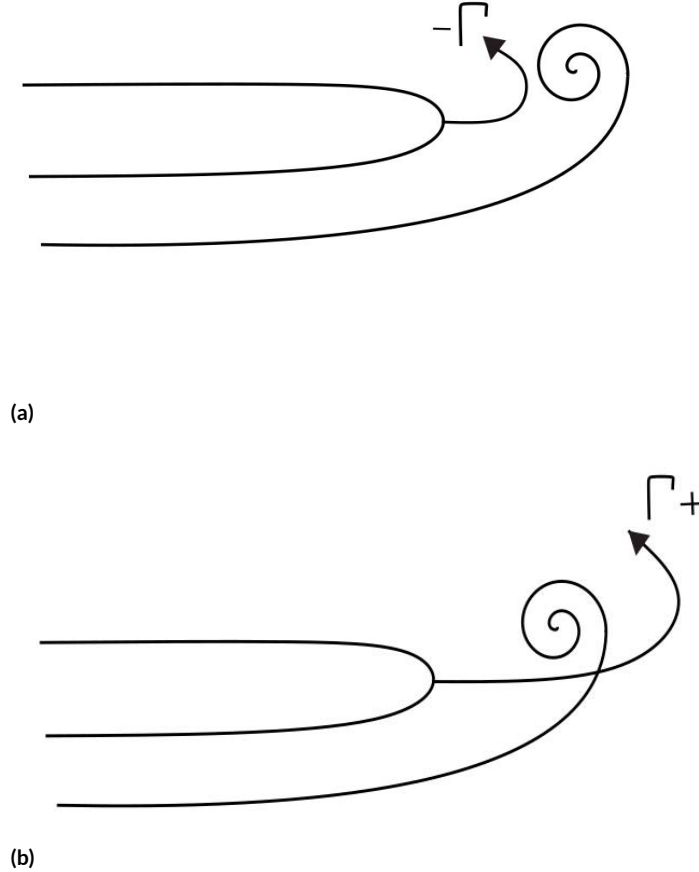
Figure 5.6: Schematic of the continuous jet at low (a) or high (b) Reynolds number.

For the lowest Reynolds number, $Re=7\times10^3$, we plot in Figure 5.7 3D isocontours for $\omega = 3$ in red and $\omega = -3$ in blue for different blowing ratios R_{jet}. In the case of without blowing, $R_{jet} = 0$ (a), one counter-rotating vortex is created behind the wing. The vortex presents a very linear shape and its intensity decays smoothly with the axial distance z due to viscous diffusion. For the middle blowing ratios, R_{jet} =0.75 (b) and R_{jet} =1 (c), the jet flowing from the tip of the wing counteracts the main vortex, reducing its strength. For highest blowing rate R_{jet} =2 (d) the reduction is evident, probably because the jet flowing from the wingtip is able to break the vorticity sheet so that the continuous jet does not act on the inner side of the wingtip vortex, which the reduction of strength being less evident.

On the other hand, for higher Reynolds numbers, we show above that the effect of increasing the blowing ratio is feeble. In Figures 5.8 we represent again 3D isocontours of the vorticity in red for ω =4 and in blue for ω =-4, for the seven chords near the wing where the region at which the effect of the blowing is evident. We observe that the rolling process produces, in this case, two different counter-rotating vortices near the wing, as in the $Re=7\times10^3$ case. The blowing jet does not change the main vortex but reduces the strength of the blue vortex strongly for $Re=15\times10^3$. Conversely, the blowing produces a new co-rotating vortex for $Re=20\times10^3$.
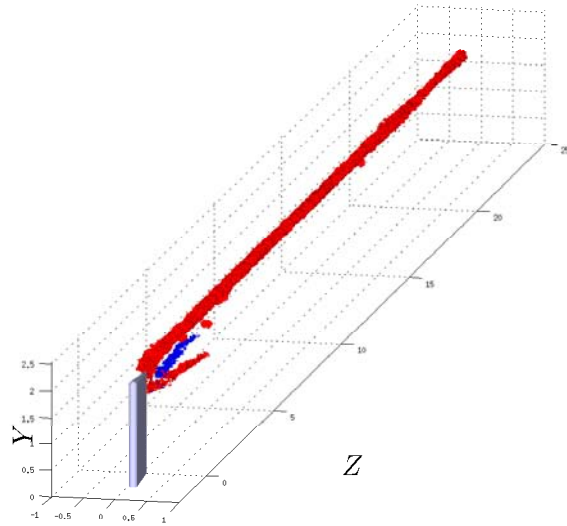
(a) R_{jet} =0
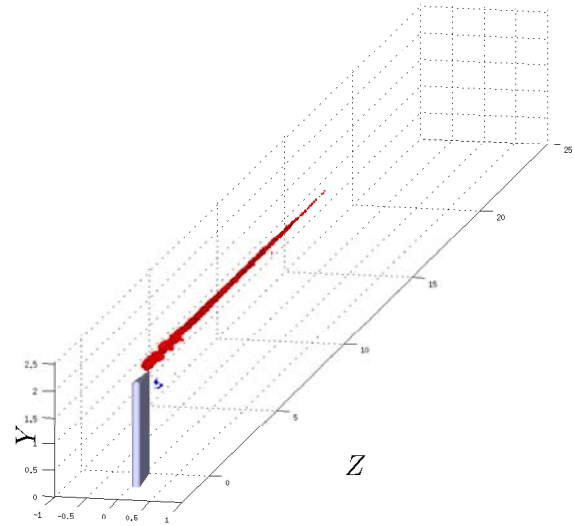
(b) R_{jet} =0.75
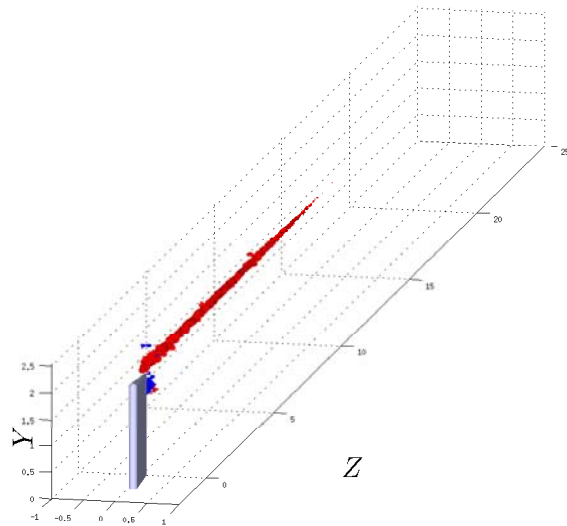
(c) R_{jet} =1
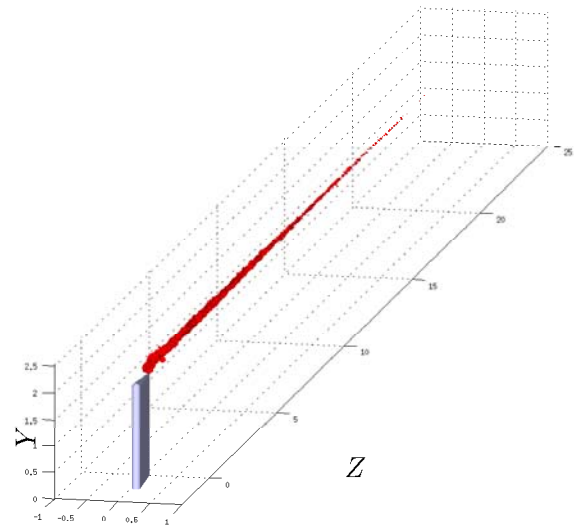
(d) R_{jet} =2

Figure 5.7: 3D vortex representation for Re=7×10^3 and four blowing ratios $R_{jet} = 0$ (a), 0.75 (b), 1, (c) and 2 (d). In red/blue are represented the 3D isocontour of vorticity for $\omega = 3$ and $\omega = -3$ respectively.
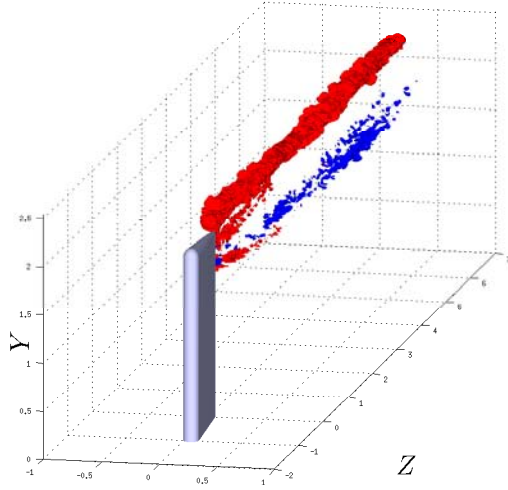
(a) Re_c =15×10^3-R_{jet} =0
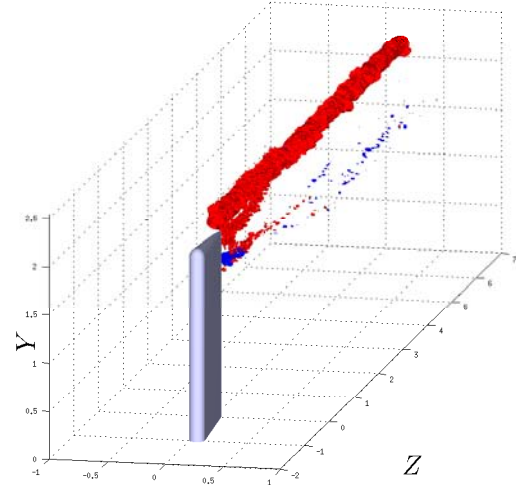
(b) Re_c =15×10^3-R_{jet} =1
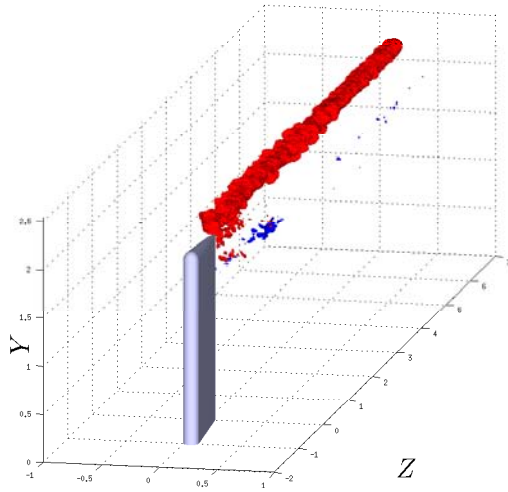
(c) Re_c =20×10^3-R_{jet} =0
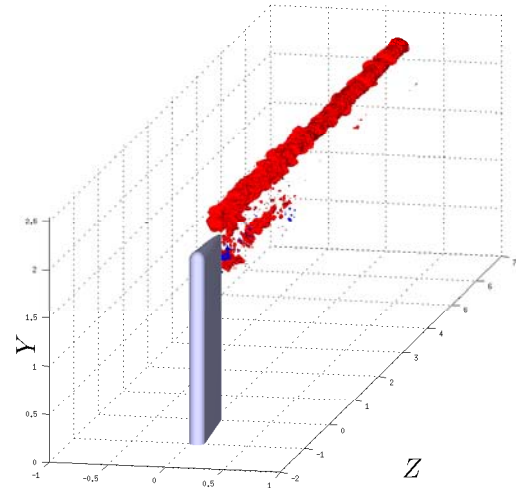
(d) Re_c =20×10^3-R_{jet} =1

Figure 5.8: 3D vortex representation at Re=15×10^3 (a)-(b) and 20×10^3 (c)-(d). In red/blue are represented the 3D isocontour of vorticity for $\omega = 4$ and $\omega = -4$ respectively.

5.3   Conclusions

In this chapter, we have studied the influence of low blowing ratio continuous jets on wingtip vortex characteristics, including the formation and development of the wingtip vortex with the axial distance. We have measured for three different Reynolds numbers Re=7, 15, and 20×10^3, and different blowing ratios R_{jet}. We show that for lowest Reynolds numbers, the effect of the continuous jet for middle blowing ratios is to reduce the wingtip vortex strength dramatically. For higher Reynolds numbers, the effect is observable only in the region near the wing (distances up to 7 chords), and it only affects to the secondary vortex that appears in the rolling process. The reason for this different effect for different cases is related to the ability of the perpendicular jet to break the vorticity sheet. If the jet is not able to break it, the effect is to add some small negative circulation to the main vortex, and the overall effect is to decrease the vortex strength strongly.

6

Conclusions and recommendations for future work

This chapter summarises the main findings of the present research regarding novel experimental techniques applied to wingtip vortices plus their associated characterisation. Also, we discuss some results from Direct Numerical Simulations and 2D Particle Image Velocimetry (PIV) measurements together with their implications. Finally, we make some recommendations for future work which correspond to theoretical, numerical and experimental topics.

6.1 Conclusions

This thesis has as its main objective to present a study of the wake dynamics of the flow behind wings. In particular, we focus on the trailing vortex behind a NACA0012 airfoil in the from the near- to the far-field. To that end, we have taken into account different numerical, experimental and theoretical considerations related to: (i) the shape of the wingtip vortex using smoke visualizations; (ii) the DNS and 2DPIV measurements as the trailing vortex evolves downstream for several Reynolds numbers; and (iii) active control performed by a continuous jet in the spanwise direction.

Regarding the description of the experimental work given in the second chapter, two large facilities have been used and set up to carry out tests using smoke visualisations and 2DPIV measurements from which one can define the structure of the trailing vortex. For instance, in the first of two experiments described in chapter three using a wind tunnel we report the exact value of theoretical parameters such as the vortex strength and the virtual origin of the coordinate system using a simple experimental technique. For this purpose, we record images from smoke visualisations of a laser sheet plane, which highlight the smoke coming from a thin wire. Only a digital camera is required. The post-processing of instantaneous images allows successful quantification of the shape of the wingtip vortex at different planes in the near-field. These results in combination with differential equations that describe the axial evolution of the trajectory theoretically give quantitative information of two parameters of Batchelor's model during the roll-up process up to five chords. This experimental procedure was found to be a simple tool for the validation of previous PIV measurements and future numerical simulations. It should also be noted that accurate simulations of turbulent flows with intense rotation from the trailing vortices always requires experimental validation, so the novel

experimental technique described in chapter three is a good option.

We have also focused on DNS and 2DPIV measurements in the fourth chapter using a NACA0012 air-foil. In this case, a towing tank has been used. The major finding of this chapter is the relation of theoretical parameters of Batchelor's and Morre & Saffman's models with the Reynolds numbers. As it was mentioned in the introduction section, there is a lack of information about the dependence on theoretical models for wingtip vortices and Reynolds numbers at ultra-low, low and moderate Reynolds numbers for aeronautical applications. A big amount of numerical and experimental studies have been carried out, but no connection with the Reynolds numbers (Re_c) has been established accurately. To shed some new light into this dependence, we performed direct numerical simulations (DNS) and experiments. An excellent agreement was found at $Re_c = 7 \times 10^3$ and $Re_c = 4 \times 10^3$ in the near-field. After this comparison, we gave information at lower Reynolds numbers using only with DNS due to the extreme difficulties of carrying out experiments in our facility. Besides, it was not possible to explore higher Reynolds numbers in the near- and far-field experimentally because to run DNS is quite time-consuming. On the one hand, our numerical results up to $Re_c = 7 \times 10^3$ show a significant change of trend in theoretical parameters regarding the vortex strength at $Re_c \approx 1.3 \times 10^3$, where the onset of unsteadiness in the flow was present in the near-field (up to eleven chords). On the other hand, the experimental results in the far-field show a saturation in theoretical parameters at $Re_c = 10\text{-}15 \times 10^3$, being these values in agreement with other authors that reported experimental data at $Re_c = 530 \times 10^3$. Finally, the parameter n that gives us information of the vortex decay in Morre & Safmann's model. We showed that this value is greater than 0.44, so the vortex is always wake-like. Consequently, all the information given in this chapter is of great value to perform:

1. Future stability analysis in the range of $Re_c = 1\text{-}1.5 \times 10^3$ to detect the nature of the unstable flow and,

2. to establish the minimum Reynolds number at which simulations must be carried out to neglect viscous effects in the range of Re_c between 10×10^3 and 15×10^3

.

In the fifth chapter, a detailed study of active control is presented for a NACA0012 airfoil. As commented in the introduction section, the time between the appearance and breakdown of wingtip vortices makes airport runways to be less efficient regarding use in landing and take-off operations. A strategy to destroy the wingtip is still an open question, and it would be welcomed by aircraft's manufactures. To that end, we study in chapter five a plausible solution using continuous jets in the spanwise direction. We compare how the maximum azimuthal velocity decays with a injection in the near- and far-field (up to 20 chords). It has been confirmed that the aspect ratio $R_{jet} = 1$ defined as the relation between the jet and external velocities give us the highest growth rate of vortex decay. This observation has also been corroborated by the attenuation of the vorticity field.

6.2   Recommendations for future work

In general, this thesis contains numerical simulations and experimental measurements and a mathematical model of wingtip vortices behind a NACA0012 airfoil.

The motivation of this thesis has been the improvement of the knowledge of the dynamics of wingtip vortices which is a key point for designing different strategies to destroy these vortices in airport runways.

Theoretical parameters such as the vortex strength as well as the vortex decay in the near- and far-field are necessary to characterise these trailing vortices. The assessments presented as conclusions on the dynamics of wingtip vortices give an idea that this study requires depth and long period of investigation if one aim is to account for the numerous phenomena of turbulent diffusion that this type of flows with strong rotation exhibit. As the research progresses, some considerations have been made that envisage numerous lines of potential research that could be stemmed from this study. Let us briefly describe some of them.

Our contribution regarding the novel experimental technique to avoid complex PIV measurements in a wind tunnel could be extended. Only Batchelor's model has been introduced in the differential equations to describe the path lines behind the wing, so the Moore & Saffman's model could be another candidate. To that end, the results from this model are of great interest to confirm the vortex decay (parameter n).

It should also be interesting to extend from 2D to 3D the PIV measurements thus giving more details of the flow structure in the towing tank. Moreover, the implications of the parameters from Batchelor's model together with Moore & Saffman's model as a function of Reynolds numbers have opened new questions. These are essential for knowing the nature of the unstable mode observed at $Re \approx 1300$ and also to define other critical Reynolds number at which the viscosity should be neglected in the mathematical models (Re_c=10,15×10^3. The author does believe that some clues regarding the nature of the instability at $Re_c \approx 1,3 \times 10^3$ could be given performing a POD analysis of the DNS. In addition, the relation of these two critical Reynolds numbers must be related to the aerodynamics characteristics of drag and lift coefficients.

The active control at different continuous speed ratios must be explored. Parameters R_jet belonging to the low range are also more significant for technological applications (R_jet of the order of 0.1 or less). Besides, not only the continuous jet but also a pulsating jet could be studied. In this sense, two configurations can be addressed: synthetic jet and pulsating jet over a constant signal. The mathematical models given in this study must be the starting point of future work that corresponds to optimal response or frequency response of trailing vortices. The results of stability analyses with the most unstable modes could be implemented experimentally.

Lastly, two aspects are of great interest. Firstly, the influence of external turbulence, so a mesh with different effective surface promoting different intensity levels could be set upstream the airfoil in the towing tank. Secondly, the dependence of trailing vortices on the wing geometry. Only the aspect ratio AR=2 has been studied, so the trailing vortices coming from wings with some new values of the aspect ratio between the chord and the length in the spanwise direction could be analysed in detail.

References

Aeroclub, S. L. (2006). Boeing b-757 with wing-tip vortex on clouds. http://www.sunlakesaeroclub.org/updates_web_data/081231/Contrails.htm.

Ahmadi-Baloutaki, M., Carriveau, R., & Ting, D. S. K. (2015). An experimental study on the interaction between free-stream turbulence and a wing-tip vortex in the near-field. *Aerospace Science and Technology*, 43, 395–405.

Albano, F., Gregorio, F. D., & Ragni, A. (2003). Trailing vortex detection and quantitative evaluation of vortex characteristics by piv technique. In *Instrumentation in Aerospace Simulation Facilities, 2003. ICIASF '03. 20th International Congress on* (pp. 31–43).

Alexey, R. (2006). Mi-8 helicopter. https://russianplanes.net/ID16778.

Allen, A. & Breitsamter, C. (2009). Experimental investigation of counter-rotating four vortex aircraft wake. *Aerosp. Sci. Technol.*, 13, 114.

Amitay, M. & Cannelle, F. (2006). Evolution of finite span synthetic jets. *Physics of Fluids*, 18(5).

Amitay, M., Smith, D. R., Kibens, V., Parekh, D. E., & Glezer, A. (2001). Aerodynamic Flow Control over an Unconventional Airfoil Using Synthetic Jet Actuators. *AIAA Journal*, 39(3), 361–370.

Ananda, G. K., Sukumar, P. P., & Selig, M. S. (2015). Measured aerodynamic characteristics of wings at low Reynolds. *Aerospace Science and Technology*, 42, 392–406.

Astrobob (2015). Milk vortices in a cup of coffee. https://en.wikipedia.org/wiki/Vortex#/media/File:Milk_vortices.jpg.

Ayers, R. F. & Wilde, M. R. (1956). *Aerodynamic characteristics of a swept wing with spanwise blowing. An experimental investigation of the aerodynamic characteristics of a low aspect ratio swept wing with blowing in a spanwise direction from the tip*. Technical report, The college of Aeronautics Cranfield.

Bailey, S. C., Tavoularis, S., & Lee, B. H. (2006). Effects of Free-Stream Turbulence on Wing-Tip Vortex Formation and Near Field. *Journal of Aircraft*, 43(5), 1282–1291.

Bailey, S. C. C. & Tavoularis, S. (2008). Measurements of the velocity field of a wing-tip vortex, wandering in grid turbulence. *Journal of Fluid Mechanics*, 601, 281–315.

Baker, G. R., Barker, S. J., Bofah, K. K., & Saffman, P. (1974). Laser aneometer measurements of trailing vortices in water. *Journal of Fluid Mechanics Fluid Mech.*, 65 (2)(October), 325–336.

Batchelor, G. (1964). Axial flow in trailing line vortices. *J.Fluid Mech.*, 20, 645–658.

Beninati, M. L. & Marshall, J. S. (2005). An experimental study of the effect of free-stream turbulence on a trailing vortex. *Experiments in Fluids*, 38(2), 244–257.

Bhagwat, M., Caradonna, F., & Ramasamy, M. (2015). Wing–vortex interaction: unraveling the flowfield of a hovering rotor. *Experiments in Fluids*, 56(1).

Bilanin, a. J., Teske, M. E., & Williamson, G. (1977). *Vortex interactions and decay in aircraft wakes*. Technical Report 2, Nasa Contractor Report.

Birch, D. & Lee, T. (2003). Rollup and Near-Field Behavior of a Tip Vortex. *Journal of Aircraft*, 40(3 : Engineering notes), 603–607.

Birch, D., Lee, T., Mokhtarian, F., & Kafyeke, F. (2004). Structure and Induced Drag of a Tip Vortex. *Journal of Aircraft*, 41(5), 1138–1145.

Brandt, S. A. & Iversen, J. D. (1977). Merging of Aircraft Trailing Vortices. *Journal of Aircraft*, 14(12), 1212–1220.

Carafoli, E. (1964). The influence of lateral jets, simple or combined with longitudinal jets, upon the wing lifting characteristics(increased lift of wings of stol aircraft by use of lateral fluid jets, simple or combined with longitudinal jets). *Nasa Technical Reports Server*.

Carafoli, E. & Camarasescu, N. (1971). *New Researches on Small Span-Chord Ratio Wings with Lateral Jets*. Technical report, DTIC Document.

Chadwick, E. (2006). The vortex line in steady, incompressible Oseen flow. *Proceedings of the Royal Society of London A: Mathematical, Physical and Engineering Sciences*, 462(2066), 391–401.

Chigier, N. A. & Corsigilia, V. R. (1972). Wind-Tunnel Studies of Wing Wake Turbulence. *Journal of Aircraft*, 9(12), 820–825.

Chow, J., Zilliac, G., & Bradshaw, P. (1997). Mean Turbulence Measurements in the Near Field of a Wingtip Vortex. *AIAA Journal*, 35(February), 1561–1567.

Cohn, R. K. & Koochesfahani, M. M. (2000). The accuracy of remapping irregularly spaced velocity data onto a regular grid and the computation of vorticity. *Experim*, (pp. 61–69).

Corjon, A. (2004). Process and device for accelerating the destruction of at least two vortices in the wake of a moving body, particulary an aircraft. US Patent US 2004/6719246.

Corsigilia, V. R., Iversen, J. D., & Orloff, K. L. (1978). *Laser-Velocimeter Surveys of Merging Vortices in a Wind Tunnel - Complete Data and Analysis*. Technical Report October, NASA, California.

Corsiglia, V. R., Schwind, R. G., & Chigier, N. A. (1973). Rapid Scanning, Three-Dimensional Hot-Wire AnemometerSurveys of Wing-Tip Vortices. *Journal of Aircraft*, 10(12), 752–757.

Craft, T., Launder, B., & Robinson, C. (2005). The computational modelling of wing-tip vortices and their near-field decay. *Engineering Turbulence Modelling and Experiments 6*, (pp. 627 – 636).

Crouch, J. D. (1997). Instability and transient growth for two trailing-vortex pairs. *Journal of Fluid Mechanics*, 350, 311–330.

Crouch, J. D. (2000). Active system for early destruction of trailing vortices. US Patent US 2000/6082679.

Crouch, J. D., Miller, G. D., & Spalart, P. R. (2001). Active-Control System for Breakup of Airplane Trailing Vortices. *AIAA Journal*, 39(12), 2374–2381.

Crow, S. C. (1970). Stability theory for a pair of trailing vortices. *AIAA Journal*, 8(12), 2172–2179.

Crow, S. C. & Bate, E. R. (1976). Lifespan of trailing vortices in a turbulent atmosphere. *Journal of Aircraft*, 13(7), 476–482.

Dacles-Mariani, J., Zilliac, G. G., & Bradshaw, P. (1995). Numerical/experimental study of a wingtip vortex in the near field. *AIAA Journal*, 33(9), 1561–1568.

De Souza, F. & Faghani, D. (2001). Near-field wing tip vortex measurements via PIV. *19th AIAA Applied Aerodynamics Conference*, 2451(June).

del Pino, C., Lopez-Alonso, J. M., Parras, L., & Fernandez-Feria, R. (2011a). Dynamics of the wing-tip vortex in the near field of a NACA 0012 aerofoil. *Aeronautical Journal*, 115(1166), 229–239.

del Pino, C., Parras, L., Felli, M., & Fernandez-Feria, R. (2011b). Structure of trailing vortices: Comparison between particle image velocimetry measurements and theoretical models. *Physics of Fluids*, 23(1), 1–12.

Deniau, H. & Nybelen, L. (2009). Strategy for spatial simulation of co-rotating vortices. *Int. J. Numer. Methods Fluids*, 61, 23.

Desquesnes, G., Terracol, M., & Sagaut, P. (2007). Numerical investigation of the tone noise mechanism over laminar airfoils. *Journal of Fluid Mechanics*, 591, 155–182.

Devenport, W. J., Rife, M. C., Liapis, S. I., & Follin, G. J. (1996). The Structure and Development of a Wing-Tip Vortex. *Journal of Fluid Mechanics. n*, 312(November), 67–106.

Devenport, W. J., Vogel, C. M., & Zsoldos, J. S. (1999). Flow structure produced by the interaction and merger of a pair of co-rotating wing-tip vortices. *Journal of Fluid Mechanics*, 394, 357–377.

Devenport, W. J., Zoldos, Jeffrey, S., & Vogel, C. M. (1997). The dtructure and development of a counter-rotating wing-tip vortex pair. *Journal of Fluid Mechanics. n*, 332(July), 71–104.

Devenport, W. J. & Zsoldos, J. S. (1992). *An Experimental Investigation of Interesting Wing-Tip Vortex Pairs*. Technical report, Aerospace and Ocean Engineering Department, Arlington.

Dghim, M., Ferchichi, M., Perez, R., & BenChiekh, M. (2016). Near wake development of a wing tip vortex under the effect of synthetic jet actuation. *Aerospace Science and Technology*, 54, 88–107.

Duraisamy, K. & Lele, S. K. (2008). Evolution of isolated turbulent trailing vortices. *Physics of Fluids*, 20(3), 1–11.

Edstrand, A. M., Davis, T. B., Schmid, P. J., Taira., K., & Cattafesta-III, L. M. (2016). On the mechanism of trailing vortex wandering. *Journal of Fluid Mechanics*, 801, 1–11.

Elimelech, Y., Vasile, J., & Amitay, M. (2011). Secondary flow structures due to interaction between a finite-span synthetic jet and a 3-D cross flow. *Physics of Fluids*, 23(9).

Fabre, D. & Dizès, S. L. (2008). Viscous and inviscid centre modes in the linear stability of vortices: the vicinity of the neutral curves. *Journal of Fluid Mechanics*, 603, 1–38.

Fabre, D., Fontane, J., Brancher, P., Dizès, S. L., Roy, C., Leweke, T., Fernandez-Feria, R., Parras, L., & del Pino, C. (2008). *Synthesis on vortex meandering*. Technical Report No. D.1.1.1, STREP project no. AST4-CT- 2005-012238.

Fabre, D. & Jacquin, L. (2004). Short-wave cooperative instabilities in representative aircraft vortices. *Physics of Fluids*, 16(5), 1366–1378.

Fabre, D., Jacquin, L., & Loof, A. (2002). Optimal perturbations in a four-vortex aircraft wake in counter-rotating configuration. *Journal of Fluid Mechanics*, 451, 319–328.

Fedoul, F., Parras, L., del Pino, C., & Fernandez-Feria, R. (2014). Experimental study of the aerodynamic characteristics of a low-aspect-ratio flat plate array in a configuration of interest for a tidal energy converter. *Journal of Fluids and Structures*, 48, 487–496.

Feys, J. & Maslowe, S. A. (2014). Linear stability of the Moore-Saffman model for a trailing wingtip vortex. *Physics of Fluids*, 26(2).

Feys, J. & Maslowe, S. A. (2016). Elliptical instability of the moore-saffman model for a trailing wingtip vortex. *Journal of Fluid Mechanics*, 803, 556–590.

Francis, M. S. (1976). *An Experimental investigation of wing trailing vortex formation.* Technical Report August, Air Force Systems Command, Colorado.

Gaspareck, E. P. (1960). *Viscous decay of a vortex.* PhD thesis, Syracuse University, NY.

Gerz, T., Holzapfel, F., Bryant, W., Köpp, F., Frech, M., Tafferner, A., & Winkelmans, G. (2005). Research towards a wake-vortex advisory system for optimal aircraft spacing. *C. R. Phis.*, 6, 501.

Gerz, T., Holzapfel, F., & Darracq, D. (2001). Commercial aircraft wake vortices. *Prog. Aerosp. Sci.*, 38, 181.

Gim, O.-S. & Lee, G.-W. (2013). Flow characteristics and tip vortex formation around a NACA 0018 foil with an end plate. *Ocean Engineering*, 60, 28 – 38.

Giuni, M. (2013). *Formation and early development of wingtip vortices.* PhD thesis, University of Glasgow.

Green, S. & Acosta, A. J. (1991). Unsteady flow in trailing vortices. *Journal of Fluid Mechanics*, 227, 107–134.

Greenblatt, D. (2005). Trailing vortex management via boundary layer separation control. US Patent US 2005/0103944.

Heaton, C. (2007). Centre modes in inviscid swirling flows and their application to the stability of the Batchelor vortex. *Journal of Fluid Mechanics*, 576, 325–348.

Heaton, C. J. & Peake, N. (2007). Transient growth in vortices with axial flow. *Journal of Fluid Mechanics*, 587, 271–301.

Heyes, a. L., Jones, R. F., & Smith, D. a. (2004). Wandering of wing-tip vortices. *12th International Symposium on Applications of Laser Techniques to Fluid Mechanics.*

Heyes, A. L. & Smith, D. A. R. (2005). Modification of a wing tip vortex by vortex generators. *Aerospace Science and Technology*, 9(6), 469–475.

Hoarau, Y., Braza, M., Ventikos, Y., Faghani, D., & Tzabiras, G. (2003). Organized modes and the three-dimensional transition to turbulence in the incompressible flow around a naca0012 wing. *Journal of Fluid Mechanics*, 496, 63–72.

Holman, R., Utturkar, Y., Mittal, R., Smith, B. L., & Cattafesta, L. (2005). Formation Criterion for Synthetic Jets. *AIAA Journal*, 43(10), 2110–2116.

Igarashi, H., Durbin, P. A., Ma, H., & Hu, H. (2010). A Stereoscopic PIV Study of a Near-field Wingtip Vortex. *AIAA Journal*, 48(January), 1–13.

Iungo, G., Skinner, P., & Buresti, G. (2009). Correction of wandering smoothing effects on static measurements of a wing-tip vortex. *Experiments in Fluids*, 46(3), 435–452.

Jacquin, L., Fabre, D., Geffroy, P., & Coustols, E. (2001). The properties of a transport aircraft wake in the extended near field-An experimental study. *American Institute of Aeronautics and Astronautics*, 39th Aeros(AIAA 2001-1038).

Jacquin, L., Fabre, D., Sipp, D., & Coustols, E. (2005). Unsteadiness, instability and turbulence in trailing vortices. *Comptes Rendus Physique*, 6(July), 399–414.

Jacquin, L. & Pantano, C. (2002). On the persistence of trailing vortices. *J. Fluid. Mech.*, 471, 159–168.

James, S. (2015). Stunning tornado south of simla, colorado great contrast between the dirt and the funnel. https://twitter.com/jamessmartlp/status/623249486559641600.

Jammy, S. P., Hills, N., & Birch, D. M. (2014). Boundary conditions and vortex wandering. *Journal of Fluid Mechanics*, 747(1), 350–368.

Jones, L. E., Sandberg, R. D., & Sandham, N. D. (2008). Direct numerical simulations of forced and unforced separation bubbles on an airfoil at incidence. *Journal of Fluid Mechanics*, 602, 175–207.

Jones, L. E., Sandberg, R. D., & Sandham, N. D. (2010). Stability and receptivity characteristics of a laminar separation bubble on an aerofoil. *Journal of Fluid Mechanics*, 648, 257–296.

Lagarias, J. C., Reeds, J. A., Wright, M. H., & Wright, P. E. (1998). Convergence properties of the nelder–mead simplex method in low dimensions. *SIAM Journal on Optimization*, 9(1), 112–147.

Lee, C. S., Tavella, D. a., & Wood, N. J. (1989). Flow structure and scaling laws in lateral wing tip blowing. *AIAA Journal*, 27(8), 1002–1007.

Lee, T. (2011). PIV study of near-field tip vortex behind perforated gurney flaps. *Experiments in Fluids*, 50(2), 351–361.

Lee, T. & Pereira, J. (2013a). Modification of static-wing tip vortex via a slender half-delta wing. *Journal of Fluids and Structures*, 43, 1–14.

Lee, T. & Pereira, J. (2013b). Passive control of unsteady-wing tip vortex via a slender half-delta wing in both reverse and regular configurations. *Experiments in Fluids*, 54(7).

Lee, T. & Su, Y. (2012). Wingtip vortex control via the use of a reverse half-delta wing. *Experiments in Fluids*, 52(6), 1593–1609.

Lombard, J.-E. W., Moxey, D., Hoessler, J. F. A., Dhandapani, S., Taylor, M. J., & Sherwin, S. J. (2015). Transient simulation of a wingtip vortex at $re_c = 1.2 \cdot 10^6$. *AIAA Journal*.

Manar, F., Medina, A., & Jones., A. (2014). Effect of wall proximity on rotating wings. *Experiments in Fluids*, 55(9).

Mao, X. & Sherwin, S. J. (2012). Transient growth associated with continuous spectra of the batchelor vortex. *Journal of Fluid Mechanics*, 697, 35–59.

Margaris, P. (2006). Wing tip vortex control using synthetic jets. *Aeronautical Journal*, 3079, 673–681.

Margaris, P. & Gursul, I. (2009). Vortex topology of wing tip blowing. *Aerospace Science and Technology*, 14(3), 143–160.

Marshall, J. S. & Beninati, M. L. (2005). External turbulence interaction with a columnar vortex. *Journal of Fluid Mechanics*, 540, 221–245.

Martinez-Aranda, S., Garcia-Gonzalez, A. L., Parras, L., & del Pino, C. (2016). Comparison of the Aerodynamic Characteristics of the NACA0012 Airfoil at Low-to-Moderate Reynolds Numbers for any Aspect Ratio. *International Journal of Aerospace Sciences*, 4(1), 1–8.

Mason, W. H. & Marchman, F. J. (1972). Far-field structure of an aircraft trailing vortex. *NASA CR 62078*.

Mayer, E. W. & Powell, K. G. (1992). Viscous and inviscid instabilities of a trailing vortex. *Journal of Fluid Mechanics*, 245, 91–114.

McCormick, B., Sherrie, H., & Tangler, J. (1968). Structure of Trailing Vortices. *Journal of Aircraft*, 5(0021-8669), 260–267.

Melander, M. V., Zabusky, N. J., & Mcwilliams, J. C. (1988). Symmetric vortex merger in two dimensions: causes and conditions. *Journal of Fluid Mechanics*, 195, 303–340.

Meunier, P., Le Dizès, S., & Leweke, T. (2005). Physics of vortex merging. *Comptes Rendus Physique*, 6(4-5 SPEC. ISS.), 431–450.

Meunier, P. & Leweke, T. (2003). Analysis and treatment of errors due to high velocity gradients in particle image velocimetry. *Experiments in Fluids*, 35(5), 408–421.

Meunier, P. & Villermaux, E. (2003). How vortices mix. *Journal of Fluid Mechanics*, 476, 213–222.

Moore, D. W. & Saffman, P. (1973). Axial flow in laminar trailing vortices. *Journal of Fluid Mechanics*, 333, 491–508.

NASA (2012). Saturn north polar vortex. https://en.wikipedia.org/wiki/Vortex#/media/File:Saturn_north_polar_vortex_2012-11-27.jpg.

Nash, E. C., Lowson, M. V., & McAlpine, A. (1999). Boundary-layer instability noise on aerofoils. *Journal of Fluid Mechanics*, 382, 27–61.

Olendraru, C. & Sellier, A. (2002). Viscous effects in the absolute–convective instability of the Batchelor vortex. *Journal of Fluid Mechanics*, 459, 371–396.

Olsen, J. (1970). *Aircraft Wake Turbulence and Its Detection*.

Orloff, K. L. (1974). Trailing Vortex Wind-Tunnel Diagnostics with a Laser Velocimeter. *Journal of Aircraft*, 11(8), 477–482.

Ortega, J. M., Bristol, R. L., & Savas, Ö. (2003). Experimental study of the instability of unequal-strength counter-rotating vortex pairs. *Journal of Fluid Mechanics*, 474, 35–84.

Paredes, P., Rodríguez, D., & Theofilis, V. (2013). Three-dimensional solutions of trailing-vortex flows using parboiled equations. *AIAA Journal*, 51, 2763–2770.

Parras, L. & Fernandez-Feria, R. (2007). Interaction of an unconfined vortex with a solid surface. *Physics of Fluids*, 19(6).

Patrice, M., Thomas, L., Richard, L., Benoit, V. A., & Chao, W. (2004). *DPIVSoft User Guide*.

Pennings, P. C., Bosschers, J., Westerweel, J., & van Terwisga., T. J. C. (2015a). Dynamics of isolated vortex cavitation. *Journal of Fluid Mechanics*, 778.

Pennings, P. C., Westerweel, J., & van Terwisga., T. J. C. (2015b). Flow field measurement around vortex cavitation. *Experiments in Fluids*, 56(11).

Pet, W. (2006). Stunning tornado south of simla, colorado great contrast between the dirt and the funnel. http://alecjacobson.com/programs/regallery/tino-weinkauf/th_PropellerGFM2006_Silver_c1200.jpg.

Phillips, W. & Graham, J. (1984). Reynolds-stress measurements in a turbulent trailing vortex. *Journal of Fluid Mechanics*, 147, 353–371.

Pilot Friends (Copyright 2000). http://www.pilotfriend.com.

Prandtl, L. & Tietjens, O. (1957). *Fundamentals of Hydro and Aeromechanics*. Dover Publications.

Pröbsting, Scarano, F., & Morris, S. C. (2015). Regimes of tonal noise on an airfoil at moderate reynolds number. *J. Fluid Mech.*, 780, 407–438.

Raffel, M., Willert, C. E., Wereley, S. T., & Kompenhans, J. (2007). *Particle Image Velocimetry. A Practical Guide*. Springer Berlin Heidelberg, second edi edition.

Ragab, S. & Sreedhar, M. (1995). Numerical simulation of vortices with axial velocity deficits. *Physics of Fluids*, 7(3), 549.

Reinaud, J. N. & Dritschel, D. G. (2005). The critical merger distance between two co-rotating quasi-geostrophic vortices. *Journal of Fluid Mechanics*, 522, 357–381.

Robert, D. A. (2013). Vortex in draining bottle of water. https://commons.wikimedia.org/wiki/File:Vortex_in_draining_bottle_of_water.jpg.

Rokhsaz, K., Foster, S. R., & Miller, L. S. (2000). Exploratory Study of Aircraft Wake Vortex Filaments in a Water Tunnel. *Journal of Aircraft*, 37(6), 1022–1027.

Roy, C., Leweke, T., Thompson, M. C., & Hourigan, K. (2011). Experiments on the elliptic instability in vortex pairs with axial core flow. *Journal of Fluid Mechanics*, 677, 383–416.

Saffman, P. G. & Baker, G. R. (1979). Vortex Interactions. *Annual Review of Fluid Mechanics*, 11(1), 95–121.

Sahni, O., Wood, J., Jansen, K. E., & Amitay, M. (2011). Three-dimensional interactions between a finite-span synthetic jet and a crossflow. *Journal of Fluid Mechanics*, 671, 254–287.

Sarpkaya, T. & Daly, J. J. (1987). Effect of ambient turbulence on trailing vortices. *Journal of Aircraft*, 24(6), 399–404.

Serrano-Aguilera, J. J., Garcia-Ortiz, J. H., Gallardo-Claros, A., Parras, L., & del Pino, C. (2016). Experimental characterization of wingtip vortices in the near field using smoke flow visualizations. *Experiments in Fluids*, 57(8).

Shekarriz, A., Fu, T. C., Katz, J., & Huang, T. (1993). Near-field behavior of a tip vortex. *AIAA Journal*, 31(1), 112–118.

Shyy, W., Aono, H., Chimakurthi, S., Trizila, P., Kang, C.-K., Cesnik, C., & Liu, H. (2010). Recent progress in flapping wing aerodynamics and aeroelasticity. *Progress in Aerospace Sciences*, 46, 284–327.

Singh, P. I. & Uberoi, M. S. (1976). Experiments on vortex stability. *Physics of Fluids*, 19(12), 1858.

Sohn, M. H. & Chang, J. W. (2012). Visualization and PIV study of wing-tip vortices for three different tip configurations. *Aerospace Science and Technology*, 16(1), 40–46.

Spalart, P. R. (1998). Airplane trailing vortices. *Annual Review of Fluid Mechancis*, 30, 107–138.

Stifle, K. E. . & Panton, L. (1991). *Experimental of a Vortex Subjected to Study Imposed Strain*. Technical report, University of Texas, Austin.

Sun, Q. & Boyd, I. D. (2004). Flat-plate aerodynamics at very low reynolds number. *J. Fluid Mech.*, 502, 199–206.

Sun, R. & Daichin (2011). Experimental investigation on tip vortices and aerodynamics. *Theoretical and Applied Mechanics Letters*, 1(3), 032001.

Suzuki, T. (2015). Data assimilation in fluid dynamics. *Fluid Dynamics Research*, 47, 050001.

Suzuki, T., Ji, H., & Yamamoto, F. (2009a). Unsteady PTV velocity field past an airfoil solved with DNS: Part 1. Algorithm of hybrid simulation and hybrid velocity field at $Re \approx 10^3$. *Experiments in Fluids*, 47(6), 957–976.

Suzuki, T., Sanse, A., Mizushima, T., & Yamamoto, F. (2009b). Unsteady PTV velocity field past an airfoil solved with DNS: Part 2. Validation and application at Reynolds numbers up to $Re \leq 10^4$. *Experiments in Fluids*, 47(6), 977–994.

Taira, K. & Colonius, T. (2009a). On the effect of tip vortices in low-Reynolds-number post-stall flow control. *47th AIAA Aerospace Sciences Meeting*, 376, 1–13.

Taira, K. & Colonius, T. (2009b). Three-dimensional flows around low-aspect-ratio flat-plate wings at low Reynolds numbers. *Journal of Fluid Mechanics*, 623.

Tavella, D., Lee, C. S., & Wood, N. J. (1986). Influence of wing tip configuration on lateral blowing efficiency. In *24th Aerospace Sciences Meeting*, Aerospace Sciences Meetings. American Institute of Aeronautics and Astronautics.

Tavella, D. a., Wood, N. J., Lee, C. S., & Roberts, L. (1988). Lift modulation with lateral wing-tip blowing. *Journal of Aircraft*, 25(4), 311–316.

Tendero, J. A., Theofilis, V., Roura, M., & Govindarajan, R. (2015). On vortex filament methods for linear instability analysis of aircraft. *Aerospace Science and Technology*, 44, 51–68.

Uberoi, M. S. (1979). Mechanisms of decay of laminar and turbulent vortices. *Journal of Fluid Mechanics*, 90(02), 241–255.

Şugar Gabor, O., Koreanschi, A., Botez, R. M., Mamou, M., & Mebarki, Y. (2016). Numerical simulation and wind tunnel tests investigation and validation of a morphing wing-tip demonstrator aerodynamic performance. *Aerospace Science and Technology*, 53, 136–153.

van Buren, T., Whalen, E., & Amitay, M. (2014). Vortex formation of a finite-span synthetic jet: High Reynolds numbers. *Physics of Fluids*, 26(1).

van Jaarsveld, J. P. J., Holten, A. P. C., Elsenaar, A., Trieling, R. R., & van Heijst, G. (2011). An experimental study of the effect of external turbulence on the decay of a single vortex and a vortex pair. *Journal of Fluid Mechanics*, 670, 214–239.

Viola, F., Arratia, C., & Gallaire, F. (2016). Mode selection in trailing vortices: harmonic response of the non-parallel Batchelor vortex. *Journal of Fluid Mechanics*, 790(2016), 523–552.

Wang, Y., Liu, P., Hu, T., & Qu, Q. (2016). Investigation of co-rotating vortex merger in ground proximity. *Aerospace Science and Technology*, 53, 116–127.

White, H. E. (1963). *Wind tunnel investigation of the use of wing tip blowing to reduce drag for take off and landing.* Technical report, Armed Services Techincal Information Agency, Arlington.

Williamson, C. (1996). Vortex dynamics in the cylinder wake. *Annual Review of Fluid Mechancis*, 28, 477–539.

Wu, J., Vakili, A., Chen, Z., & Gilliam, F. (1983). Investigations on the effects of discrete wingtip jets. In *21st Aerospace Sciences Meeting*, Aerospace Sciences Meetings. American Institute of Aeronautics and Astronautics.

Wu, J. M., Vakili, A., & Chen, Z. (1982). Wing-tip jets aerodynamics performance. *ICAS 1982 Congres*, 6.3(5).

Yang, Z., Sarkar, P., & Hu, H. (2012). Visualization of the tip vortices in a wind turbine wake. *Journal of visualization*, 12, 39–44.

Yarusevych, S., Sullivan, P., & Kawall, J. G. (2006). Coherent structures in an airfoil boundary layer and wake at low reynolds numbers. *Physics of Fluids*, 18, 044101.

Yarusevych, S., Sullivan, P., & Kawall, J. G. (2009). On vortex shedding from an airfoil in low-reynolds-numbers flows. *Journal of Fluid Mechanics*, 632, 245–271.

Zhou, Y., Zhang, H. J., & Whitelaw, J. H. (2004). Wing-Tip Vortex Measurement With Particle Image Velocimetry. *34h AIAA Applied Aerodynamics Conference*, 2433(July).